

The Impact of $^{12}\text{C}(\alpha, \gamma)^{16}\text{O}$ Reaction on the Presupernova Evolution and Supernova Explodability of Massive Stars

WENYU XIN ^{1, 2, 3, 4} KEN'ICHI NOMOTO ⁵ AND GANG ZHAO ^{1, 2}

¹*National Astronomical Observatories, Chinese Academy of Sciences, Beijing 100101, China*

²*School of Astronomy and Space Science, University of Chinese Academy of Sciences, Beijing 100101, China*

³*Institute for Frontiers in Astronomy and Astrophysics, Beijing Normal University, Beijing, 102206, China*

⁴*School of Physics and Astronomy, Beijing Normal University, Beijing, 100875, China*

⁵*Kavli Institute for the Physics and Mathematics of the Universe (WPI), The University of Tokyo Institutes for Advanced Study, The University of Tokyo, Kashiwa, Chiba 277-8583, Japan*

Submitted to ApJS on February 16, 2025

ABSTRACT

Among the uncertainties of stellar evolution theory, we investigate how the $^{12}\text{C}(\alpha, \gamma)^{16}\text{O}$ reaction rate affects the evolution of massive stars for the initial masses of $M(\text{ZAMS}) = 13 - 40 M_{\odot}$ and the solar metallicity. We show that the *explodability* of these stars, i.e., which of a neutron star (NS) or a black hole (BH) is formed, is sensitive to the strength of convective shell burning of C and O, and thus the mass fractions of C ($X(\text{C})$) and O in the shell. For the small $^{12}\text{C}(\alpha, \gamma)^{16}\text{O}$ reaction rate that yields larger $X(\text{C})$, $X(\text{C})$ is further enhanced by mixing of C from the overlying layer and then C shell burning is strengthened. The extra heating by C shell burning tends to prevent the contraction of outer layers and decrease the *compactness parameter* at $M_r = 2.5 M_{\odot}$. This effect leads to the formation of smaller mass cores of Si and Fe and steeper density and pressure gradients at the O burning shell in the presupernova models. If the pressure gradient there is steeper, the model is more likely to explode to form a NS rather than a BH. We describe the pressure gradient against M_r with V/U and the density drop with $1/U$, where U and V are non-dimensional variables to describe the stellar structure. We estimate the critical values of V/U and $1/U$ at the O-burning shell above which the model is more likely to explode. We conclude that the smaller $^{12}\text{C}(\alpha, \gamma)^{16}\text{O}$ reaction rate makes the mass range of $M(\text{ZAMS})$ that forms a NS larger.

Keywords: Black Holes, Neutron Stars, Massive stars, Supernovae, Stellar evolution, pair-instability, reaction rate

1. INTRODUCTION

In the Universe, stars are formed with various masses, evolve, and die. Understanding the nature and evolution of stars is essentially crucial in understanding the evolution of the Universe (e.g., [Arnett 1996](#)). Extensive studies on spherical stars have shown that the evolution of stars are basically determined by their Zero-Age Main-

Sequence masses $M(\text{ZAMS})$ (e.g., [Hayashi et al. 1962](#)). In particular, stars with $M(\text{ZAMS}) \gtrsim 8 M_{\odot}$ evolve through hydrostatic nuclear burning and end their lives as core-collapse supernovae (e.g., [Nomoto et al. 2013](#)).

The exact explosion mechanism of core-collapse supernovae has not been well understood and the important properties of the explosion, e.g., the kinetic energy, has not been well-reproduced despite the extensive hydrodynamical simulations (e.g., [Sugimoto & Nomoto 1980](#)). Possible sources of difficulties in the core-collapse supernova modeling include the complicated physical pro-

cesses, such as neutrino transport during core-collapse and the difficulty in numerical treatment of those processes.

Another source of difficulty would be inaccuracies of the progenitor’s evolution and presupernova structure (e.g., Branch & Wheeler 2017). Such inaccuracies may stem from uncertainties in the complicated evolution processes, which include mass loss (e.g., Renzo et al. 2017), convection (e.g., Woosley et al. 2002), rotation (e.g., Heger et al. 2008; Chatzopoulos et al. 2016), magnetic fields (e.g., Maeder & Stahler 2009), and nuclear reactions (e.g., Weaver & Woosley 1993; Sallaska et al. 2013; Fields et al. 2018).

A possible example of such inaccuracies of progenitor’s evolution is the “mass-gap” problem of black holes (BHs). The current stellar evolution theory predicts that stars of $140 M_{\odot} \lesssim M(\text{ZAMS}) \lesssim 300 M_{\odot}$ undergo thermonuclear explosions triggered by electron-positron pair-creation instability and are disrupted completely without leaving the compact object (Barkat et al. 1967, pair-instability supernova: PISN)¹.

In close binary systems, stars with $140 M_{\odot} \lesssim M(\text{ZAMS}) \lesssim 300 M_{\odot}$ form He stars with $M(\text{He}) = 65 - 140 M_{\odot}$, which undergo PISNe. The upper mass limit of BHs formed from $M(\text{He}) \lesssim 65 M_{\odot}$ has been estimated to be $\sim 50 M_{\odot}$, while the lower mass limit of BHs from $M(\text{He}) \gtrsim 140 M_{\odot}$ is $\sim 140 M_{\odot}$ (Woosley 2017). Therefore, the “mass-gap” of $\sim 50 - 140 M_{\odot}$ due to PISNe has been predicted to exist for BHs in close binary systems.

However, the gravitational-wave (GW) signal GW190521 detected by LIGO/Virgo seems to originate from a merger of binary BHs ($85^{+21}_{-14} M_{\odot}$ and $66^{+17}_{-18} M_{\odot}$; Abbott et al. 2020). The probability that at least one of them falls in the BH mass-gap due to PISNe is 99.0%.

This is a challenge to the stellar evolution theory. It has motivated many attempts to examine the effects of uncertainties involved in the stellar evolution, such as the reaction rate (Farmer et al. 2019, 2020; Costa et al. 2021), rotation (Marchant & Moriya 2020; Mapelli et al. 2020), Super-Eddington accretion (van Son et al. 2020), magnetic fields (Keszthelyi et al. 2020) convection and overshooting (Renzo et al. 2020; Woosley & Heger 2021; Kaiser et al. 2020).

¹ For discussion on PISNe in this section, we assume that stars have low enough metallicities for a wind-type mass loss to be negligible (see, e.g., Limongi & Chieffi 2015, for the wind effect on the core mass).

Among those attempts is the study of the effects of the uncertainty of the $^{12}\text{C}(\alpha, \gamma)^{16}\text{O}$ reaction rate (Farmer et al. 2019, 2020; Costa et al. 2021). Those works have found that if the $^{12}\text{C}(\alpha, \gamma)^{16}\text{O}$ rate is smaller, the mass range of PISNe and thus the BH mass gap move to higher masses. The upper limit of the BH mass is $\sim 59, 71$, and $94 M_{\odot}$, if the rate is smaller by 1σ , 2σ , and 3σ , respectively (Farmer et al. 2020).

To explain the observed BH masses of GW190521, the $^{12}\text{C}(\alpha, \gamma)^{16}\text{O}$ rate might be significantly smaller than the currently adopted in the stellar evolution calculations, although some combination with other effects might be necessary.

Motivated by these works, we study the effect of the $^{12}\text{C}(\alpha, \gamma)^{16}\text{O}$ rate on the evolution of massive stars. The effect of the $^{12}\text{C}(\alpha, \gamma)^{16}\text{O}$ rate has been studied on nucleosynthesis yields (Weaver & Woosley 1993; Tur et al. 2007; West et al. 2013), carbon burning (Sukhbold et al. 2016; Sukhbold & Adams 2020), and compactness (Sukhbold & Woosley 2014). In the present work, we study the effects of this rate on the stellar structure and evolution through Fe core-collapse more systematically. In particular, we will focus on how the rate uncertainty affects the presupernova structure and the explosability, i.e., whether the progenitors explode or collapse (O’Connor & Ott 2011; Ugliano et al. 2012; Ertl et al. 2016; Müller et al. 2016).

More specifically, to clarify the mass and the rate dependencies, we evolve stars with $M(\text{ZAMS}) = 13 - 40 M_{\odot}$ from the ZAMS to Fe core-collapse with MESA by changing the $^{12}\text{C}(\alpha, \gamma)^{16}\text{O}$ rate in the range of $\pm 3\sigma$. Effects on nucleosynthesis yields, including metallicity effects, will be reported in the forthcoming paper.

The uncertainties in the stellar structure and evolution also stem from the difference in computer codes and numerical methods. Thus our aim of the present study includes the comparison of our MESA results with other numerical results obtained with different codes such as Kepler (Weaver & Woosley 1993; Sukhbold & Woosley 2014), FRANEC (Chieffi & Limongi 2020), and previous results by MESA (Farmer et al. 2016).

In Section 2, we describe the models and some basic definitions used in this work including non-dimensional variables U and V . In Section 3, we present the evolution of H and He burning and discuss the effect of $^{12}\text{C}(\alpha, \gamma)^{16}\text{O}$ rate on the mass fraction of ^{12}C during He burning and the C ignition stages. In Section 4, we study how this reaction rate affects the evolution from C burning to the Fe core-collapse and the presupernova core structure for $M(\text{ZAMS}) = 28, 25$ and $30 M_{\odot}$. In

Section 5, we study the explodability of the presupernova models for all ranges of $M(\text{ZAMS})$ and σ studied here, showing the criterion of the explodability including the critical values of V/U and $1/U$. We then show how the mass range $M(\text{ZAMS})$ of stars to form a neutron star (NS) (or a BH) depends on the $^{12}\text{C}(\alpha, \gamma)^{16}\text{O}$ rate. In Section 6, summaries and discussion are given.

2. MODELS AND PARAMETERS

We employ the Modules for Experiments in Stellar Astrophysics (MESA, version 12778; Paxton et al. 2011, 2013, 2015, 2018, 2019; Jermyn et al. 2023) to evolve massive stars from ZAMS to Fe core-collapse. The packages “25M_pre_ms_to_core_collapse” (examples in the test suite directory of MESA) are modified to build our models.

2.1. Reactions and Nuclear Network

Table 1. Nuclides included in the nuclear reaction network of mesa_128.net.

Element	A_{\min}	A_{\max}	Element	A_{\min}	A_{\max}
n	1	1	S	31	34
H	1	2	Cl	35	37
He	3	4	Ar	35	38
Li	7	7	K	39	43
Be	7	10	Ca	39	44
B	8	8	Sc	43	46
C	12	13	Ti	44	48
N	13	15	V	47	51
O	14	18	Cr	48	57
F	17	19	Mn	51	56
Ne	18	22	Fe	52	58
Na	21	24	Co	55	60
Mg	23	26	Ni	55	61
Al	25	28	Cu	59	62
Si	27	30	Zn	60	64
P	30	32			

⁸Be is not included.

To study nucleosynthesis, we adopt a large nuclear reaction network consisting of 128 isotopes (mesa_128.net, Paxton et al. 2011; Timmes 1999; Timmes et al. 2000). The isotopes included in this network are listed in Table 1. Farmer et al. (2016) studied the evolution with several sizes of network and concluded that ~ 127 isotopes are needed to get convergence of various quantities of stellar models at the $\sim 10\%$ level.

For weak interactions, the tabulation of Langanke & Martínez-Pinedo (2000); Oda et al. (1994); Fuller et al.

Table 2. The corresponding relationship between multiplier factors, $f_{C12\alpha}$, and the σ of $^{12}\text{C}(\alpha, \gamma)^{16}\text{O}$ reaction rates for the temperature during the He burning stage.

σ	-3	-2	-1	0	1	2	3
$f_{C12\alpha}$	0.37	0.52	0.72	1	1.28	1.93	2.69

(1985) are adopted. In this work, the reaction rates of 3α from Angulo et al. (1999), $^{12}\text{C}(\alpha, \gamma)^{16}\text{O}$ from Kunz et al. (2002), and the $^{12}\text{C}+^{12}\text{C}$ rate from Tumino et al. (2018) are adopted. Other reaction rates are taken from REACLIB (Cyburt et al. 2010).

Regarding the uncertainty of the $^{12}\text{C}(\alpha, \gamma)^{16}\text{O}$ rate, all direct measurements of this reaction rate have been performed at the energies higher than $E_{\text{c.m.}} = 891$ keV (Hammer et al. 2005), which is much higher than the energy ($E_{\text{c.m.}} = 300$ keV) corresponding to the temperature during helium burning (An et al. 2015).

The cross-section decreases exponentially at low energies, resulting from the small Coulomb penetrability. Therefore, it is necessary to extrapolate from the high energy to obtain the reaction rate in the astrophysics environment. However, most estimates are still far from the uncertainty of better than 10% required by stellar models (e.g., Woosley et al. 2002).

Since the uncertainty of the reaction rate follows the log-normal distribution, we can calculate the lower and upper rates given by $\pm 3\sigma$ for $^{12}\text{C}(\alpha, \gamma)^{16}\text{O}$ to cover 99% of the probability distribution of the rate (Sallaska et al. 2013). The σ here is defined by the following formula:

$$e^{\sigma} = \sqrt{\frac{x_{\text{high}}}{x_{\text{low}}}} \quad (1)$$

where x_{high} and x_{low} represent the high and low rates of the reactions, respectively. In the present work, we use $\sigma_{C12\alpha}$ to represent the uncertainty of the $^{12}\text{C}(\alpha, \gamma)^{16}\text{O}$ rate. We also show the value of the multipliers corresponding to each σ in Table 2.

2.2. Input Physics

We calculate the evolution of 82 models in this work. For $\sigma_{C12\alpha} = 0$, we evolve stars with the initial masses of $M(\text{ZAMS}) = 13 - 40 M_{\odot}$ for a mass interval of $1 M_{\odot}$. We also evolve stars with $M(\text{ZAMS}) = 20, 23, 25, 28, 30, 32, 35, 38$, and $40 M_{\odot}$ for $\sigma_{C12\alpha} = \pm 1, \pm 2$, and ± 3 .

For the convection zone, we use the mixing-length theory with the ratio between the mixing-length and the pressure scale height of $\alpha_{\text{mlt}} = 3.0$ when the mass fraction of hydrogen is larger than 0.5 and $\alpha_{\text{mlt}} =$

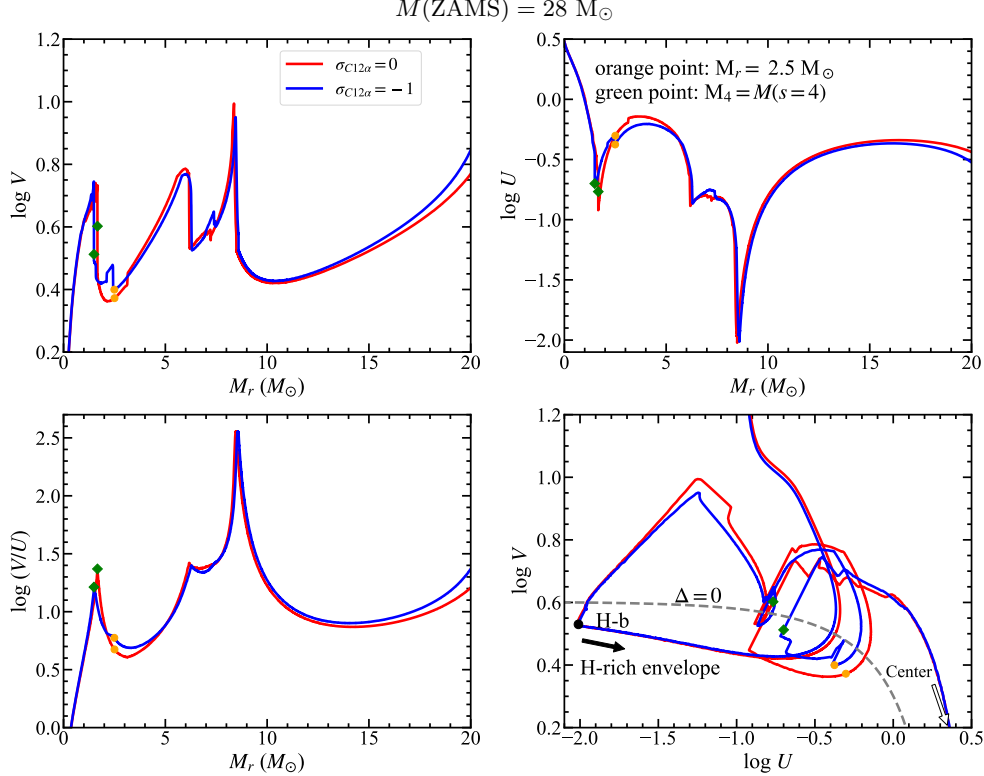


Figure 1. The $U - V$ curves at $t = t_f$ for $M(\text{ZAMS}) = 28 M_\odot$. The black points indicate the place where $M_r = 2.5 M_\odot$, while the green squares show the place where $M_r = M(s = 4)$, which is defined in Equation (14). In the $\log U - \log V$ plot, we show the star's center with the white arrow. The location of the hydrogen burning shell and the direction of the H-rich envelope are indicated with the black point and arrow. The gray dashed line indicates the $\Delta \equiv 2U + V - 4 = 0$ curve.

1.5 for other stage. We adopt the exponential scheme with $f_0 = 0.004$ and $f = 0.01$ for the overshooting. The Dutch scheme is adopted for the mass loss with `Dutch_scaling_factor=0.5`. Three main mass loss prescriptions included in Dutch wind are from de Jager et al. (1988) for cool stars, Vink et al. (2001) for hot hydrogen-rich stars, and Nugis & Lamers (2000) for Wolf-Rayet stars.

For the initial elemental abundances, we assume the He mass fraction of $Y = 2Z + 0.24$ and the H mass fraction of $X = 1 - Y - Z$. Here, Z denotes the sum of the initial mass fractions of heavy elements, i.e., C and heavier elements. We assume the solar abundance ratios from Anders & Grevesse (1989) for isotopic abundance ratios among heavy elements.

2.3. Basics of Stellar Evolution

In this section, we describe some relations and definitions, which will be used later.

2.3.1. $U - V$ Curves

The hydrostatic equilibrium of a spherical star gives two non-dimensional quantities, which has been defined in, e.g., Schwarzschild (1958), Hayashi et al. (1962), Sug-

imoto & Nomoto (1980), Nomoto (1984), Sugimoto & Fujimoto (2000) and Kippenhahn et al. (2013):

$$U \equiv \frac{d \ln M_r}{d \ln r} = \frac{4\pi r^3 \rho}{M_r} \quad (2)$$

$$V \equiv -\frac{d \ln P}{d \ln r} = \frac{GM_r \rho}{rP} \quad (3)$$

From Equations (2) and (3), we obtain V/U as

$$\frac{V}{U} = -\frac{d \ln P}{d \ln M_r} = \frac{GM_r^2}{4\pi r^4 P} \quad (4)$$

Differentiating Equations (2) and (3), we also obtain

$$d \ln r = -\frac{1}{\Delta} (d \ln U - d \ln V) \quad (5)$$

$$\Delta \equiv 2U + 4V - 4 \quad (6)$$

Here V/U and $1/U$, respectively, show the steepness of the gradients of $\log P$ and $\log r$ against $\log M_r$, which are crucially important for the *explodability* of stars as will be discussed later (Section 5.3). Note also that U is the ratio between the local density at the enclosed mass

M_r and the mean density within the sphere of radius r . If U is very small (i.e., $1/U$ is very large), it indicates the existence of almost a *density jump*, which is also critical for explodability. V is the ratio between gravitational energy and thermal energy.

Figure 1 shows the $U - V$ curves of the $M(\text{ZAMS}) = 28 M_\odot$ star at the final stage when the central temperature reaches $\log T_c (\text{K}) = 10.0$. Here, we show the curves for $\sigma_{C12\alpha} = 0$ and -1 . Although the two curves look similar, important differences exist between the two cases, as will be discussed in Section 4.2.4.

In the $\log U - \log V$ plot, we show the star's center with the white arrow. The location of the hydrogen burning shell at $M_r = 8.5 M_\odot$ and the direction of the H-rich envelope are indicated by the black point and arrow. The dashed line indicates the curve of $\Delta \equiv 2U + V - 4 = 0$ (Sugimoto & Nomoto 1980). The loop of the $\log U - \log V$ curve shows a relatively large jump across $\Delta = 0$. The location of the above jump is typically a nuclear burning shell at the core edge. This jump from large V to small U in the deep core is critical for *explodability*.

The black points indicate the place where $M_r = 2.5 M_\odot$, while the green squares show the place where $M_r = M(s = 4)$, which is defined in Equation (14). These points will be discussed in later sections.

2.3.2. Negative Specific Heat

Another important quantity related to hydrostatic equilibrium is the effective mass (M_{eff}) giving the relation between the central quantities and the mass (Nomoto & Hashimoto 1988).

$$\frac{P_c^3}{\rho_c^4} = 4\pi G^3 \left(\frac{M_{\text{eff}}}{\phi} \right)^2 \quad (7)$$

where the P_c and ρ_c are the central pressure and density, respectively; ϕ is a dimensionless mass that depends on the polytropic index N in the central region as $\phi = 10.73$ and 16.14 for $N = 1.5$ and 3 , respectively (Sugimoto & Nomoto 1980).

Here the density (ρ) and pressure (P) are related by the polytropic index as

$$\frac{d \ln \rho}{d \ln P} = \frac{N}{N + 1} \quad (8)$$

As will be discussed in later sections, M_{eff} corresponds to the core mass enclosed within the most active nuclear burning shell.

For an ideal gas of $P = (k/\mu H)\rho T$, where μ is the mean molecular weight, H the unit of atomic mass, and k the

Boltzmann constant, Equation (7) gives

$$\frac{T_c^3}{\rho_c} \propto G^3 M_{\text{eff}}^2 \quad (9)$$

The specific entropy s

$$s = \frac{k}{\mu H} \ln \left(\frac{T^{3/2}}{\rho} \right) + C_1 \quad (10)$$

is then given at the center as

$$\frac{\mu H}{k} s_c = \ln \left(\frac{M_{\text{eff}}^2}{T_c^{3/2}} \right) + C_2 = \ln \left(\frac{M_{\text{eff}}}{\rho_c^{1/2}} \right) + C_3 \quad (11)$$

where C_1 , C_2 , and C_3 are additional constants. Equation 11 shows that for the same T_c (i.e., for roughly the same nuclear burning stage), s_c is higher (and ρ_c is lower) for larger M_{eff} , i.e., higher s_c is necessary to sustain larger mass against self-gravity. When the nuclear reaction is not active, the stellar core loses entropy by radiation and neutrinos and thus s_c decreases. Equation (11) shows that both T_c and ρ_c increase as s_c decreases for given M_{eff} as shown by

$$C_g = \frac{ds_c}{d \ln T_c} = -1.5 \frac{k}{\mu H} \quad (12)$$

Equation (12) (Nomoto & Hashimoto 1988) implies that the stellar core has the *negative specific heat*. The increase in ρ_c means the stellar core contracts and releases gravitational energy, part of which goes into internal energy and the rest goes into radiation and neutrino losses.

For discussion on the explodability of the presupernova models, several criteria have been proposed. One is the compactness parameter (ξ_{M_r/M_\odot}) from O'Connor & Ott (2011):

$$\xi_{M_r/M_\odot} = \frac{M_r/M_\odot}{r(M_r)/1000 \text{ km}} \quad (13)$$

where M_r is the enclosed mass at the radius of $r(M_r)$. O'Connor & Ott (2011) proposed $M_r/M_\odot = 2.5$, i.e., $\xi_{2.5}$ for the actual criterion.

The others are M_4 and μ_4 introduced by Ertl et al. (2016, 2020):

$$\mu_4 = \left. \frac{dm/M_\odot}{dr/1000 \text{ km}} \right|_{s=4} \quad (14)$$

where M_4 and r_4 are the mass and radial coordinates where the specific entropy is $s = 4$ (hereafter s is given in units of $\text{erg g}^{-1} \text{K}^{-1}$). μ_4 and $\mu_4 M_4$ are related to the accretion rate and accretion luminosity during the Fe core-collapse.

Table 3. Lost masses until the end of H burning, ΔM_{H} , He burning, ΔM_{He} , and Fe core-collapse, ΔM_{CC} , as well as the final mass, $M(\text{final})$.

$M(\text{Initial})$ (M_{\odot})	ΔM_{H} (M_{\odot})	ΔM_{He} (M_{\odot})	ΔM_{CC} (M_{\odot})	$M(\text{final})$ (M_{\odot})
13	0.17	0.60	0.64	12.36
14	0.19	0.79	0.83	13.17
15	0.22	0.98	1.02	13.98
16	0.25	1.43	1.48	14.52
17	0.29	1.81	1.86	15.14
18	0.33	1.66	1.71	16.29
19	0.37	2.49	2.55	16.45
20	0.39	2.51	2.58	17.42
21	0.42	2.75	2.82	18.18
22	0.46	2.87	2.94	19.06
23	0.51	2.93	3.01	19.99
24	0.55	4.07	4.15	19.85
25	0.61	3.88	3.97	21.03
26	0.62	4.61	4.70	21.30
27	0.69	4.96	5.06	21.94
28	0.78	5.76	5.85	22.15
29	0.89	5.76	5.86	23.14
30	0.99	6.07	6.17	23.83
31	1.11	7.60	7.70	23.93
32	1.23	7.85	7.97	24.03
33	1.35	8.37	8.51	24.49
34	1.48	8.50	8.63	25.37
35	1.62	9.69	9.81	25.19
36	1.77	10.62	10.74	25.26
37	1.91	11.25	11.38	25.62
38	2.06	12.06	12.12	25.88
39	2.22	12.12	12.24	26.76
40	2.38	12.85	12.97	27.03

3. HYDROGEN BURNING AND HELIUM BURNING

3.1. Hydrogen Burning

We evolve the stars from H burning with $X = 0.70$, $Y = 0.28$, and $Z = 0.02$ through the Fe core-collapse for $\sigma_{\text{C12}\alpha} = 0$ and -1 . Figure 2 shows the evolution of stars of $M(\text{ZAMS}) = 28 M_{\odot}$ in the central density and temperature diagram. The blue dashed lines show the ignition lines of C burning (for $X(\text{C}) = 0.5$), Ne burning, O burning and Si burning, where the energy generation rate by nuclear burning equals the energy loss rate by neutrino emissions. In the region on the left of the black line, stars are dynamically unstable due to the electron-positron pair creation (indicated as “pair

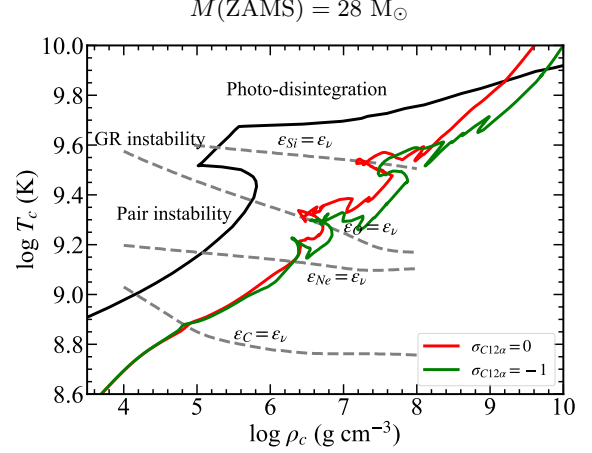


Figure 2. The central temperature against the central density for the evolution of the star with $M(\text{ZAMS}) = 28 M_{\odot}$, $Z = 0.02$, $\sigma_{\text{C12}\alpha} = 0$ and -1 . The blue dashed lines show the ignition lines of C burning, Ne burning, O burning and Si burning, where the energy generation rate by nuclear burning equals the energy loss rate by neutrino emissions. In the region on the left of the black line, stars are dynamically unstable due to the electron-positron pair creation (indicated as “pair instability”) (Ohkubo et al. 2009), general relativistic effects (“GR instability”) (see, e.g., Osaki 1966), and the photo-disintegration of matter in nuclear statistical equilibrium (NSE) at $Y_e = 0.5$ (“photo-disintegration”) (Ohkubo et al. 2009).

instability”) (Ohkubo et al. 2009), general relativistic effects (“GR instability”) (see, e.g., Osaki 1966), and the photo-disintegration of matter in nuclear statistical equilibrium (NSE) at $Y_e = 0.5$ (“photo-disintegration”) (Ohkubo et al. 2009).

H burning forms a He core. When the mass fractions of H at the center becomes $X < 10^{-4}$, which is the end of H burning, we define the He core mass, $M(\text{He})$, as an enclosed mass, M_r , at the He core boundary where X where X changes inwardly from $X \geq 10^{-4}$ to $X < 10^{-4}$.

In Figure 3, we show $M(\text{He})$ (M_{\odot}) as a function of $M(\text{ZAMS})$ by the red points. We obtain the gray straight line of

$$M(\text{He}) = 0.43M(\text{ZAMS}) - 4.13 M_{\odot} \quad (15)$$

by fitting the red points. (Of course, the $M(\text{He}) - M(\text{ZAMS})$ relation does not depend on $\sigma_{\text{C12}\alpha}$.)

Some deviations from the line may be due to different spatial and temporal resolutions in some models, which would affect the convective overshooting and thus the convective core mass. Our $M(\text{He}) - M(\text{ZAMS})$ relation is in good agreement with other works (e.g., Sukhbold & Woosley 2014).

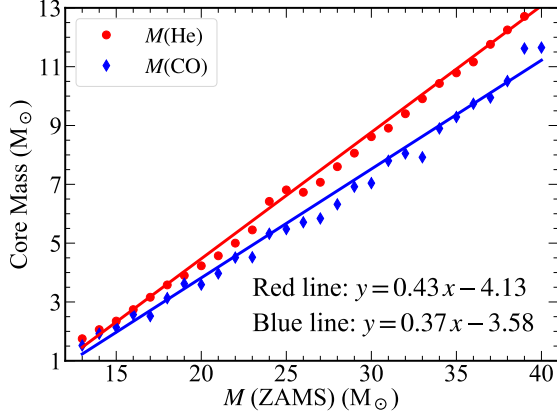


Figure 3. The core mass as a function of $M(\text{ZAMS})$ for $\sigma_{C12\alpha} = 0$. The red points and blue diamonds represent $M(\text{He})$ and $M(\text{CO})$, respectively. The red and blue straight lines are obtained by fitting the data.

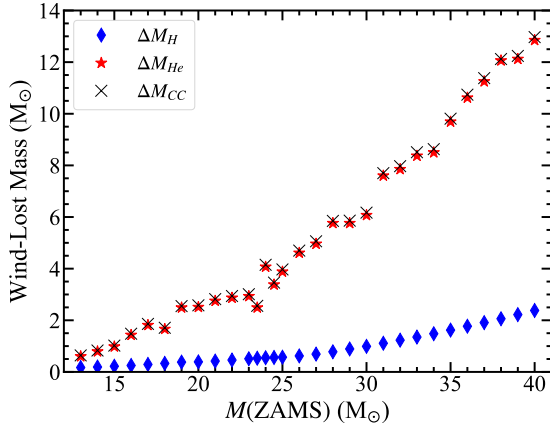


Figure 4. Lost masses by the stellar wind until the end of H burning (blue diamonds), He burning (red stars), and Fe core-collapse (black crosses), respectively, as a function of $M(\text{ZAMS})$.

For $Z = 0.02$, the wind mass loss is important during H and He burning. The accumulated lost masses at the end of H burning ΔM_{H} , He burning ΔM_{He} , and Fe core-collapse ΔM_{CC} , are summarized in Table 3 and Figure 4.

3.2. Helium Burning

He burning synthesizes mainly ^{12}C and ^{16}O . As $X(^4\text{He})$ decreases, the central temperature increases to be high enough for the $^{12}\text{C}(\alpha, \gamma)^{16}\text{O}$ reaction to convert ^{12}C to ^{16}O .

We define the CO core mass, $M(\text{CO})$, as M_r at the CO core boundary where $X(^4\text{He})$ inwardly decreases below 10^{-4} . We show $M(\text{CO})$ as a function of $M(\text{ZAMS})$ by the blue points in Figure 3. We obtain the green straight

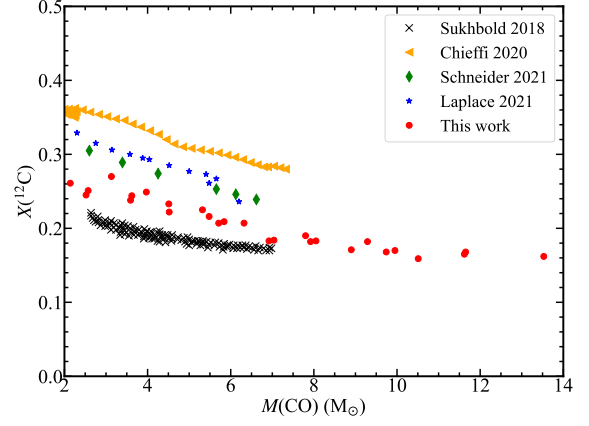


Figure 5. The mass fraction of ^{12}C , $X(^{12}\text{C})$, at the center as a function of the CO core mass, $M(\text{CO})$, for $\sigma_{C12\alpha} = 0$. The red points indicate our results. The grey cross, green squares, blue stars and orange triangle are those from Sukhbold et al. (2018), Schneider et al. (2021), Laplace et al. (2021) and Chieffi & Limongi (2020).

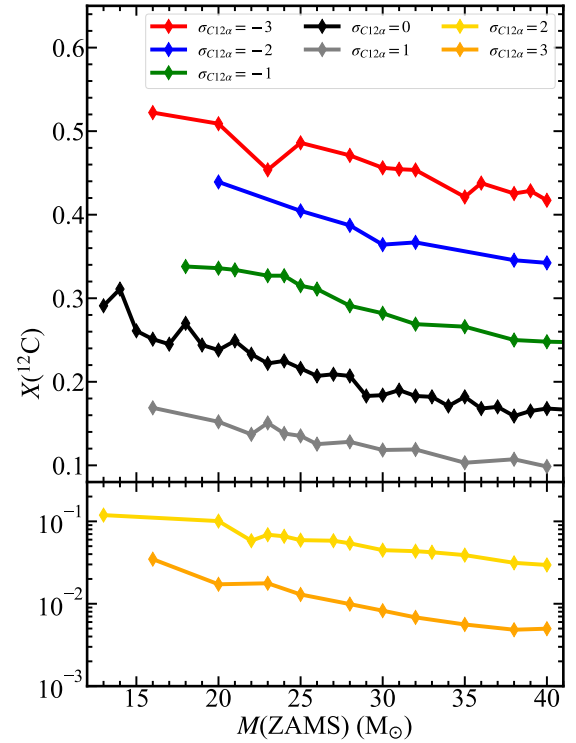


Figure 6. $X(^{12}\text{C})$ at the center when the mass fraction of He in the center becomes lower than 10^{-4} , as functions of $M(\text{ZAMS})$ and $\sigma_{C12\alpha}$.

line of

$$M(\text{CO}) = 0.37M(\text{ZAMS}) - 3.58 M_{\odot} \quad (16)$$

by fitting the blue points.

Table 4. Important evolutionary stages for $M(\text{ZAMS}) = 28 M_{\odot}$ and $\sigma_{C12\alpha} = 0$ and -1 .

Stages	$\log \tau$ (yr)	$\sigma_{C12\alpha} = 0$	$\log \tau$ (yr)	$\sigma_{C12\alpha} = -1$	Comment
		Convective Region (M_r)		Convective Region (M_r)	
He EX	4	$X(^{12}\text{C})=0.176$	4	$X(^{12}\text{C})=0.264$	
C CB	3 - 1	radiative	3 - 1	radiative	
1st C SB	1 - 0	radiative	2 - 1	radiative	CO core contraction
C EX	0		0.3		NeO core rapid contraction
2nd C SB	0 - -0.8	1.7 - 4.0	1 - 0.1	1.2 - 3.2	
Ne CB	-0.3 - -0.6	0.0 - 0.1	0.2 - -0.2	0.0 - 0.1	
Ne SB	-0.6 - -0.9	0.1 - 1.0	-0.2	0.1 - 0.6	
O CB	-0.9 - -2.6	0.0 - 0.6	-0.2 - -1.8	0.0 - 0.9	
3rd C SB	-0.9 - -2.6	2.2 - 6.5	0.1 - -5	2.0 - 7.0	Most important difference
1st O SB	-2.6 - -3.4	0.9 - 1.5	-1.8 - -2.8	0.9 - 1.5	
2nd O SB	-3.6 - -4.5	1.5 - 2.2	-2.8 - -3.0	1.2 - 1.8	
3rd O SB	-4.5 - -5	1.7 - 2.2	-3.5 - -5.0	1.2 - 2.0	Bottom of O SB gives $M(\text{Si})$
Si CB	-3.4 - -3.6	0.0 - 0.4	-2.9 - -3.5	0.0 - 1.0	
1st Si SB	-3.6 - -3.8	0.4 - 0.8	-3.7 - -4.0	0.8 - 1.2	
2nd Si SB	-4.1 - -5.0	0.9 - 1.5	-4.6 - -5.0	1.2 - 1.5	Bottom of Si SB gives $M(\text{Fe})$

CB, SB, and EX denote central burning, shell burning, and exhaustion stages, respectively.

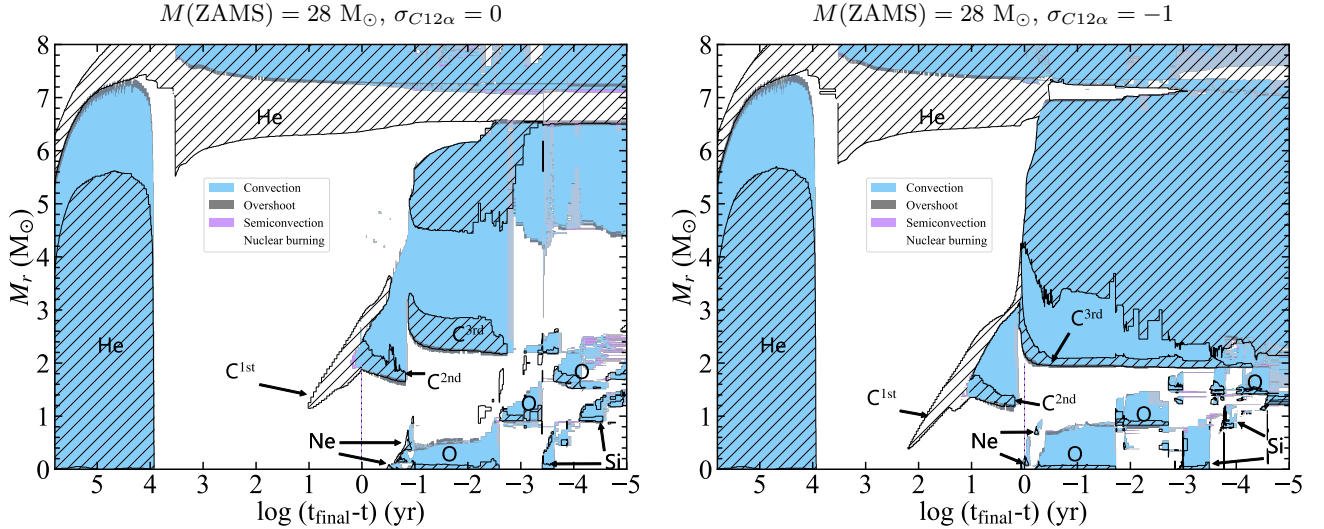


Figure 7. Kippenhahn diagrams of stars with $M(\text{ZAMS}) = 28 M_{\odot}$ for $\sigma_{C12\alpha} = 0$ (left) and -1 (right). The inner part of $M_r = 0 - 8 M_{\odot}$ is shown. The blue, grey and pink regions show where the convection, overshoot and semiconvection mixing occurs. The black-hatched region indicates where the nuclear burning occurs.

$X(^{12}\text{C})$ after He burning mainly depends on $\sigma_{C12\alpha}$ and is an important quantity for later stellar evolution, as will be discussed in Section 4. We thus compare $X(^{12}\text{C})$ in our work with others. As shown in Figure 5, $X(^{12}\text{C})$ in our models behaves similarly to other MESA works from Laplace et al. (2021) and Schneider et al. (2021). On the other hand, our result is located between those calculated by the KEPLER code (Sukhbold et al. 2018) and the FRANEC code (Chieffi & Limongi 2020). These differences stem not only from different sources of the

$^{12}\text{C}(\alpha, \gamma)^{16}\text{O}$ rate but also depend on other effects such as convective overshooting during the late phase of core He burning, 3D convective mixing in shell burning, as well as the binary stripping effect which is discussed in (Schneider et al. 2021).

Figure 6 shows $X(^{12}\text{C})$ at the center when $X(^4\text{He})$ becomes lower than 10^{-4} as functions of $M(\text{ZAMS})$ and $\sigma_{C12\alpha}$. We note that the effect of $\sigma_{C12\alpha}$ on $X(^{12}\text{C})$ is much larger than that of $M(\text{ZAMS})$. For example,

$X(^{12}\text{C})$ decreases from 0.51 to 0.02 as $\sigma_{C12\alpha}$ increases from -3 to 3 for $M(\text{ZAMS}) = 20 M_{\odot}$.

3.3. Carbon Ignition

After the core He burning, the CO core contracts. Figure 2 shows that the evolution of the central density and temperature reaches the dashed line of the ignition of C burning ($^{12}\text{C}+^{12}\text{C}$), where the nuclear energy generation rate (ϵ_C) is equal to the energy loss rate by neutrino emissions (ϵ_{ν}). However, that the C ignition line is obtained for $X(^{12}\text{C}) = 0.5$. With smaller $X(^{12}\text{C})$, C burning is less energetic because ϵ_C depends on $X(^{12}\text{C})^2$. If $X(^{12}\text{C})$ is smaller than a certain value, $\epsilon_C < \epsilon_{\nu}$. Then, C burning does not form a convective core and proceeds radiatively.

Table 5. The critical masses for different $\sigma_{C12\alpha}$ s.

$\sigma_{C12\alpha}$	-3	-2	-1	0	1
M_{crit}	26	24	22	20	16

Figure 6 shows that $X(^{12}\text{C})$ is smaller for larger $M(\text{ZAMS})$ and larger $^{12}\text{C}(\alpha, \gamma)^{16}\text{O}$ rate. Thus C burning proceeds radiatively for stars with $M(\text{ZAMS}) > M_{\text{crit}} \sim 20 M_{\odot}$ in our models (also Chieffi & Limongi 2020; Chieffi et al. 2021) as seen in Table 5 and will be discussed in detail in our forthcoming paper. For the $28 M_{\odot}$ stars, no convective core of C burning is formed for both $\sigma_{C12\alpha} = 0$ and -1 as seen in Figure 7.

4. CARBON BURNING TO FE CORE-COLLAPSE

In the following subsections, we study how the $^{12}\text{C}(\alpha, \gamma)^{16}\text{O}$ rate affects the presupernova core structure and the explodability (e.g., Weaver & Woosley 1993; Timmes et al. 1996) by comparing the evolutionary features for several cases. We particularly focus on the stars with $M(\text{ZAMS}) = 28 M_{\odot}$, $25 M_{\odot}$, and $35 M_{\odot}$ because of the following reasons. Hereafter, we call these stars as the “ $28 M_{\odot}$ star”, “ $25 M_{\odot}$ star”, and “ $35 M_{\odot}$ star”, respectively.

- (1) The evolution of the $28 M_{\odot}$ star is a typical case in which shows a large difference between $\sigma_{C12\alpha} = 0$ and -1 .
- (2) The evolution of the $25 M_{\odot}$ star shows a rather small difference between $\sigma_{C12\alpha} = 0$ and -1 , but there appears an important difference near the final stages of evolution. A significant difference occurs at earlier stages for $\sigma_{C12\alpha} = -2$.
- (3) The evolution of the $35 M_{\odot}$ star is a typical case where a significant difference appears for $\sigma_{C12\alpha} = 1$.

We discuss the $28 M_{\odot}$ models in detail, and the $25 M_{\odot}$ and $35 M_{\odot}$ models in short for comparisons.

4.1. Chemical Evolution of $28 M_{\odot}$ Star

After He exhaustion, the star evolves through the gravitational contraction of the core and nuclear burning at the center and outer shells until the formation of the Fe core, as shown in Figure 2.

These evolutionary stages are summarized in Table 4 for the $28 M_{\odot}$ star, where CB, SB, and EX denote central burning, shell burning, and exhaustion stages, respectively. Here the time

$$\tau = t_f - t \quad (17)$$

is measured from the final stage at t_f where the central density reaches $\log T_c \text{ (K)} = 10.0$. The evolutionary behavior and the time depend on the $^{12}\text{C}(\alpha, \gamma)^{16}\text{O}$ rate as seen from the comparison between $\sigma_{C12\alpha} = 0$ and -1 in Table 4.

The following figures show the evolutionary changes in various stellar quantities in the $28 M_{\odot}$ star from He burning to the beginning of Fe core-collapse. The dependence on the $^{12}\text{C}(\alpha, \gamma)^{16}\text{O}$ rate is seen from the comparison between $\sigma_{C12\alpha} = 0$ and -1 in these figures.

Figures 7 show Kippenhahn Diagrams. The inner part of $M_r = 0 - 8 M_{\odot}$ is shown. Nuclear burning (at the center and outer shells) produces a convective region as indicated by the blue region. The hatched region shows where the energy generation rate of nuclear reactions are larger than the neutrino loss rate. We should see that several convective shells are formed, which largely affect the stellar structure and evolution, as will be discussed in later sections.

Figure 8 shows the time evolution of the mass fractions of some isotopes at the center (Figure 8 (a, b)), $M_r = 1.5 M_{\odot}$ (Figure 8 (c, d)), $M_r = 2.0 M_{\odot}$ (Figure 8 (e, f)), and $M_r = 2.5 M_{\odot}$ (Figure 8 (g, h)) for the $28 M_{\odot}$ star from He burning through Fe core-collapse for $\sigma_{C12\alpha} = 0$ (Figure 8 (a, c, e, g)), and $\sigma_{C12\alpha} = -1$ (Figure 8 (b, d, f, h)). In the following subsections, the chemical evolution of the central core is described as shown in the abundance evolution at the center (Figure 8 (a, b)). Then, the evolution of the outer layers and the burning of carbon and oxygen shells will be discussed.

4.1.1. Central Carbon Burning

The abundance distributions before C burning are shown in Figure 9. Note $X(^{12}\text{C})$ in the CO core is smaller for $\sigma_{C12\alpha} = 0$ (left) than that for $\sigma_{C12\alpha} = -1$ (right).

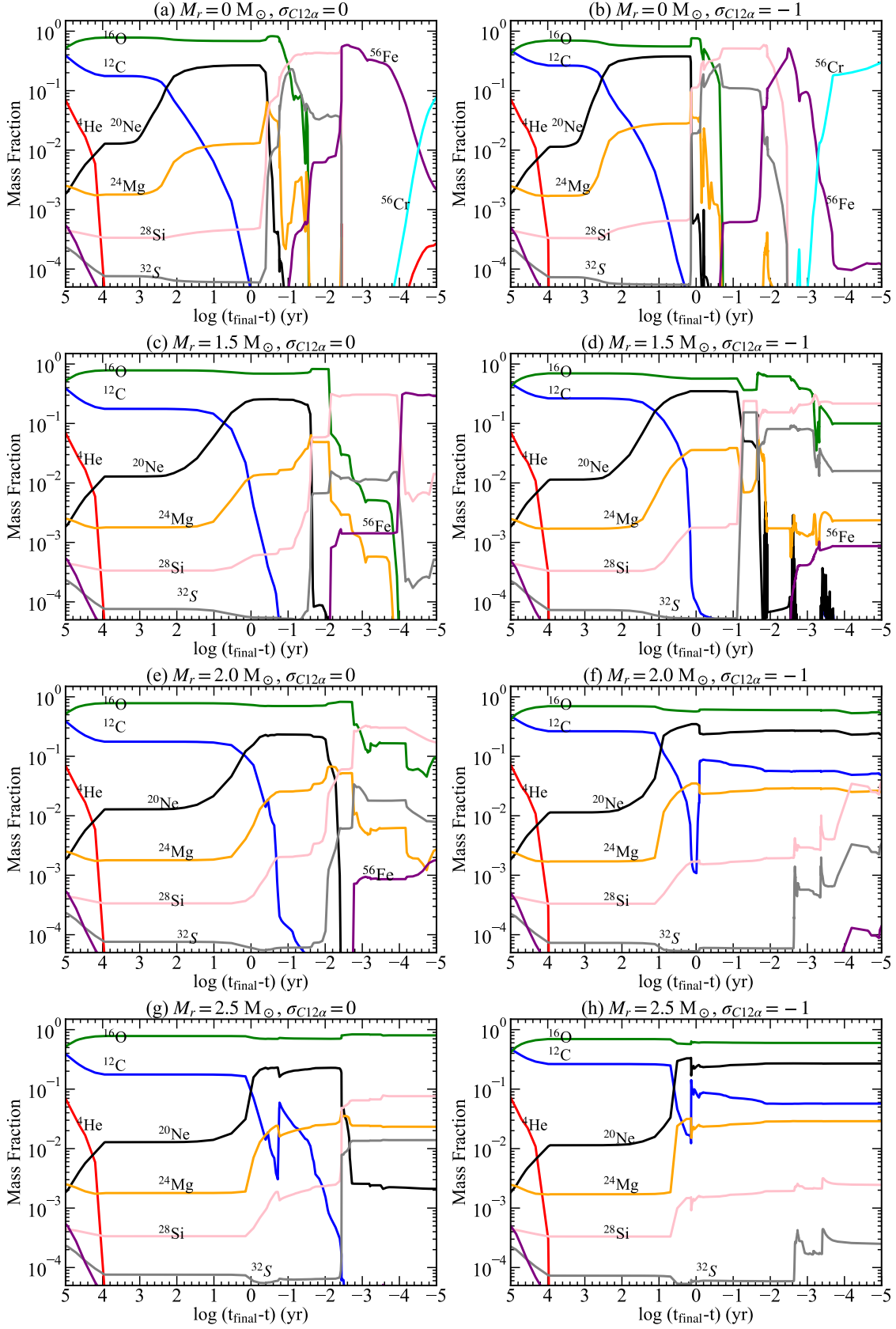
$M(\text{ZAMS}) = 28 M_{\odot}$


Figure 8. The time evolution of the mass fractions of some isotopes at the center, $M_r = 1.5 M_{\odot}$, $M_r = 2.0 M_{\odot}$ and $M_r = 2.5 M_{\odot}$ for the $M(\text{ZAMS}) = 28 M_{\odot}$ star with $\sigma_{C12\alpha} = 0$ (left) and -1 (right).

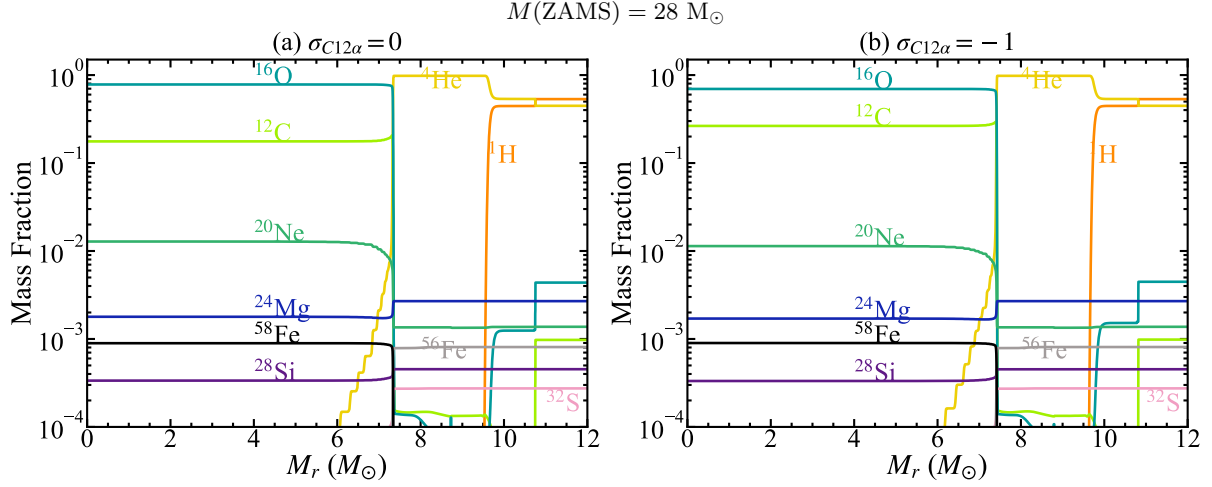


Figure 9. Abundance distributions of stars with $M(\text{ZAMS}) = 28 M_{\odot}$ for $\sigma_{C12\alpha} = 0$ (left) and -1 (right) at the end of He burning ($\tau \sim 10^4$ yr).

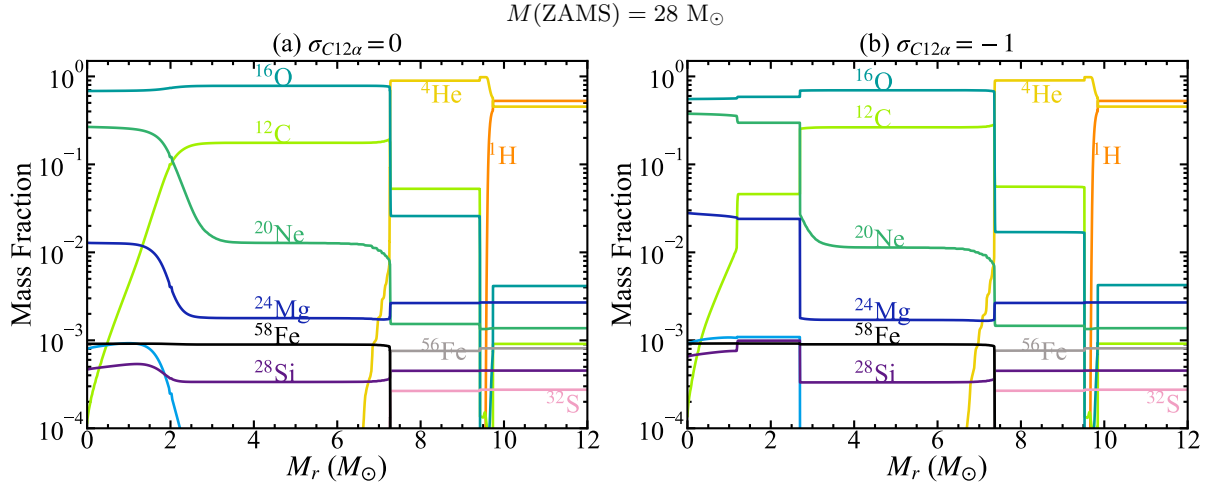


Figure 10. Abundance distributions of stars with $M(\text{ZAMS}) = 28 M_{\odot}$ for $\sigma_{C12\alpha} = 0$ (left) and -1 (right) at the end of C burning ($\tau \sim 10^{0.3-0}$ yr).

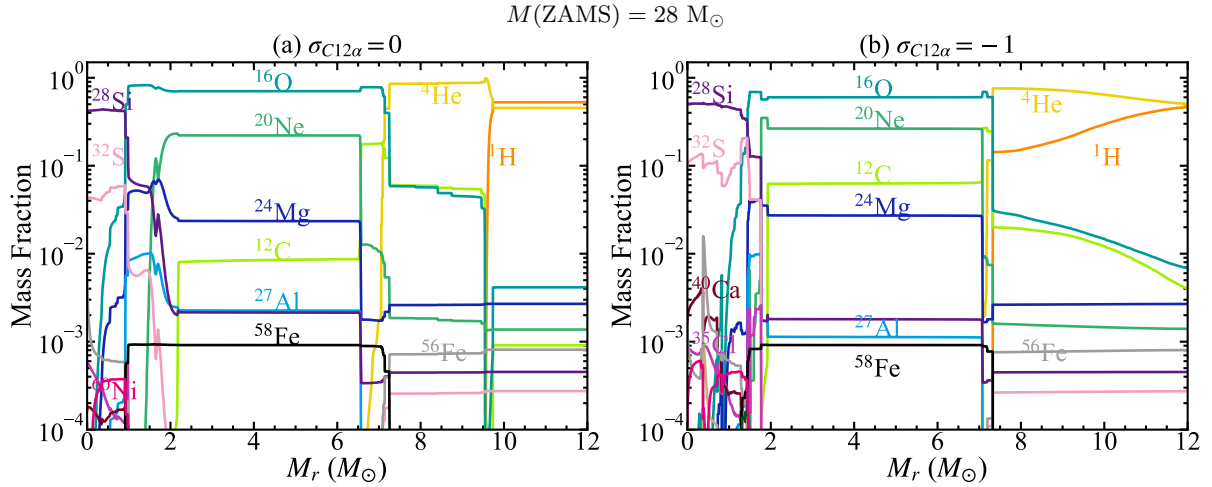


Figure 11. Abundance distributions of stars with $M(\text{ZAMS}) = 28 M_{\odot}$ at the end of O burning: $\tau \sim 10^{-1.6}$ yr for $\sigma_{C12\alpha} = 0$ (left) and $\tau \sim 10^{-0.7}$ yr for $\sigma_{C12\alpha} = -1$ (right).

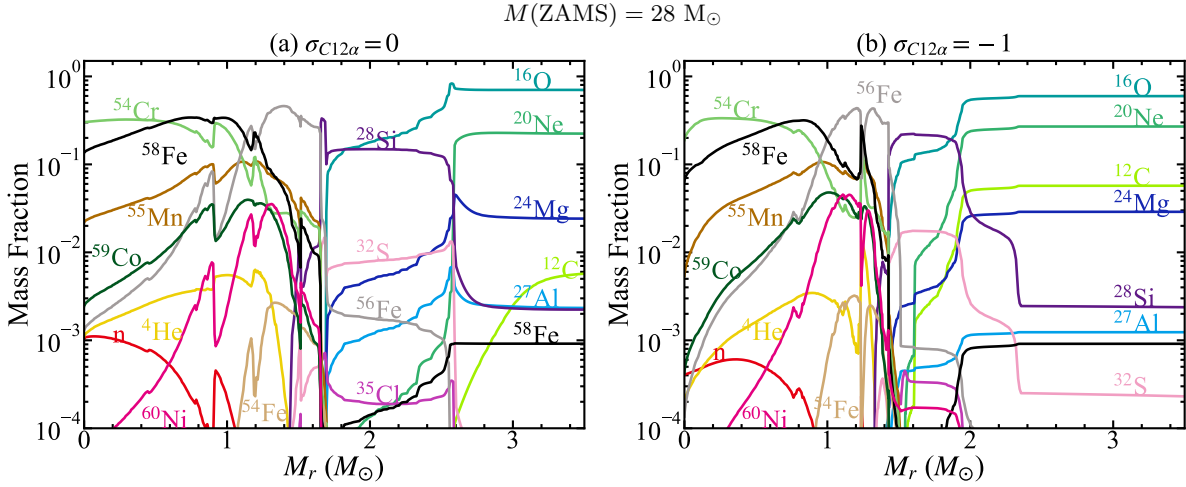


Figure 12. Abundance distributions in the inner $3.5 M_{\odot}$ of stars with $M(\text{ZAMS}) = 28 M_{\odot}$ for $\sigma_{C12\alpha} = 0$ (left) and -1 (right) at $\log T_c$ (K) = 10.0 ($\tau = t_f$).

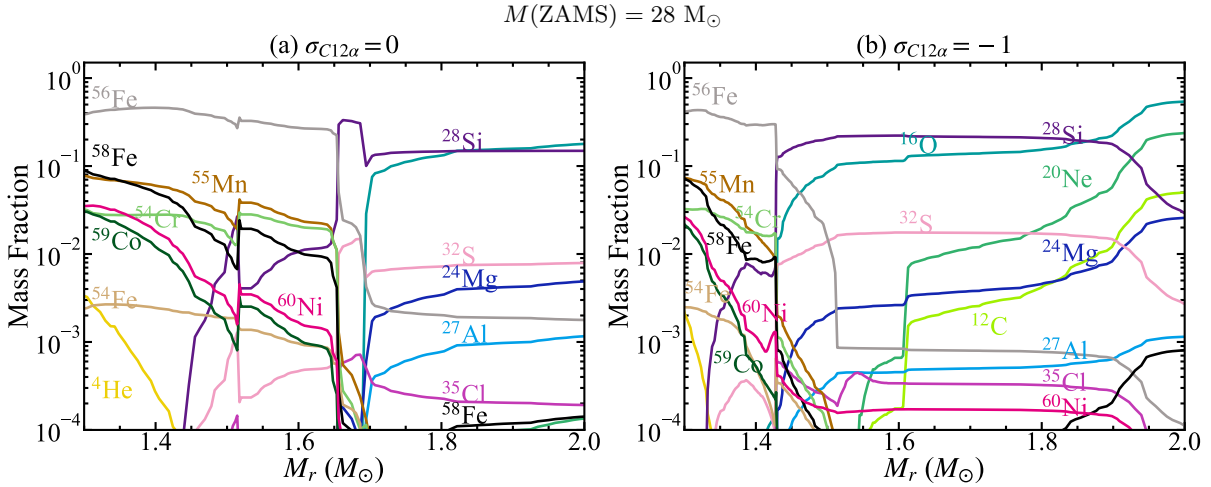


Figure 13. Detailed abundance distributions between $M_r = 1.2 - 2.0 M_{\odot}$ of stars with $M(\text{ZAMS}) = 28 M_{\odot}$ for $\sigma_{C12\alpha} = 0$ (left) and -1 (right) at $\log T_c$ (K) = 10.0 ($\tau = t_f$).

As shown by decreasing $X(^{12}\text{C})$ at the center in Figure 8, significant C burning takes place at $\tau \sim 10^{2.6}$ yr. As seen from Kippenhahn diagrams (Figs. 7), no convective core appears, i.e., C burns radiatively because the neutrino energy loss rate exceeds the energy generation rate for $M(\text{ZAMS}) > M_{\text{crit}} \sim 20 M_{\odot}$ (see Table 5 and subsection 3.3). As a result, the CO core continues to contract as seen in the smooth increase in T_c and ρ_c in Figure 2. There is no large difference in the central evolution between $\sigma_{C12\alpha} = 0$ and -1 during central C burning.

4.1.2. ONeMg Core Contraction and Neon Burning

After C-exhaustion in the central region, an ONeMg core composed of O, Ne, Mg, and Na are formed. The abundance distributions in the central ONeMg core around $\tau \sim 10^{0.3-0}$ yr are shown in Figures 10.

In the contracting ONeMg core, Ne is ignited at the center and burns convectively around $\tau \sim 10^{-0.3}$ yr and $10^{0.2}$ yr for $\sigma_{C12\alpha} = 0$ and -1 , respectively (Figs. 7 and 8(a, b)).

4.1.3. Oxygen Burning

After Ne exhaustion, an OSi core composed of O, Mg, Si, and S is formed. O burning takes place around $\tau \sim 10^{-0.2} - 10^{-1.0}$ yr (Figs. 8(a, b)), forming a convective core for both $\sigma_{C12\alpha} = 0$ and -1 .

Then, a Si-rich core composed of Si, S, Ar, and Ca is formed. Abundance distributions with the Si-rich core are shown in Figure 11 at $\tau \sim 10^{-1.6}$ yr for $\sigma_{C12\alpha} = 0$ (left) and $\tau \sim 10^{-0.7}$ yr for $\sigma_{C12\alpha} = -1$ (right).

4.1.4. Silicon Burning and Fe Core Contraction

Si burning takes place convectively for both $\sigma_{C12\alpha} = 0$ (Figure 8(a, c)) and $\sigma_{C12\alpha} = -1$ (Figure 8(b)), and a Fe core is formed. The Fe core contraction is accelerated by photo-disintegration of Fe-peak species and becomes dynamically unstable. We stop our calculations at $\log T_c$ (K) = 10.0 ($t = t_f$) because the reaction rates provided by the database (REACLIB) of MESA reach only $\log T(\text{K}) = 10.0$.

The abundance distributions at the final stage of $t = t_f$ are shown in Figure 12, and the detailed distributions in the Fe core are shown in Figure 13 for both $\sigma_{C12\alpha}$. (The Y_e distribution will be shown later in Figure 22.)

The Fe core masses $M(\text{Fe})$ at the boundary with $X(\text{Si}) = 10^{-3}$ are $1.51 M_\odot$ and $1.36 M_\odot$ for $\sigma_{C12\alpha} = 0$ and $\sigma_{C12\alpha} = -1$, respectively.

4.1.5. Carbon Shell Burning

The difference in the evolution between $\sigma_{C12\alpha} = 0$ and -1 more clearly appears in C shell burning (C SB in Table 4) compared with central core burning, as seen in Kippenhahn diagrams (Figs. 7) and summarized in Table 4. In this subsection, we describe the differences which can be seen mostly in the abundance patterns in Figures 8. Differences in physical quantities will be described in the next subsection.

(1) First C Shell Burning (1st C SB) in the CO Core: As discussed in the earlier subsection, the CO core contracts even during central C burning. As a result of the temperature increase in the outer shell, the energy generation rate of C burning exceeds the neutrino loss rate ($\epsilon > 0$) around $\tau \sim 10^{2.2}$ yr and $\sim 10^1$ yr for $\sigma_{C12\alpha} = -1$ and 0 , respectively (Table 4); Figure 7). The first C shell burning takes place radiatively.

(2) Second C Shell Burning (2nd C SB) in the ONeMg Core: As the ONeMg core contracts around $\tau \sim 10^{1.5-0.0}$ yr, the second C shell burning is ignited and produces a convective shell for both $\sigma_{C12\alpha}$. This is seen from the decrease in $X(^{12}\text{C})$ at $M_r = 1.5$ and $2.0 M_\odot$ in Figures 8(c)-(f).

(3) The third C Shell Burning (3rd C SB): The 3rd C shell burning behavior depends clearly on $\sigma_{C12\alpha}$.

(3-1) For $\sigma_{C12\alpha} = -1$, C shell-burning forms a convective shell at $\tau \sim 10^0$ yr. It extends from $M_r \sim 2.0 M_\odot$ to $6.9 M_\odot$ and mixes some C from the outer layer into the convective shell as seen from the increase in $X(^{12}\text{C})$ at $M_r = 2.0 M_\odot$ and $2.5 M_\odot$ in Figure 8(f) and (h), respectively. Owing to this enhancement of $X(^{12}\text{C})$, C shell burning is reactivated and continues to be active

through collapse with the convective shell extended from $M_r = 2.0 M_\odot$ (Figure 7).

(3-2) For $\sigma_{C12\alpha} = 0$, on the other hand, such convective mixing does not occur at $\tau \sim 10^0$ yr because of smaller $X(^{12}\text{C})$ during earlier C shell burning. Thus no increase in $X(^{12}\text{C})$ is seen at $M_r = 2.0 M_\odot$ in Figure 8(e). Then C is exhausted at $\tau \sim 10^{-1.5}$ yr.

Such a difference in the convective C shell between $\sigma_{C12\alpha} = 0$ and -1 stems from the difference in the C/O ratio after the He burning, and leads to an important difference in the later evolution.

As will be discussed in subsection 4.2.4 on $U - V$ curves, the existence of active C-shell burning at $M_r \sim 2.0 M_\odot$ makes M_{eff} (Equation 7) smaller for $\sigma_{C12\alpha} = -1$ than 0 . This makes the mass of the heavier element core larger for $\sigma_{C12\alpha} = 0$ than -1 as will be shown in § 4.2.4.

In fact, for $\sigma_{C12\alpha} = 0$, the layer around $M_r = 2.0 M_\odot$ becomes a part of the Si-rich core after $\tau = 10^{-2.8}$ yr (Figure 8(e)). For $\sigma_{C12\alpha} = -1$, on the other hand, those layers are still O-rich with some C (Figure 8(f)).

Similar differences are seen around $M_r = 1.5 M_\odot$. For $\sigma_{C12\alpha} = 0$, O burns out after $\tau = 10^{-2.0}$ yr and the layer becomes part of a Fe core after $\tau = 10^{-4.0}$ yr (Figure 8(c)). For $\sigma_{C12\alpha} = -1$, on the other hand, O shell burning maintains its activity until the collapse and the layer is OSi-rich (Figure 8(d)). This makes the Fe core mass for $\sigma_{C12\alpha} = 0$ ($1.51 M_\odot$) larger than for $\sigma_{C12\alpha} = -1$ ($1.36 M_\odot$) as seen in Figure 13.

4.2. Thermal and Dynamical Evolution of 28 M_\odot Star

In association with the chemical evolution of the $28 M_\odot$ star as described in the earlier subsection, the thermal and dynamical structures of the star evolve as follows with the significant dependence on $\sigma_{C12\alpha}$.

4.2.1. Evolution of Entropy and Temperature

Figure 14 shows the evolution of specific entropy at the center (s_c), $M_r = 1.5 M_\odot$ ($s_{1.5}$), $M_r = 2.0 M_\odot$ ($s_{2.0}$), and $M_r = 2.5 M_\odot$ ($s_{2.5}$) for $\sigma_{C12\alpha} = 0$ and -1 .

Figure 15 shows the evolution of temperatures at the center (T_c), $M_r = 1.5 M_\odot$ ($T_{1.5}$), $M_r = 2.0 M_\odot$ ($T_{2.0}$) and $M_r = 2.5 M_\odot$ ($T_{2.5}$) for both cases of $\sigma_{C12\alpha}$.

Even during central C-burning ($\tau \sim 10^3 - 10^1$ yr), s_c decreases because the neutrino energy loss rate exceeds the nuclear energy generation rate. Then the CO core contracts to increase T_c because of the gravothermal effect (Equation 11 - 12).

Around $\tau \sim 10^{1.2}$ yr, carbon in the central region is almost exhausted (Figure 8). Subsequent contraction of

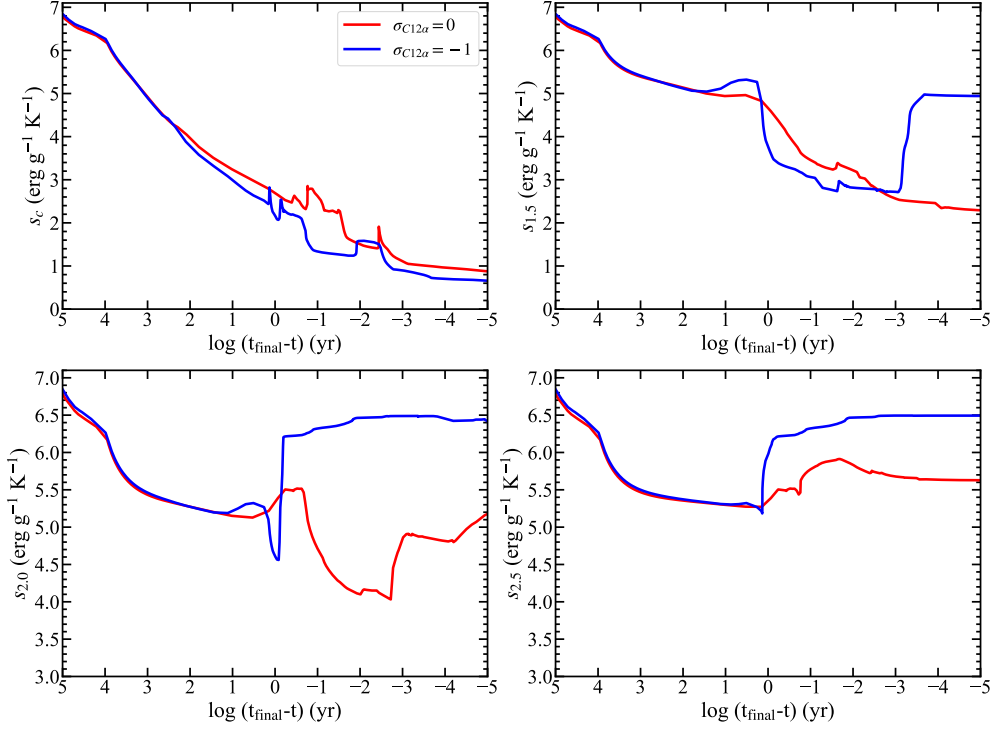
$M(\text{ZAMS}) = 28 M_{\odot}$


Figure 14. The time evolution of specific entropy in units of $\text{erg g}^{-1} \text{K}^{-1}$ at the center (s_c), $M_r = 1.5 M_{\odot}$ ($s_{1.5}$), $M_r = 2.0 M_{\odot}$ ($s_{2.0}$) and $M_r = 2.5 M_{\odot}$ ($s_{2.5}$) of $M(\text{ZAMS}) = 28 M_{\odot}$ star with $\sigma_{C12\alpha} = 0$ and -1 .

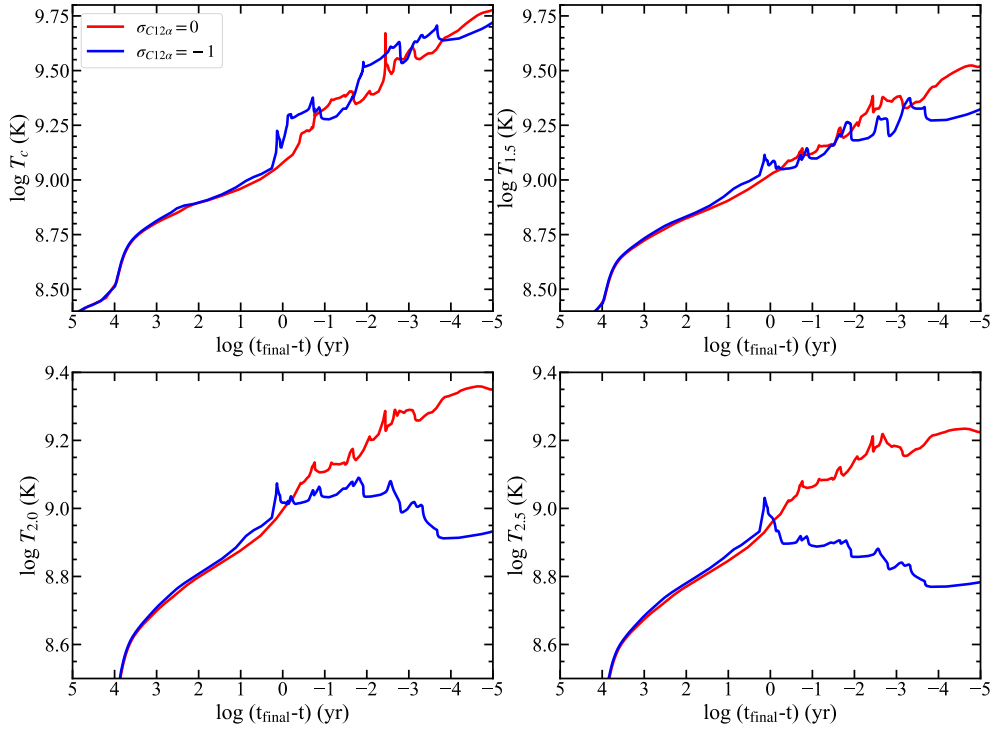
 $M(\text{ZAMS}) = 28 M_{\odot}$


Figure 15. The time evolution of temperature at the center (T_c), $M_r = 1.5 M_{\odot}$ ($T_{1.5}$), $M_r = 2.0 M_{\odot}$ ($T_{2.0}$) and $M_r = 2.5 M_{\odot}$ ($T_{2.5}$) of $M(\text{ZAMS}) = 28 M_{\odot}$ star with $\sigma_{C12\alpha} = 0$ and -1 .

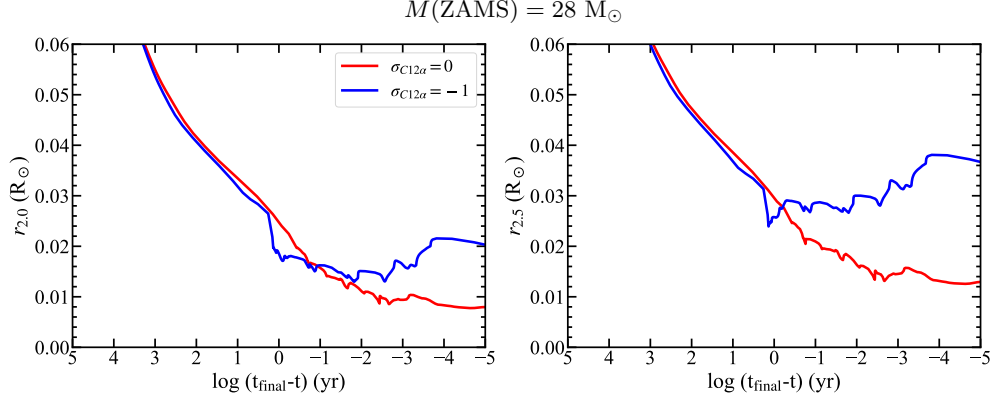


Figure 16. The time evolution of radius at $M_r = 2.0 M_{\odot}$ ($r_{2.0}$) and $M_r = 2.5 M_{\odot}$ ($r_{2.5}$) of $M(\text{ZAMS}) = 28 M_{\odot}$ star with $\sigma_{C12\alpha} = 0$ and -1 .

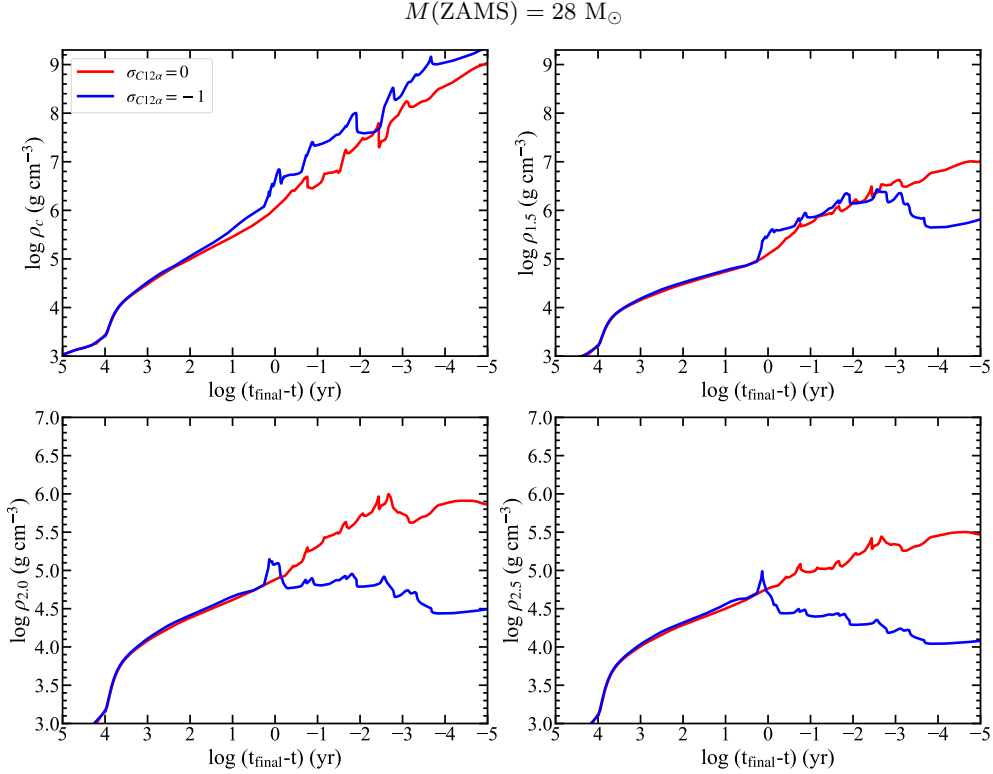


Figure 17. The time evolution of density at the center (ρ_c), $M_r = 1.5 M_{\odot}$ ($\rho_{1.5}$), $M_r = 2.0 M_{\odot}$ ($\rho_{2.0}$) and $M_r = 2.5 M_{\odot}$ ($\rho_{2.5}$) of $M(\text{ZAMS}) = 28 M_{\odot}$ star with $\sigma_{C12\alpha} = 0$ and -1 .

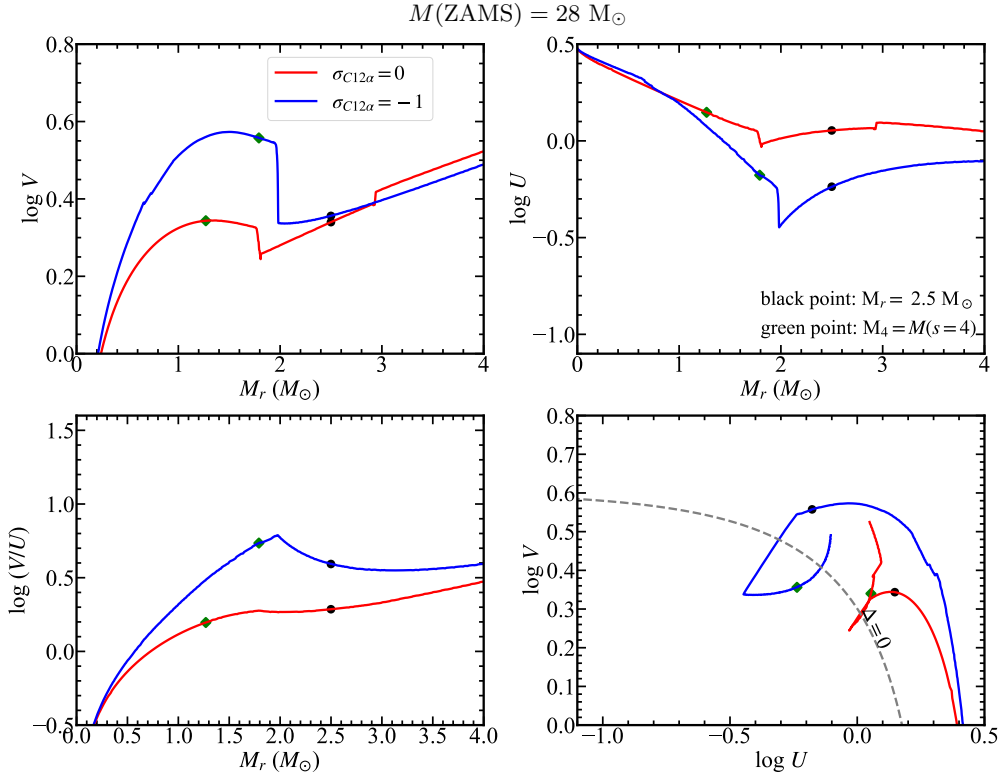


Figure 18. The $U - V$ curves of $28 M_{\odot}$ star at $\tau \sim 10^{-0.3}$ yr. The orange points represent the place where $M_r = 2.5 M_{\odot}$, while the green diamonds show the place where $M_r = M(s = 4)$.

the ONeMg core leads to the increase in the core temperatures (T_c , $T_{1.5}$, $T_{2.0}$, and $T_{2.5}$) (Figure 15). Then, the first C-shell burning is ignited radiatively for both cases of $\sigma_{C12\alpha}$ (Figure 7).

The second C-shell burning forms a convective shell for both cases (Table 4). The resulting heating is higher for $\sigma_{C12\alpha} = -1$ than 0 as seen in the slightly higher $s_{1.5}$ and $s_{2.0}$ around $\tau \sim 10^{1.2} - 10^0$ yr. This is because of larger $X(^{12}\text{C})$ in $\sigma_{C12\alpha} = -1$ although the difference is not so large.

A large difference between the two cases of $\sigma_{C12\alpha}$ appears around $\tau \sim 10^0$ yr near the end of central C-burning (Figure 8(a)).

For $\sigma_{C12\alpha} = -1$ (the blue lines), C-shell burning keeps a large convection zone above $M_r = 2.0 M_{\odot}$ as seen from the increase in $s_{2.0}$ and $s_{2.5}$ (the blue lines) near $\tau = 10^0$ yr. Such enhancement of $s_{2.0}$ occurs because $X(^{12}\text{C})$ is enhanced by mixing of outer C into the convective shell around $\tau \sim 10^0$ yr (Figure 8(f)). This convective C-shell burning continues to exist through Fe core-collapse. Because of this heating, the increase in $T_{2.0}$ is slow and $T_{2.5}$ is almost constant, in contrast to the increase in T_c and $T_{1.5}$ due to core contraction through Fe core-collapse.

For $\sigma_{C12\alpha} = 0$ (the red lines), on the other hand, $X(^{12}\text{C})$ at $M_r = 2.0 M_{\odot}$ is not enhanced (Figure 8(e)), so that the increase in $s_{2.0}$ is small from $\tau \sim 10^0$ to $10^{-0.6}$ yr. It even decreases after $\tau = 10^{-0.6}$ yr due to the neutrino energy loss. Then $T_{2.0}$ and $T_{2.5}$ continue to increase as in T_c and $T_{1.5}$.

4.2.2. Evolution of Radius and Density

The difference in the heating effect of C-shell burning appears in the difference in the evolution of core structure between the two cases.

Figure 16 shows the evolution of radius at $M_r = 2.0 M_{\odot}$ ($r_{2.0}$) and $M_r = 2.5 M_{\odot}$ ($r_{2.5}$) for $\sigma_{C12\alpha} = 0$ (the red line) and -1 (the blue lines).

The obvious differences appear at $\tau \sim 10^0$ yr, where $r_{2.5}$ stays almost constant for $\sigma_{C12\alpha} = -1$ (blue), while $r_{2.5}$ decreases along $r_{2.0}$ (red). This is due to the heating effect of C-shell burning above $M_r > 2.0 M_{\odot}$.

Figures 17 show the evolution of the density at the center (ρ_c), $M_r = 1.5 M_{\odot}$ ($\rho_{1.5}$), $M_r = 2.0 M_{\odot}$ ($\rho_{2.0}$) and $M_r = 2.5 M_{\odot}$ ($\rho_{2.5}$).

For both cases of $\sigma_{C12\alpha}$, ρ_c and $\rho_{1.5}$ continue to increase. For $\sigma_{C12\alpha} = 0$ (red), $\rho_{2.0}$ and $\rho_{2.5}$ continue to increase through the collapse. For $\sigma_{C12\alpha} = -1$ (blue), on the

other hand, $\rho_{2.0}$ keeps almost constant and $\rho_{2.5}$ even decreases.

These evolutions result in a rather large difference in the Fe core structure as will be discussed in subsection 4.2.5. We emphasize that enhancement of $X(^{12}\text{C})$ in the C shell burning causes such large differences in the thermal and dynamic structure of the presupernova core.

4.2.3. Effects of Oxygen Shell Burning

In the earlier sections, we have discussed the effect of O-shell burning on the core structure in detail. In Figure 14, 15 and 17 show a obvious increase in $s_{1.5}$ and decrease in $T_{1.5}$ and $\rho_{1.5}$ after $\log \tau = -3.8$ yr. These changes show that the expansion of the shell near $M_r = 1.5 M_\odot$ originate from the earlier mixes of O in $M_r = 1.5 M_\odot$, which has been mentioned in section 4.1.4.

4.2.4. U - V Curves

Nuclear Shell Burning and U-V Curves:

Nuclear shell burning has an important effect on the structure and evolution of stars because shell burning forms a sharp increase (almost a jump) in entropy and a convective shell. This is seen in the enhancement of $s_{2.0}$ and $s_{2.5}$ (Figure 14) due to C burning ($\log \tau \sim 0$ yr) and also $s_{1.5}$ due to O-burning ($\log \tau \sim -3.3$). Such an enhancement produces a sharp gradient of entropy as well as other physical quantities against M_r and r . This enhancement depends on $\sigma_{C12\alpha}$.

The strength of nuclear shell burning and the shell location can easily be seen in the U - V curves: See Figures 1 and 20 for the U - V curves of the whole star and that of the inner part ($M_r = 0 - 4 M_\odot$) at the collapse ($t = t_f$), respectively. Hereafter, we discuss the U - V curves of only the inner part ($M_r = 0 - 4 M_\odot$).

As seen from Equations 2, 3, and 4, the peaks of U and V indicate the locations of the steeper gradients of M_r and P against $\log r$ compared with the surrounding regions, while the peaks of V/U and $1/U$ indicate the location of the steeper gradients of P and r against $\log M_r$.

The loop of the $\log U$ - $\log V$ curve shows a relatively large jump across $\delta = 0$ (Equation 6), where U is minimum and thus, physical quantities have steep gradients concerning M_r . This implies that the location of the above jump is the core edge in M_r , which is the location of a nuclear burning shell.

The location of the bottom of the nuclear burning shell is indicated by the peaks of V/U , because nuclear shell burning produces a large entropy jump, thus creating a larger gradient of physical quantities concerning M_r .

The effect of the larger entropy jump in $\sigma_{C12\alpha} = -1$ (blue) than 0 (red) appears in the larger peak values of V (i.e., more centrally condensed) and V/U , the smaller minimum value of U (i.e., more extended), and the larger loop of $U - V$ in the blue lines than in the red lines.

Figures 18, 19, and 20 show the time evolution of the $U - V$ curves around $\tau = 10^{-0.3}$ yr, $10^{-3.3}$ yr, and t_f , respectively. At $\tau = 10^{-0.3}$ yr, strongest nuclear shell burning appears at $M_r = 2.0 M_\odot$ for $\sigma_{C12\alpha} = -1$, which is the bottom of convective C burning shell. At $\tau \sim 10^{-3.3}$ yr, the location of strongest nuclear burning shell moves to $M_r = 1.5 M_\odot$, which is O shell burning.

We note that these figures show that the maximum values of V , $1/U$ and V/U are larger in $\sigma_{C12\alpha} = -1$ than 0. This is mainly due to stronger C-shell burning with larger $X(^{12}\text{C})$.

$M(V/U_{\max})$, M_{eff} , Core Masses, and s_c :

Among these many peaks in the $U - V$ curves, M_r at the maximum V/U ($M(V/U_{\max})$) is the mass contained below the strongest burning shell.² Since V/U_{\max} appears at the most active nuclear burning shell, which forms the steepest pressure gradient, $M(V/U_{\max})$ can be regarded as M_{eff} in Equation 7. Then $M(V/U_{\max})$ is strongly related to the evolution of the core as described in Equation 7, thus being useful to discuss the explodability in the subsequent sections.

To see the dependence of $M(V/U_{\max})$ on $\sigma_{C12\alpha}$, Figure 21 shows the time evolution of core masses of Fe ($M(\text{Fe})$), Si ($M(\text{Si})$), and O ($M(\text{O})$), $M_r = M(s = 4)$ (M_4), and $M(V/U_{\max})$ for $M(\text{ZAMS}) = 28 M_\odot$ with $\sigma_{C12\alpha} = 0$ (left) and -1 (right). It is seen that $M(V/U_{\max})$ is smaller for $\sigma_{C12\alpha} = -1$ than 0, mainly because of strong C-shell burning at $M_r = 2 M_\odot$. This smaller $M(V/U_{\max})$ produces the smaller core masses of O, Si, and Fe. We also note that $M(\text{Si})$ (i.e., M_r at the O-burning shell) and M_4 are almost identical to $M(V/U_{\max})$ near the final stage so that these masses are smaller for $\sigma_{C12\alpha} = -1$ than 0.

The effect of smaller $M(V/U_{\max})$ (and thus M_{eff}) for $\sigma_{C12\alpha} = -1$ than 0 can be seen in the evolution of $\log T_c - \log \rho_c$ (Figure 2). Here s_c is smaller (and thus ρ_c is higher for the same T_c) for $\sigma_{C12\alpha} = -1$ than 0 according to Equations 11 and 9. Such evolutions of smaller s_c and

² Hereafter, we denote the maximum V/U , i.e., $(V/U)_{\max}$, as V/U_{\max} .

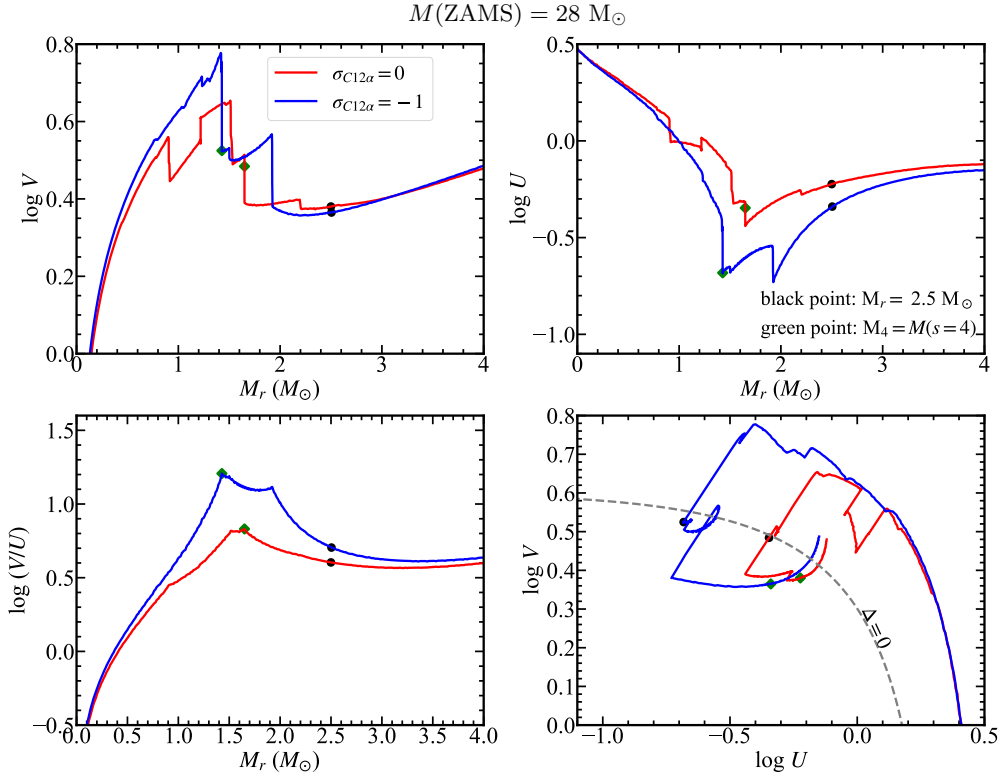


Figure 19. The $U - V$ curves of $28 M_{\odot}$ star at $\tau \sim 10^{-3.3}$ yr. The orange points represent the place where $M_r = 2.5 M_{\odot}$, while the green diamonds show the place where $M_r = M(s=4)$.

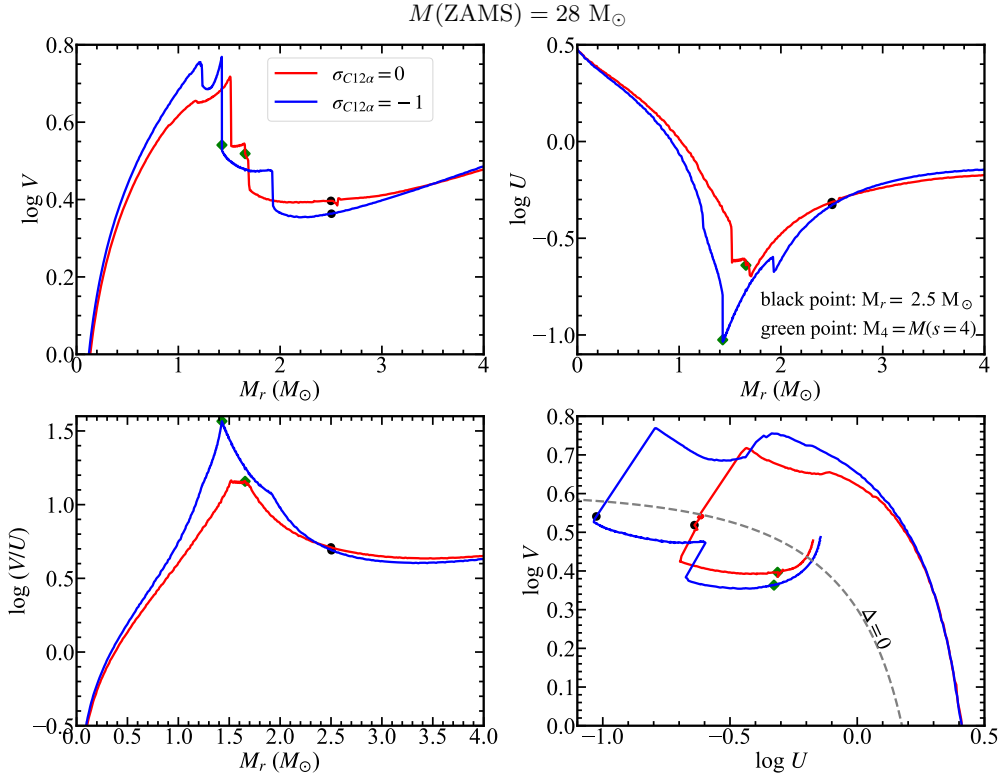


Figure 20. The $U - V$ curves of $28 M_{\odot}$ star at $\tau = t_f$. The orange points represent the place where $M_r = 2.5 M_{\odot}$, while the green diamonds show the place where $M_r = M(s=4)$.

higher ρ_c (at the same T_c) are seen in Figures 14 and 17, respectively.

Regarding the explodability, the maximum values of $\log V/U$ are 1.6 and 1.1 for $\sigma_{C12\alpha} = -1$ and 0, respectively,

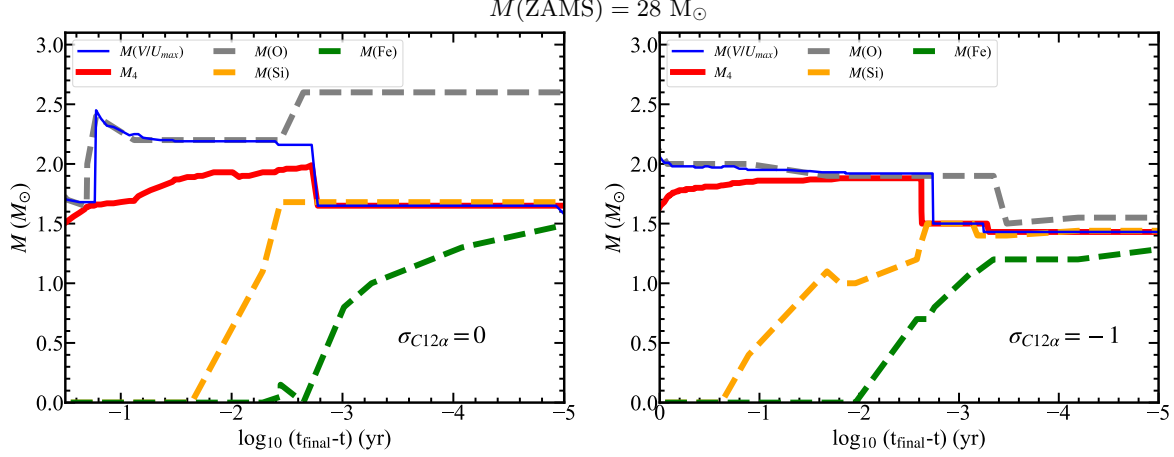


Figure 21. The time evolution of core masses of Fe, $M(\text{Fe})$, Si, $M(\text{Si})$, and O, $M(\text{O})$, $M_r = M(s=4)$, M_4 , and $M(V/U_{\text{max}})$ for $M(\text{ZAMS}) = 28 M_{\odot}$ with $\sigma_{C12\alpha} = 0$ (left) and -1 (right). The core masses are shown with the thick dashed lines, and M_4 is the thick solid line. $M(V/U_{\text{max}})$ is indicated by the thin solid line. Both $M(\text{Si})$ and M_4 are overlapped with $M(V/U_{\text{max}})$ near the final stage.

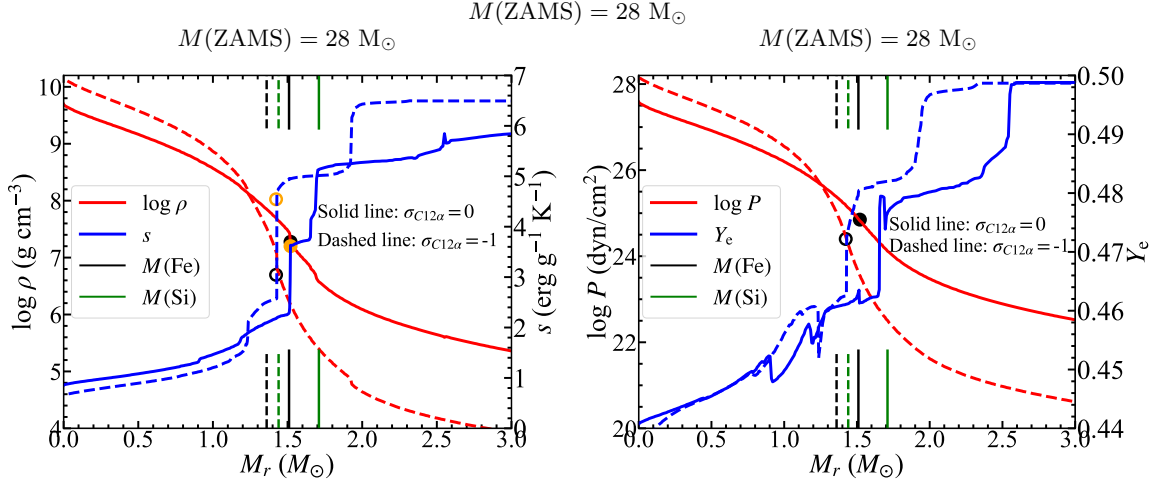


Figure 22. (Left) The density and entropy distribution of a star with $M(\text{ZAMS}) = 28 M_{\odot}$ for $\sigma_{C12\alpha} = 0$ (solid line) and -1 (dashed line). The green and black lines show the edges of Si and Fe cores, respectively. The steepest gradients of $\log \rho$ and s , which corresponds to the peak of $\log(V/U)$, are marked respectively by the filled black and orange circles (for $\sigma_{C12\alpha} = 0$) and the open black and orange circles (for $\sigma_{C12\alpha} = -1$). (Right) Same as Left but for the pressure and Y_e .

which show the difference in the steepness of $\log P$ with respect to M_r as seen in Figure 22 below. This indicates that the star with $\sigma_{C12\alpha} = -1$ is easier to explode, as will be discussed later.

Thus, the $U - V$ curves are handy diagrams to indicate the location of the critical points, such as the strongest nuclear shell burning and M_4 by showing “quantitatively” the gradients of quantities with respect to M_r and r .

4.2.5. Presupernova Structure and Compactness

Figure 22 (left) shows distributions of the $\log \rho$ and s at the beginning of the collapse ($\tau = 0$ yr: $t = t_f$), i.e., at $\log T_c$ (K) = 10.0, where the dashed lines and solid lines represent $\sigma_{C12\alpha} = 0$ and -1 , respectively. The

green lines and black lines show the outer edges of the Si core and Fe core, respectively, which are defined as the locations where the energy generation rates of shell O burning and shell Si burning is the highest. Similar distributions of $\log P$ and Y_e are shown in Figure 22 (right).

It is seen that the gradients of $\log \rho$ and $\log P$ with respect to M_r are much steeper for $\sigma_{C12\alpha} = -1$ than $\sigma_{C12\alpha} = 0$. Also, $\log \rho_c$ is higher and s_c is lower for $\sigma_{C12\alpha} = -1$ than 0 because of smaller $M(V/U_{\text{max}})$ (i.e., smaller M_{eff}) for $\sigma_{C12\alpha} = -1$ as discussed in the subsection 4.2.4 on the $U - V$ curves based on Equations 11 and 9.

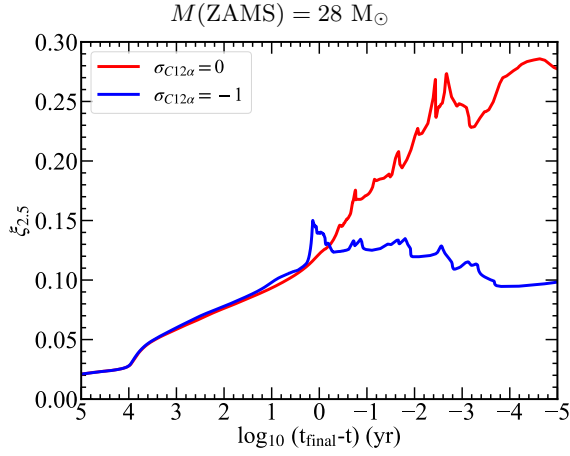


Figure 23. The time evolution of $\xi_{2.5}$ for $M(\text{ZAMS}) = 28 M_{\odot}$ and $\sigma_{C12\alpha} = 0$ and -1 .

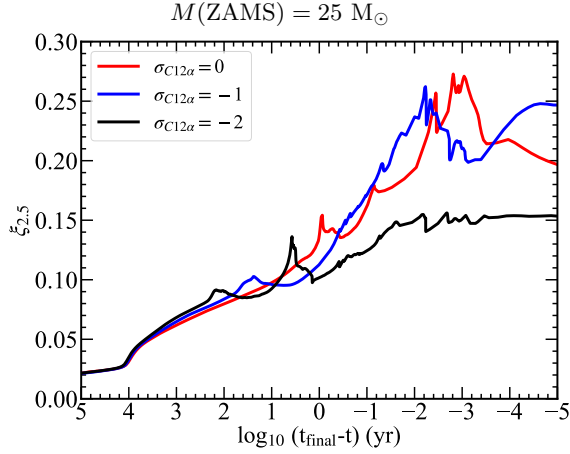


Figure 24. The time evolution of $\xi_{2.5}$ for $M(\text{ZAMS}) = 25 M_{\odot}$ and $\sigma_{C12\alpha} = 0, -1$ and -2 , respectively.

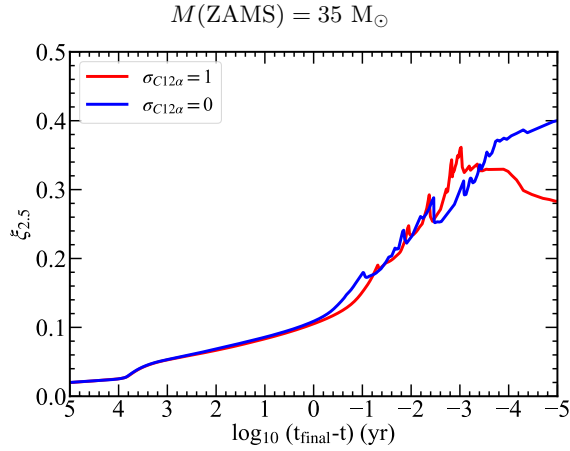


Figure 25. The time evolution of $\xi_{2.5}$ for $M(\text{ZAMS}) = 35 M_{\odot}$ with $\sigma_{C12\alpha} = 1$ and 0 .

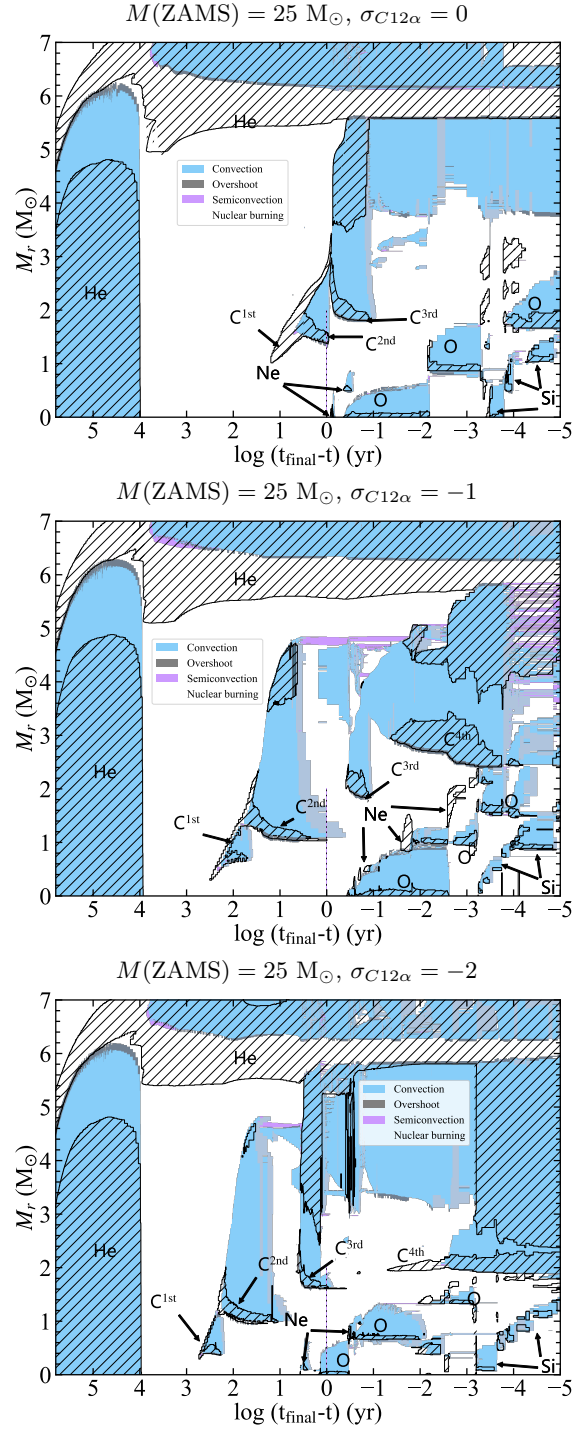


Figure 26. Same as Figure 7, but for stars with $M(\text{ZAMS}) = 25 M_{\odot}$ for $\sigma_{C12\alpha} = 0$ (top), -1 (median) and -2 (bottom).

The steepest gradient of $\log P$ with respect to M_r corresponds to the maximum $\log(V/U)$ (Figure 20) and is marked by cyan ($\sigma_{C12\alpha} = 0$) and black ($\sigma_{C12\alpha} = -1$) filled circles. The corresponding steepest points in $\log \rho$ (filled circles) and s (open circles) are also indicated.

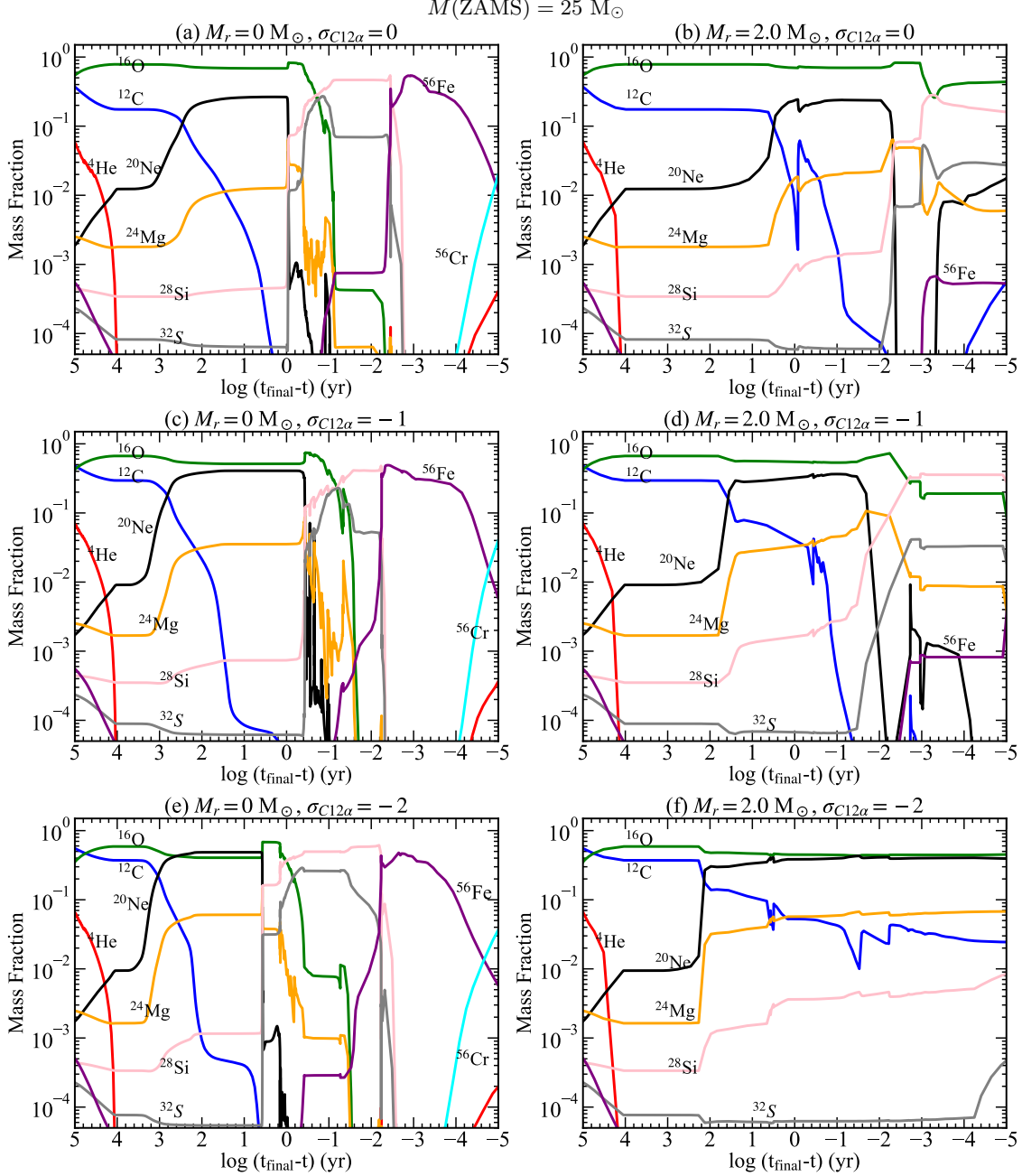


Figure 27. The time evolution of the mass fractions of some isotopes for for $25 M_{\odot}$ stars at the center (left), and $M_r = 2.0 M_{\odot}$ (right) from He burning through Fe core-collapse for $\sigma_{C12\alpha} = 0$ (upper), -1 (center), and -2 (lower).

We note that s at V/U_{\max} is close to 4 but not exactly 4 (see also Figure 40 in the later section). However, M_4 is almost identical to $M(V/U_{\max})$ because of the extremely sharp gradient of s due to entropy production by O-shell burning.

The difference in the core structure also appears in the evolution of the compactness parameter $\xi_{2.5}$ after $\tau > 10^{0.2}$ yr (Figure 23). For $\sigma_{C12\alpha} = 0$ (red), $\xi_{2.5}$ continues to increase to reach 0.28 at $\tau = -5$ yr. For $\sigma_{C12\alpha} = -1$ (blue), on the other hand, $\xi_{2.5}$ decreases from 0.15 to

0.10 at $\tau > 10^{0.2}$ yr. It is obvious that the core with $\sigma_{C12\alpha} = 0$ (red) is much more compact with larger $\xi_{2.5}$ than $\sigma_{C12\alpha} = -1$ (blue). The difference in $\xi_{2.5}$ stems exactly from the difference in the evolution of radius, where $r_{2.5}$ stays almost constant as shown in Figure 16.

Such a difference in the density and pressure distributions and the compactness parameter would lead to significant differences in the core-collapse hydrodynamics and the explosability, as well as associated explosive nucleosynthesis.

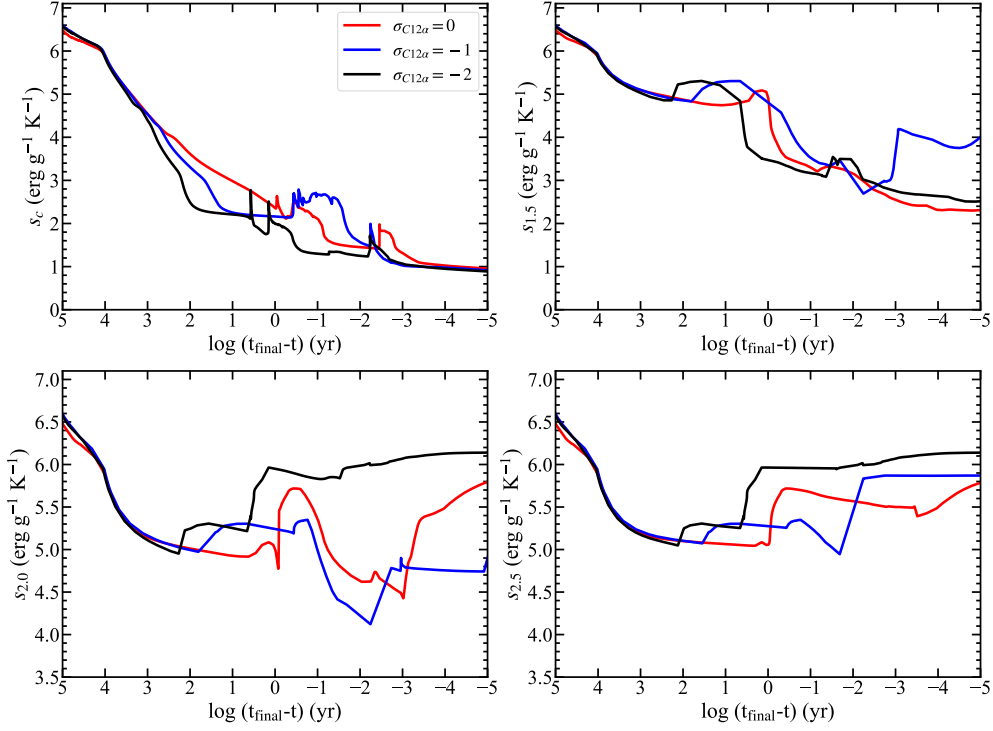
$M(\text{ZAMS}) = 25 M_{\odot}$


Figure 28. The time evolution of specific entropy at the center (s_c), $M_r = 1.5 M_{\odot}$ ($s_{1.5}$), $M_r = 2.0 M_{\odot}$ ($s_{2.0}$) and $M_r = 2.5 M_{\odot}$ ($s_{2.5}$) of stars with $M(\text{ZAMS}) = 25 M_{\odot}$ for $\sigma_{C12\alpha} = 0$ –1 and –2.

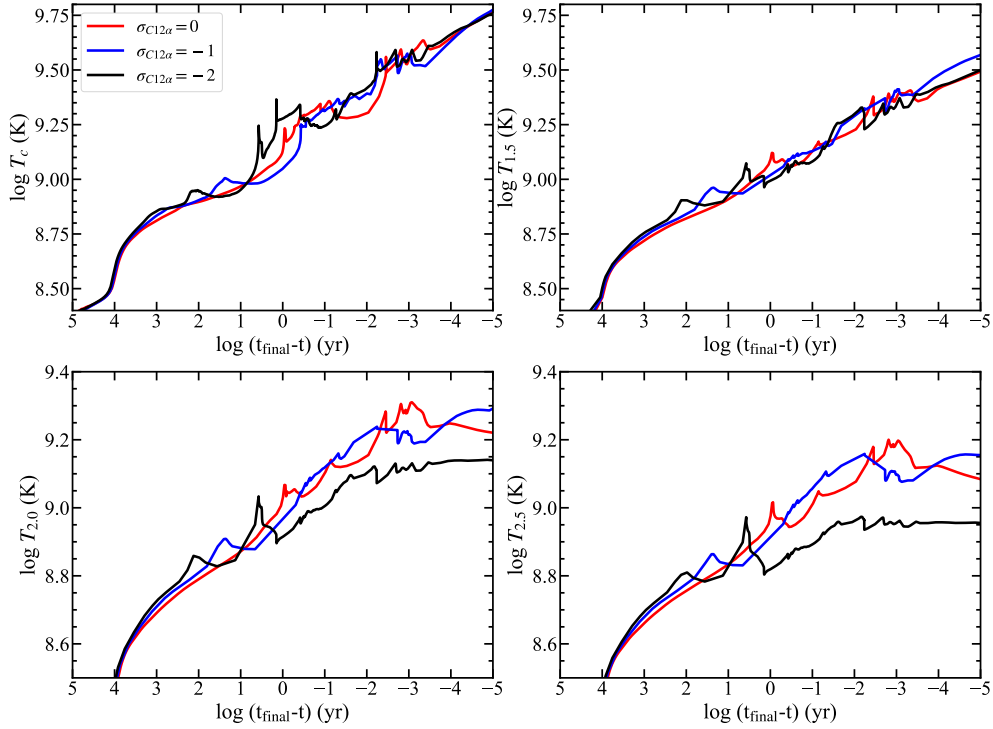
 $M(\text{ZAMS}) = 25 M_{\odot}$


Figure 29. The time evolution of temperature at the center (T_c), $M_r = 1.5 M_{\odot}$ ($T_{1.5}$), $M_r = 2.0 M_{\odot}$ ($T_{2.0}$) and $M_r = 2.5 M_{\odot}$ ($T_{2.5}$) of stars with $M(\text{ZAMS}) = 25 M_{\odot}$ for $\sigma_{C12\alpha} = 0$ –1 and –2.

4.3. Evolutions of 25 and 35 M_{\odot} Stars

For the 28 M_{\odot} star, we have shown how the evolution of $\xi_{2.5}$ is affected by $\sigma_{C12\alpha}$. We also have investigated how the effect of $\sigma_{C12\alpha}$ depends on $M(\text{ZAMS})$. In Figure 24, we show that the evolution of $\xi_{2.5}$ in the 25 M_{\odot} stars for three cases of $\sigma_{C12\alpha} = 0, -1$ and -2 . We also show in Figure 25 the evolution of $\xi_{2.5}$ in the 35 M_{\odot} stars for the cases of $\sigma_{C12\alpha} = 0$ and 1 . This figure shows the effect of the case of a very low C/O ratio originating from a large $M(\text{ZAMS})$ and a large $^{12}\text{C}(\alpha, \gamma)^{16}\text{O}$ rate. In the following sections, we will discuss the evolutions of the 25 and 35 M_{\odot} stars to clarify how these differences in $\xi_{2.5}$ appear.

4.3.1. Chemical Evolution of 25 M_{\odot} Star

The following figures show the chemical evolution of the 25 M_{\odot} stars for $\sigma_{C12\alpha} = 0, -1$ and -2 . Figure 26 shows Kippenhahn diagrams. The time

$\tau = t_f - t$ is measured from the final stage of t_f (denoted as t_{final} in the axes of Figures) where the central temperature reaches $\log T_c \text{ (K)} = 10.0$ as in the 28 M_{\odot} star.

Reaction rate dependence:

Figure 27 shows the evolution of the mass fractions of several isotopes at the center (left) and $M_r = 2.0 M_{\odot}$ (right) from He burning through Fe core-collapse. It is seen that the chemical evolution at the center (a, c, e) does not much depend on $\sigma_{C12\alpha}$, while the evolution at $M_r = 2.0 M_{\odot}$ (b, d, f) is affected by $\sigma_{C12\alpha}$ owing to the strength of C shell burning ($\tau = 10^{0.6} - 10^{-0.5}$ yr). and O shell burning ($\tau = 10^{-2} - 10^{-3}$ yr).

When He is exhausted in the core ($\tau \sim 10^{4.5}$), $X(^{12}\text{C})$ at $M_r = 2.0 M_{\odot}$ is larger for smaller $\sigma_{C12\alpha}$. For $\sigma_{C12\alpha} = -2$, $X(^{12}\text{C})$ is large enough for the C burning convective shell to reach the overlying C-rich layer. Resulting convective mixing enhances $X(^{12}\text{C})$ and make C-shell burning active. For $\sigma_{C12\alpha} = 0$ and -1 , such C-mixing does not occur and ^{12}C is exhausted at $M_r = 2.0 M_{\odot}$. Then, C-shell burning becomes inactive. Such inactivity of C-shell burning for $\sigma_{C12\alpha} = -1$ in the 25 M_{\odot} star is different from the 28 M_{\odot} star in which C-shell burning is active until core-collapse for $\sigma_{C12\alpha} = -1$.

The main difference in C-shell burning with $\sigma_{C12\alpha} = -2$ from $\sigma_{C12\alpha} = -1$ and 0 is that, because of larger $X(^{12}\text{C})$ after He exhaustion in $\sigma_{C12\alpha} = -2$, C shell burning at $M_r \sim 2.0 M_{\odot}$ is active and convective during the evolution from central O burning to Fe core-collapse (Figure 26). Resultant heating of shell burning causes the expansion of the outer layer as seen from $r_{2.5}$ and $r_{2.0}$ (Figure 30) and $\rho_{2.5}$ and $\rho_{2.0}$ (Figure 31).

Figures 23 and 24 show the mass-dependence of $\xi_{2.5}$ for $M(\text{ZAMS}) = 25$ and $28 M_{\odot}$, respectively. There appears to be a difference at $\tau < 10^{-3.5}$ yr for $\sigma_{C12\alpha} = 0$.

This difference stems from *O-shell burning*. For the 25 M_{\odot} star, convective mixing of fresh O from the outer layer occurs at the shell near $M_r = 2.0 M_{\odot}$ as seen from the almost constant $X(\text{O})$ in Figure 27(b). Then O-shell burning continues to be active. This is different from the 28 M_{\odot} star with $\sigma_{C12\alpha} = 0$ where O shell burning is weak because $X(\text{O}) < 0.1$ at $M_r = 2.0 M_{\odot}$ around $\tau < 10^{-3}$ yr (Figure 8(e)). Such a difference in O-shell burning leads to the difference in $\xi_{2.5}$ between the 25 and 28 M_{\odot} stars even for the same $\sigma_{C12\alpha} = 0$.

4.3.2. Thermal and Dynamical Evolution of 25 M_{\odot} Star

Entropy:

Figure 28 shows the evolution of specific entropy at the center (s_c), $M_r = 1.5 M_{\odot}$ ($s_{1.5}$), $M_r = 2.0 M_{\odot}$ ($s_{2.0}$), and $M_r = 2.5 M_{\odot}$ ($s_{2.5}$).

We should note that $s_{2.0}$ is enhanced around $\tau \sim 10^{0.6}$ yr for $\sigma_{C12\alpha} = -2$ (black) owing to the mixing of C. This is similar to the increase in $s_{2.0}$ in the 28 M_{\odot} star with $\sigma_{C12\alpha} = -1$.

Note also that the decrease in $\xi_{2.5}$ during $\tau \sim 10^{-2.3} - 10^{-3}$ yr for $\sigma_{C12\alpha} = -1$ (blue) and after $\tau \sim 10^{-3}$ for $\sigma_{C12\alpha} = 0$ (red) are originated from the increase in $s_{2.0}$ owing to O-mixing (see Figure 27 (b) and (d)). Such an increase is also seen in the 28 M_{\odot} star in $s_{2.0}$ after $\tau \sim 10^{-2.8}$ with $\sigma_{C12\alpha} = 0$ and $s_{1.5}$ after $\tau \sim 10^{-3}$ with $\sigma_{C12\alpha} = -1$.

Temperature:

Figure 29 shows the evolution of temperature at the center (T_c), $M_r = 1.5 M_{\odot}$ ($T_{1.5}$), $M_r = 2.0 M_{\odot}$ ($T_{2.0}$) and $M_r = 2.5 M_{\odot}$ ($T_{2.5}$).

Note that $T_{2.0}$ reaches the O-burning temperature for $\sigma_{C12\alpha} = 0$ (red) and -1 (blue). For $\sigma_{C12\alpha} = -2$, $T_{2.0}$ and $T_{2.5}$ increase slowly staying at the C-burning temperature.

Radius:

Figure 30 shows the evolution of radius at $M_r = 2.0 M_{\odot}$ ($r_{2.0}$) and $M_r = 2.5 M_{\odot}$ ($r_{2.5}$). These radii generally decrease during the core contraction. However, $r_{2.5}$ increases for $\sigma_{C12\alpha} = -2$ at $\tau \sim 10^{0.4} - 10^0$ yr because of the heating effect of C shell burning. This is the reason that the compactness parameter of $\sigma_{C12\alpha} = -2$ decreases during that period (Figure 23 (right)).

Density:

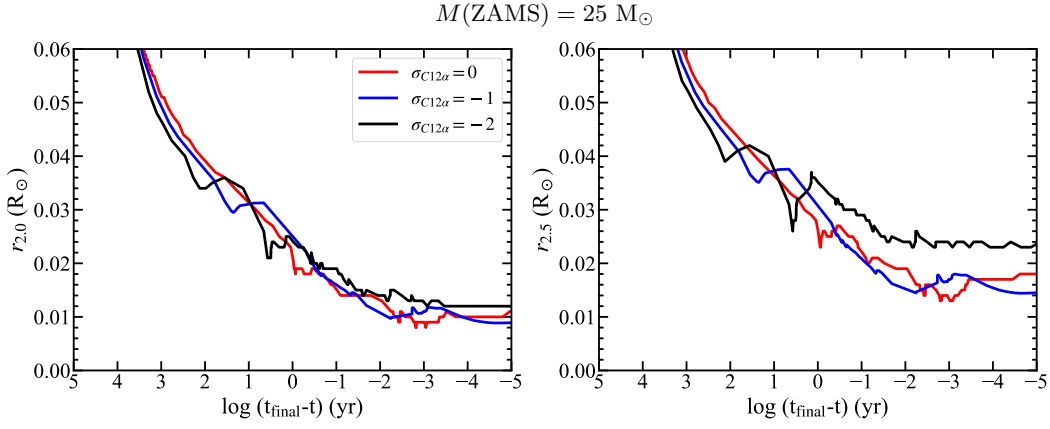


Figure 30. The time evolution of radius at $M_r = 2.0 M_\odot$ ($\rho_{2.0}$) and $M_r = 2.5 M_\odot$ ($\rho_{2.5}$) of stars with $M(\text{ZAMS}) = 25 M_\odot$ for $\sigma_{C12\alpha} = 0, -1$, and -2 .

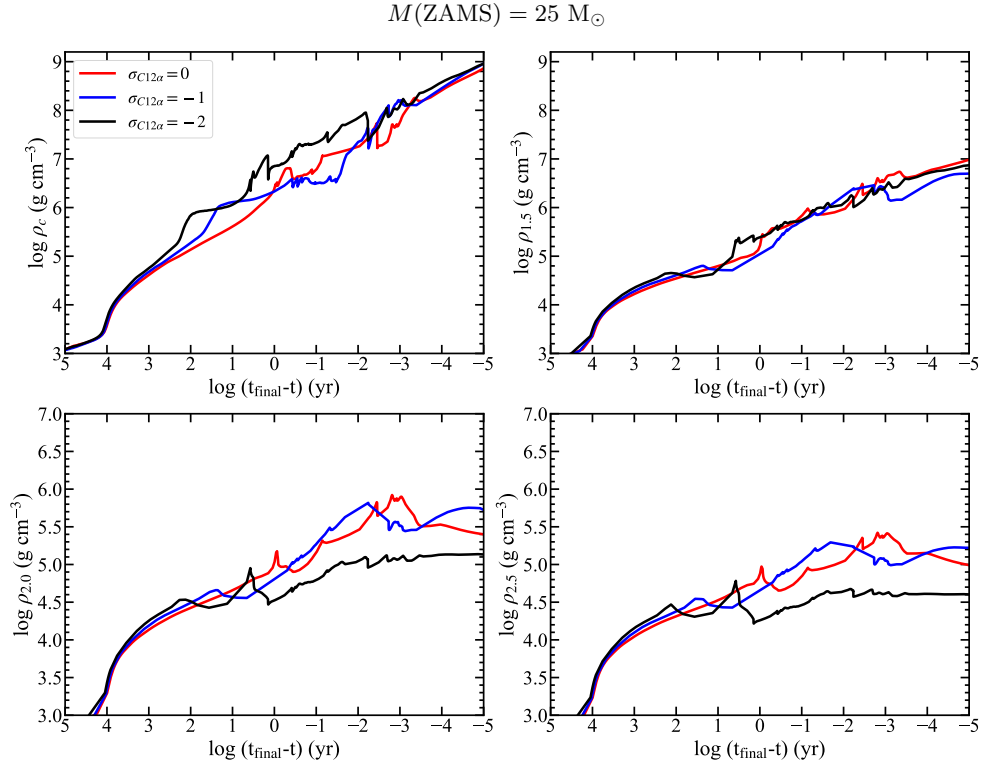


Figure 31. The time evolution of density at the center (ρ_c), $M_r = 1.5 M_\odot$ ($\rho_{1.5}$), $M_r = 2.0 M_\odot$ ($\rho_{2.0}$) and $M_r = 2.5 M_\odot$ ($\rho_{2.5}$) of stars with $M(\text{ZAMS}) = 25 M_\odot$ for $\sigma_{C12\alpha} = 0, -1$ and -2 .

Figure 31 shows the evolution of densities at the center (ρ_c), $M_r = 1.5 M_\odot$ ($\rho_{1.5}$), $M_r = 2.0 M_\odot$ ($\rho_{2.0}$), and $M_r = 2.5 M_\odot$ ($\rho_{2.5}$). These figures show that the evolution of the density at each layer of the $25 M_\odot$ stars is not so different between $\sigma_{C12\alpha} = 0$ and -1 , in contrast to the large difference for the $28 M_\odot$ star. As a result, the density and entropy distributions at $t = t_f$ are not so different between $\sigma_{C12\alpha} = 0$ and -1 (Figure 32).

For $\sigma_{C12\alpha} = -2$, on the other hand, the density evolution and the final distributions of the density and en-

trophy are different, being similar to the $28 M_\odot$ stars with $\sigma_{C12\alpha} = -1$ as seen in Figures 32.

4.3.3. Presupernova Structure and U-V Curves of $25 M_\odot$ Stars

Behaviors of shell burning at $\tau = t_f$ are shown in the $U - V$ curves in Figure 33. For $\sigma_{C12\alpha} = 0$ and -2 , maximum of V/U -curves appears near $M_r = 1.7 M_\odot$, which is the bottom of the O burning shell. On the other hand, maximum for $\sigma_{C12\alpha} = -1$ appears between the O-burning shell and the Si-burning shell ($M_r = 1.5$

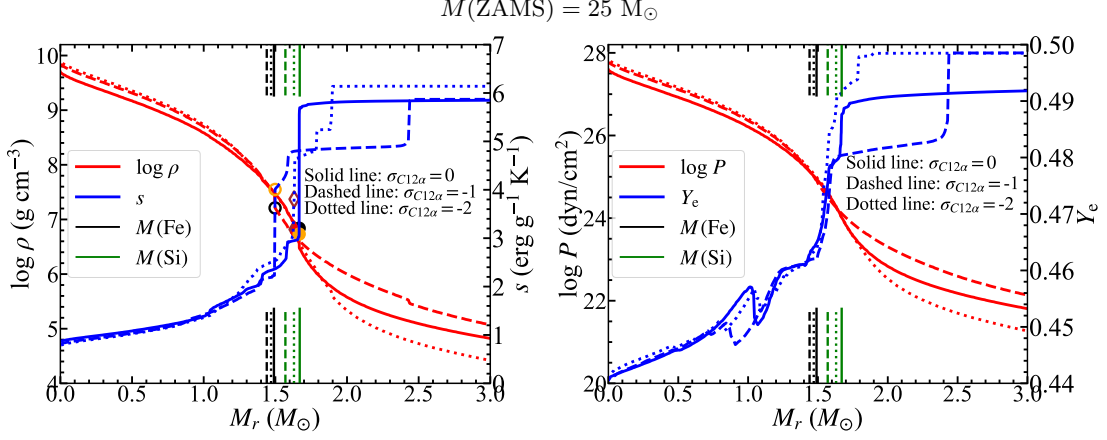


Figure 32. Same as Figure 22, but for $M(\text{ZAMS}) = 25 M_{\odot}$ and $\sigma_{C12\alpha} = 0, -1$ and -2 .

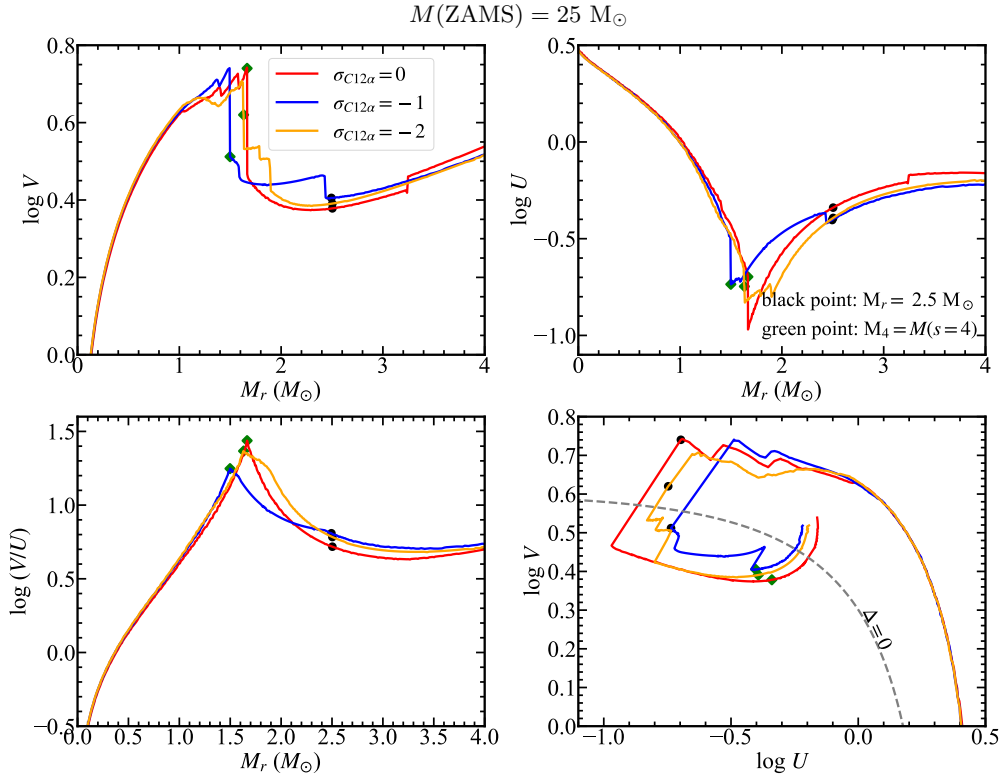


Figure 33. The $U - V$ curves of $25 M_{\odot}$ star at $\tau = t_f$. The orange points represent the place where $M_r = 2.5 M_{\odot}$, while the green diamonds show the place where $M_r = M(s = 4)$.

M_{\odot}). Similar to the $28 M_{\odot}$ models, these peaks in V/U -curves are located at M_4 and correspond to the steepest gradient of $\log P$ with respect to M_r (see Fig 32). The maximum values of $\log V/U$ in $25 M_{\odot}$ models are 1.44, 1.25, and 1.37 for $\sigma_{C12\alpha} = 0, -1$, and -2 , respectively. As will be discussed later, these values of the steepness are marginal for the criterion of the explosion vs. collapse.

For $35 M_{\odot}$ stars, we investigate the case of $\sigma_{C12\alpha} = 1$, i.e., the effect of the low C/O ratio. Figure 25 shows that $\xi_{2.5}$ increases up to 0.4 for $\sigma_{C12\alpha} = 0$ but decreases down to 0.28 for $\sigma_{C12\alpha} = 1$ from $\tau = 10^{-3}$ to 10^{-5} yr.

As shown in Figure 36 of Kippenhahn diagrams, the behavior of C shell burning is similar between these cases. Both models ignite C shell burning at $M_r \sim 2 M_{\odot}$ and the convection extends to $M_r \sim 6.5 M_{\odot}$. After $\tau \sim 10^{-2}$ yr, the C burning shell moves to $M_r \sim 4.7 M_{\odot}$ ($4.0 M_{\odot}$)

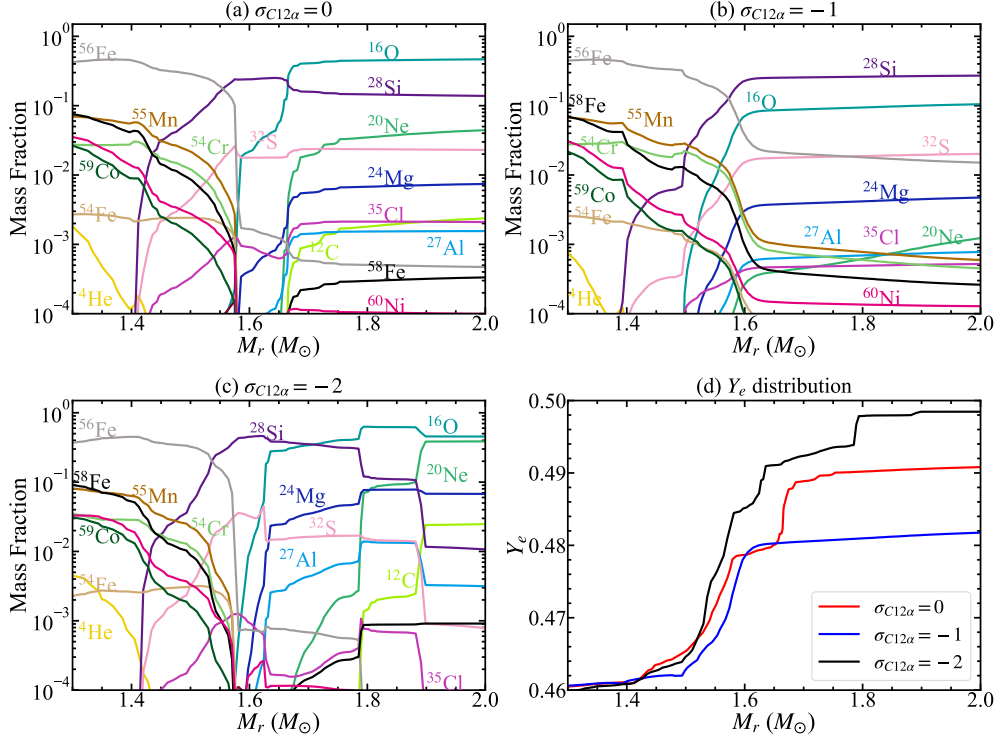
$M(\text{ZAMS}) = 25 M_{\odot}$


Figure 34. The abundance distributions in stars with $M(\text{ZAMS}) = 25 M_{\odot}$ for $\sigma_{C12\alpha} = 0$ (a), -1 (b) and -2 (c) at $\log T_c$ (K) = 10 ($t = t_f$). Also, Y_e distribution is shown (d).

and forms an oxygen core of $M(\text{O}) = 4.0 M_{\odot}$ ($3.2 M_{\odot}$) for $\sigma_{C12\alpha} = 1$ ($\sigma_{C12\alpha} = 0$).

Owing to the low $X(^{12}\text{C})$ in both models, the heating effect of C shell burning is weak. In Figure 25, evolutions of $\xi_{2.5}$ do not show a large difference between the two models up to $\tau \sim 10^{-3}$ yr.

However, $\xi_{2.5}$ decrease after $\tau = 10^{-3}$ yr for $\sigma_{C12\alpha} = 1$. This is due to the heating effect of O shell burning, which extends from $M_r = 2.0$ to $4.0 M_{\odot}$. Figure 37 (b) shows that $X(^{16}\text{O})$ at $M_r = 2 M_{\odot}$ decreases from $\tau = 10^{-2.3}$ yr to $10^{-2.8}$ yr due to O shell burning and increases after $\tau = 10^{-2.8}$ yr due to mixing of oxygen from outer layers. After O shell burning is ignited, the layers above $M_r = 2.0 M_{\odot}$ begin to expand as seen from the time evolution of $\log T$ at $M_r = 2.0 M_{\odot}$ and $M_r = 2.5 M_{\odot}$ in Figure 38.

The core structure ($\log \rho$ and s) at the final stage for these two models are compared in Figure 35. The steepest gradient of density and specific entropy occurs around $s = 3\text{--}4 \text{ erg g}^{-1} \text{ K}^{-1}$ just below the O burning shell. We conclude that the heating effect of O shell burning is important when and where $X(^{12}\text{C})$ is low enough.

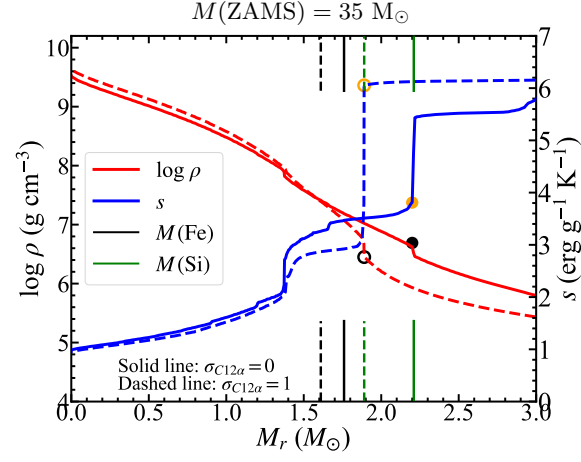


Figure 35. Same as Figure 22 (left), but for stars with $M(\text{ZAMS}) = 35 M_{\odot}$ and $\sigma_{C12\alpha} = 1$ and 0.

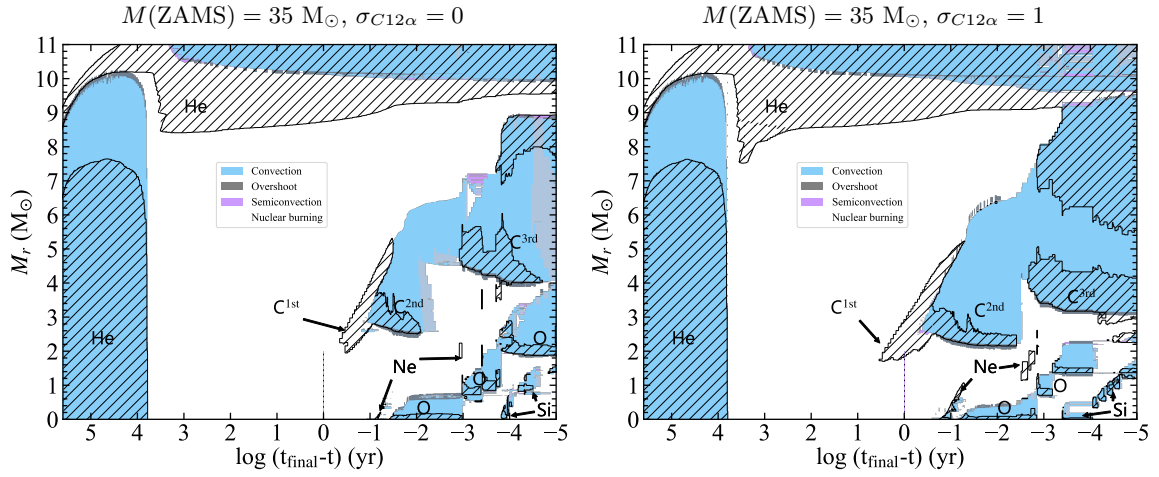


Figure 36. Same as Figure 7 but for stars with $M(\text{ZAMS}) = 35 M_{\odot}$ and $\sigma_{C12\alpha} = 1$ (left) and 0 (right).

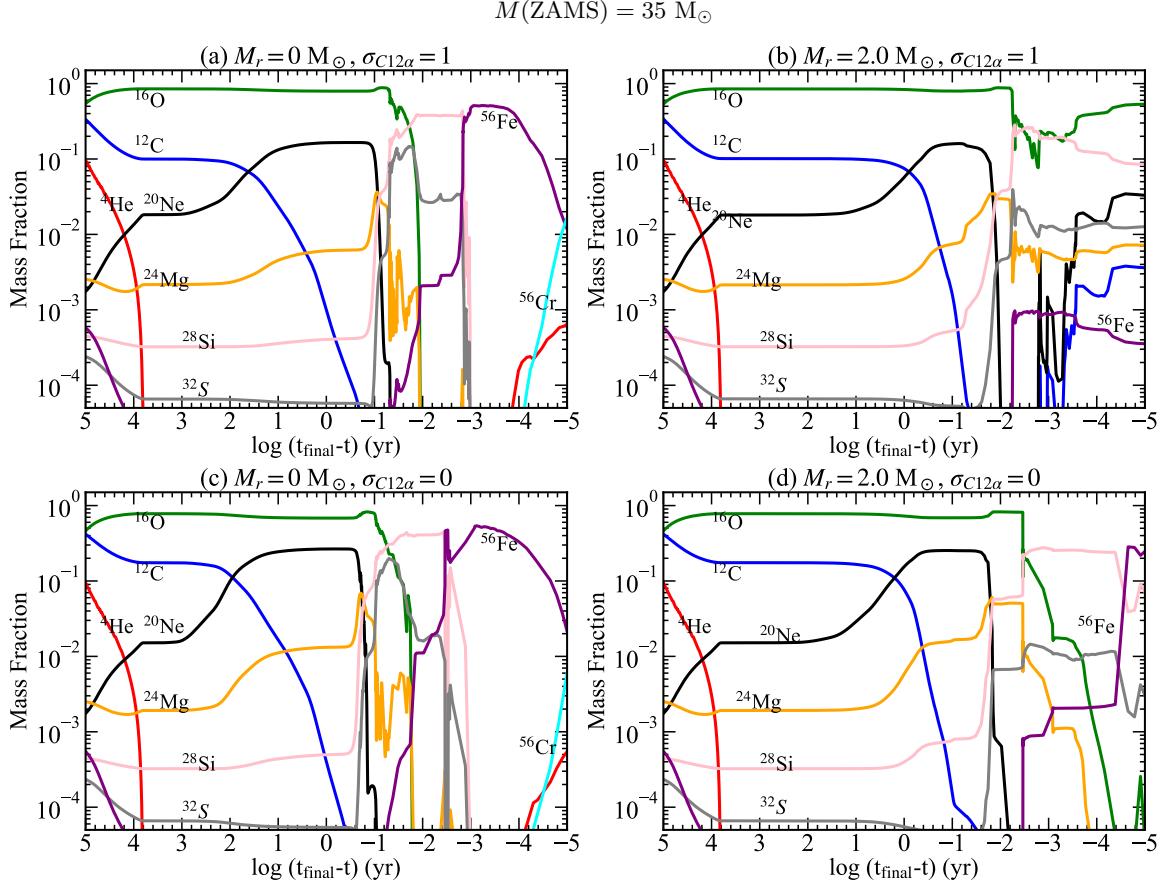


Figure 37. The time evolution of the mass fractions of some isotopes at the center and $M_r = 2.0 M_{\odot}$ for a star with $M(\text{ZAMS}) = 35 M_{\odot}$ for $\sigma_{C12\alpha} = 1$ (top) and 0 (bottom).

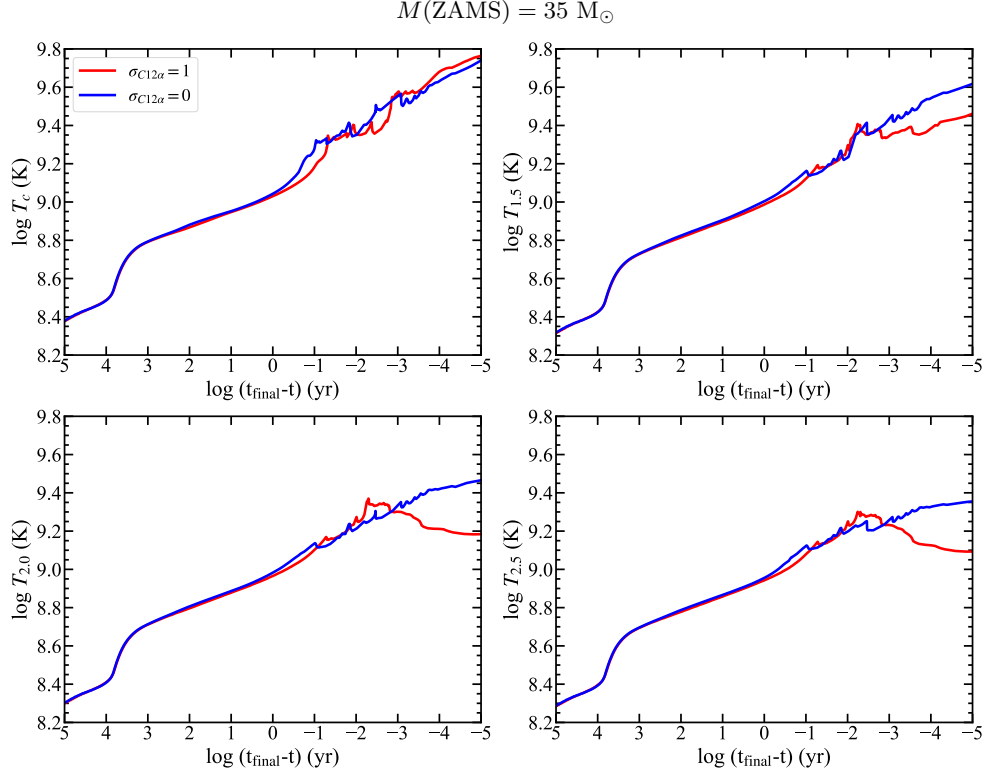


Figure 38. The time evolution of temperatures at the center (T_c), $M_r = 1.5 M_{\odot}$ ($T_{1.5}$), $M_r = 2.0 M_{\odot}$ ($T_{2.0}$) and $M_r = 2.5 M_{\odot}$ ($T_{2.5}$) of stars with $M(\text{ZAMS}) = 35 M_{\odot}$ for $\sigma_{C12\alpha} = 1$ and 0.

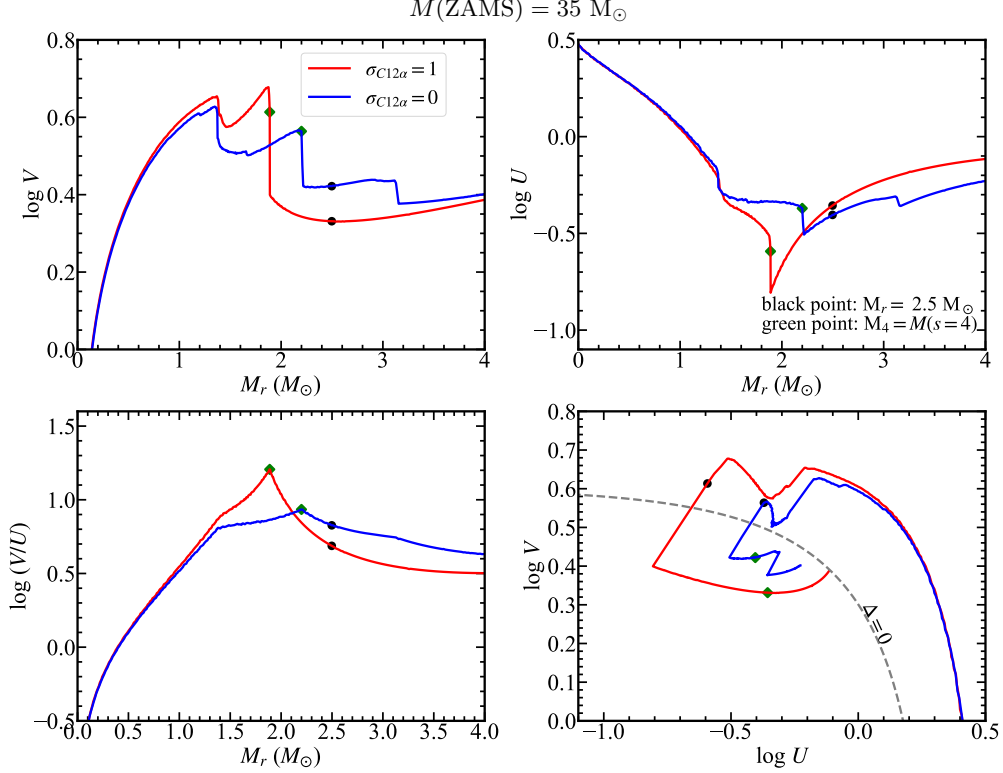


Figure 39. The $U - V$ curves of $35 M_{\odot}$ star at $\tau = t_f$. The orange points represent the place where $M_r = 2.5 M_{\odot}$, while the green diamonds show the place where $M_r = M(s=4)$.

5. DEPENDENCE OF EXPLODABILITY ON $M(\text{ZAMS})$ AND $^{12}\text{C}(\alpha, \gamma)^{16}\text{O}$ RATE

We calculate the evolution of massive stars for various combinations of $M(\text{ZAMS})$ and $\sigma_{C12\alpha}$ and obtain the compactness parameter $\xi_{2.5}$ (Equation 13) at the final stage of evolution ($t = t_f$) when $\log T_c \text{ (K)} = 10.0$ (see Tables A). $\xi_{2.5}$ has been suggested to be useful to evaluate the explodability of massive stars (Ugliano et al. 2012; Sukhbold & Woosley 2014; Müller et al. 2016; Ertl et al. 2016; Sukhbold et al. 2018; Ertl et al. 2020).

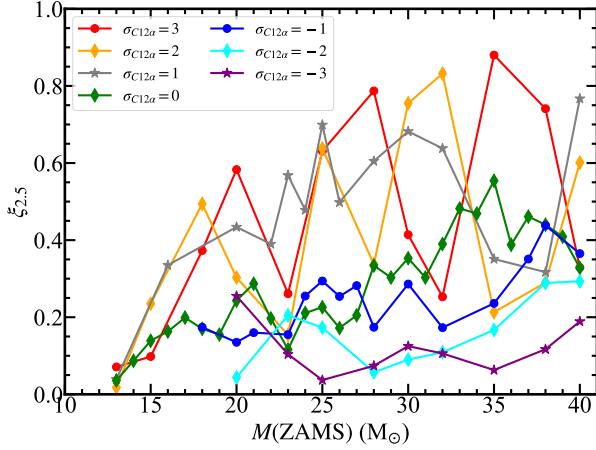


Figure 40. The compactness parameter $\xi_{2.5}$ as a function (ZAMS) for $\sigma_{C12\alpha} = -3, -2, -1, 0, 1, 2$, and 3 .

Figure 40 shows how $\xi_{2.5}$ depends on $\sigma_{C12\alpha}$ from -3 to $+3$ and $M(\text{ZAMS})$ for $13 - 40 M_\odot$. The dependence on the $^{12}\text{C}(\alpha, \gamma)^{16}\text{O}$ rate has also been studied by Sukhbold & Woosley (2014). Our results cover a wider range of the reaction rate, i.e., $\sigma_{C12\alpha} = -3$ to $+3$. Figure 40 shows complicated dependences of $\xi_{2.5}$ on $M(\text{ZAMS})$ and $\sigma_{C12\alpha}$, but the details of the dependencies are shown in the following figures with discussion.

5.1. Compactness Parameter and Shell Burning

As a source of such complicated dependences, the effect of C shell burning on $\xi_{2.5}$ is important (Chieffi & Limongi 2020). We have investigated in sections 4.1.5 and 4.2.2 how the mixing of C and resultant C shell burning cause the difference in $\xi_{2.5}$ between $\sigma_{C12\alpha} = 0$ and -1 as summarized below.

The evolution of $\xi_{2.5}$ for $\sigma_{C12\alpha} = -1$ and 0 (Figure 23) is simply the evolution of $1/r_{2.5}$ as shown in Figure 16. During the evolution until $\tau \sim 10^0$ yr, the shell at $M_r = 2.5 M_\odot$ simply contracts, i.e., $r_{2.5}$ decreases, so that $\xi_{2.5}$ increases for both $\sigma_{C12\alpha}$.

Around $\tau \sim 10^0$ yr, the contraction of the shell stops for $\sigma_{C12\alpha} = -1$ because $X(\text{C})$ at $M_r = 2.0 M_\odot$ is enhanced

(Figure 8 (f)) by convective mixing and C shell burning heats up to cause slight expansion of the overlying layers (see Figure 14 for enhancement of $s_{2.0}$ and $s_{2.5}$). Thus $1/r_{2.5}$ and $\xi_{2.5}$ slightly decrease.

For $\sigma_{C12\alpha} = 0$, such enhancement of $X(\text{C})$ and s does not occur and C is depleted in the convective shell (Figure 8 (e)) to cease C shell burning. Thus $1/r_{2.5}$ and $\xi_{2.5}$ continue to increase (Figs. 16 and 23). The temporal decreases in $1/r_{2.5}$ and $\xi_{2.5}$ around $\tau \sim 10^{-3}$ yr are caused by the activation of O shell burning.

Such a difference in the evolution of $\xi_{2.5}$ and $X(\text{C})$ are also found for $M(\text{ZAMS}) = 25 M_\odot$ and $\sigma_{C12\alpha} = -2$ to 0 as seen in Figure 24.

5.2. Compactness Parameter and $M(\text{ZAMS})$

The effect of C shell burning on $\xi_{2.5}$ appears not only in the $\sigma_{C12\alpha}$ dependence as described in subsection 5.1 above, but also on the $M(\text{ZAMS})$ dependence. As seen in Figure 40, $\xi_{2.5}$ changes non-monotonically with the $M(\text{ZAMS})$ as has been investigated in several works (e.g., Sukhbold & Woosley 2014; Sukhbold et al. 2018; Chieffi & Limongi 2020).

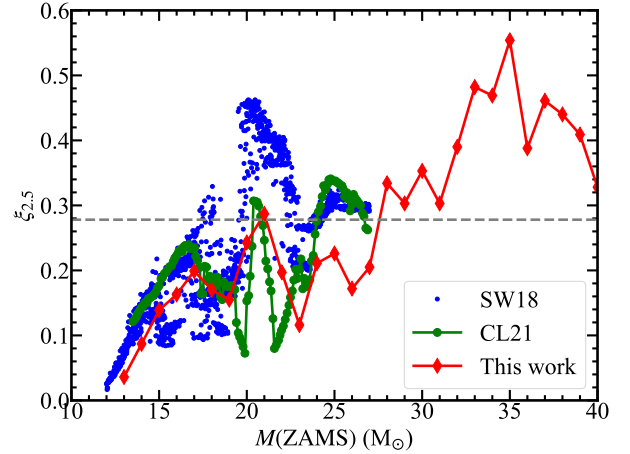


Figure 41. The compactness parameter as a function of $M(\text{ZAMS})$ from different works. Green points show the results from Chieffi et al. (2021) and blue points represent the results from Sukhbold et al. (2018), respectively. The results of this work are marked by red diamonds. The grey dashed line represents the critical value of $\xi_{2.5} = 0.278$ from Müller et al. (2016).

Figure 41 compares our $\xi_{2.5}$ as a function of $M(\text{ZAMS})$ for $\sigma_{C12\alpha} = 0$ (red) with those from Sukhbold et al. (2018) (blue) and Chieffi et al. (2021) (green). Dependencies on $M(\text{ZAMS})$ are basically similar.

$\xi_{2.5}$ generally increases with $M(\text{ZAMS})$ as seen in Figure 41. For larger $M(\text{ZAMS})$, the mass fraction $q = M_r/M(\text{ZAMS})$ of the shell of $M_r = 2.5 M_\odot$ is smaller.

For nearly homologous models, the density structure as a function of q is similar at the same stage. The shell of smaller q is deeper and $r_{2.5}$ is smaller. Thus $\xi_{2.5}$ tends to be larger for larger $M(\text{ZAMS})$.

However, the dependence of $\xi_{2.5}$ on $M(\text{ZAMS})$ is not monotonic. For example, the green (Chieffi et al. 2021) points in Figure 41 show the decrease of $\xi_{2.5}$ with $M(\text{ZAMS})$ for several mass ranges. Chieffi et al. (2021) discussed such a change as follows. At the mass ranges of $M(\text{ZAMS}) = 17.4 - 19.4$ and $20.3 - 21 M_\odot$, the heating effect of convective C shell burning is strong enough to decrease $\xi_{2.5}$. Thus, the three peaks are formed at $M(\text{ZAMS}) = 19.4, 21.0$, and $25 M_\odot$. Our results shown by the red-line in Figure 41 are basically similar, although the peak value of $\xi_{2.5}$ around $M(\text{ZAMS}) = 25 M_\odot$ is smaller.

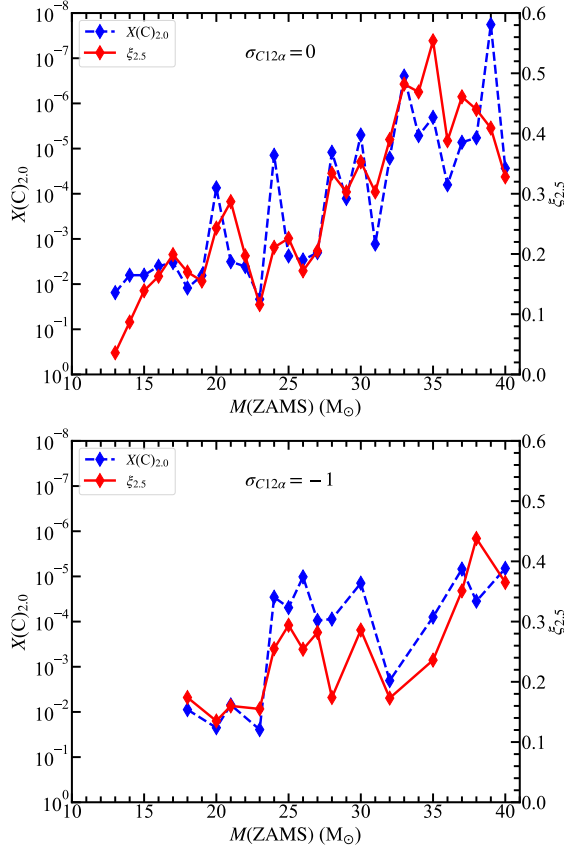


Figure 42. $X(\text{C})_{2.0}$ compared with $\xi_{2.5}$ and as a function of $M(\text{ZAMS})$ for $\sigma_{C12\alpha} = 0$ and -1 . Here $X(\text{C})_{2.0}$ denotes $X(^{12}\text{C})$ and $X(^{16}\text{O})$ at $M_r = 2.0 M_\odot$.

For the peak of $\xi_{2.5}$ around $M(\text{ZAMS}) = 21 M_\odot$ in Figure 41, Chieffi & Limongi (2020) discussed the relation with the critical mass M_{crit} . As mentioned in § 3.3, for stars with increasing $M(\text{ZAMS})$, core C burning changes from convective to radiative around M_{crit} because of the

decreasing C/O ratio. This transition may cause a sharp change in $\xi_{2.5}$ with $M(\text{ZAMS})$ as discussed by Chieffi & Limongi (2020) for $\sigma_{C12\alpha} = 0$ (Figure 41).

The critical mass M_{crit} is larger for smaller $\sigma_{C12\alpha}$ (Table 5), so that the peak of $\xi_{2.5}$ appears at larger $M(\text{ZAMS})$ as compared in Figure 42.

To examine whether such C mixing affects the compactness parameter for other stars, we compare $X(\text{C})_{2.0}$ and $\xi_{2.5}$ as a function of $M(\text{ZAMS})$ in Figure 42 for $\sigma_{C12\alpha} = 0$ and -1 . Here $X(\text{C})_{2.0}$ denotes $X(^{12}\text{C})$ at $M_r = 2.0 M_\odot$. (Note, in the vertical axis of Figure 42, $X(\text{C})_{2.0}$ decreases upward, while $\xi_{2.5}$ increases upward.)

We find a good correlation between $\xi_{2.5}$ and $X(\text{C})_{2.0}$, thus concluding that the non-monotonicity of $\xi_{2.5}$ is mainly determined by the behavior of the C burning shell, which is related to $X(^{12}\text{C})$ near the bottom of the C burning shell (around $M_r \sim 2.0 M_\odot$). For higher $M(\text{ZAMS})$, the effect of O shell burning is significant.

5.3. Explodability

5.3.1. Criteria for Explodability

The compactness parameter has been suggested to be a criterion of the explodability of presupernova models (Ugliano et al. 2012; Müller et al. 2016). Based on the 1D hydrodynamical simulations of neutrino-driven supernova models, a two-parameter criterion in the $M_4\mu_4 - \mu_4$ plane for the explodability has been proposed by Ertl et al. (2016) and Ertl et al. (2020). Here μ_4 is defined in Equation 14.

We plot all of our 99 models with the combination of $M(\text{ZAMS})$ and $\sigma_{C12\alpha}$ in the $M_4\mu_4 - \mu_4$ plane of Figure 43, where M_4 and μ_4 are given in Table 7. We adopt the line of $\mu_4 = 0.194\mu_4 M_4 + 0.058$ ³ from Ertl et al. (2016) and draw in this plane. According to the hydrodynamical simulations by Ertl et al. (2016), models above this line are likely to form BHs without much mass ejection and models below this line are likely to explode to form NSs.

Note the presupernova models adopted by Ertl et al. (2016) are different from ours and we need hydrodynamical simulations of core-collapse for our own models. Nevertheless, we assume that the line of $\mu_4 = 0.194\mu_4 M_4 + 0.058$ divides the BH formation and the NS formation for our presupernova models with different $\sigma_{C12\alpha}$. For simplicity in the present paper, we call

³ We do not use the separation line of $\mu_4 = 0.33\mu_4 M_4 + 0.09$ proposed by Müller et al. (2016), because among our 99 models there is only one “collapse” model, which seems too small.

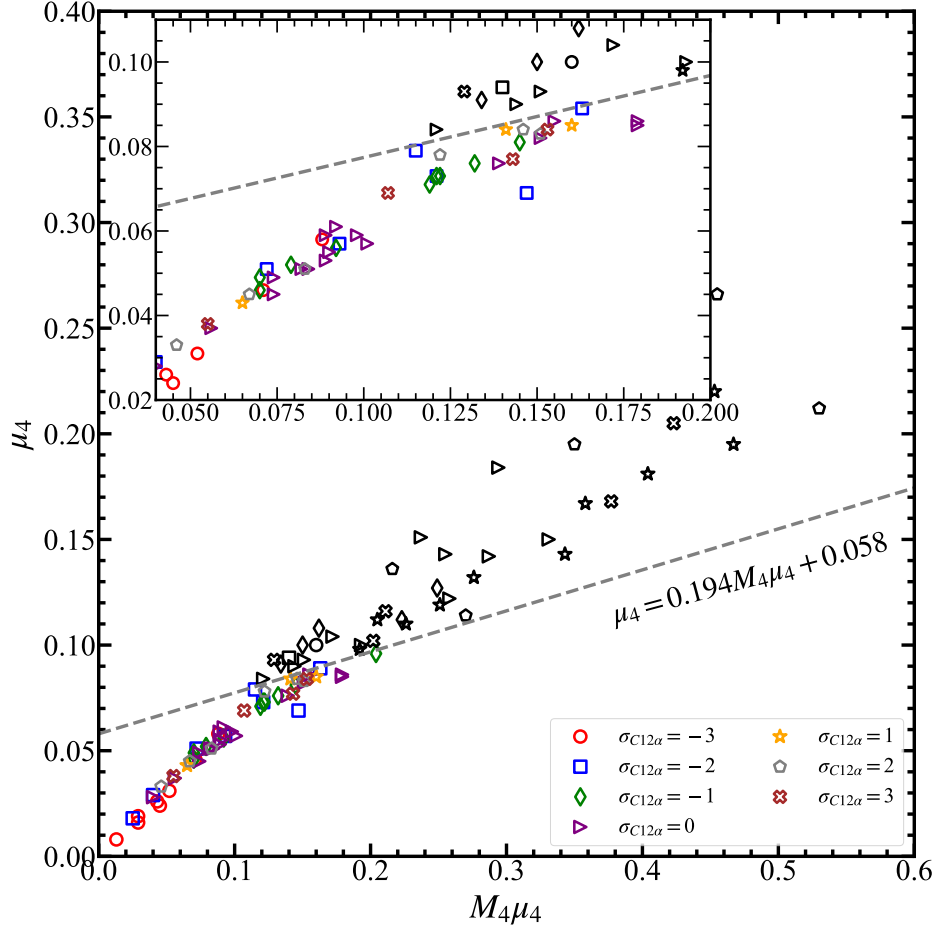


Figure 43. Distribution of the presupernova models in the $M_4\mu_4 - \mu_4$ plane. The explosion and collapse models are distinguished with $\mu_4 = 0.194M_4\mu_4 + 0.058$ from Ertl et al. (2016). The collapse models are in black, and the explosion models are in other colors.

the models above this line “collapse” models and indicate them with black markers. We call the models below this line as “explosion” models and indicate them with color markers. Different shapes and colors are used for different $\sigma_{C12\alpha}$ s.

In Tables 7 and 8, we indicate “explosion” or “collapse” for each model. To show clearly how the separation between “explosion” or “collapse” depend on model parameters ($\sigma_{C12\alpha}$ and $M(\text{ZAMS})$) and model properties ($\xi_{2.5}$, μ_4 , V/U_{\max} ⁴, and U_{\min}), we plot in Figures 44 and 45 these model properties as a function of $M(\text{ZAMS})$ for $\sigma_{C12\alpha} = -3$ to $+3$.

In these figures, V/U_{\max} of the left Y-axis decreases upward. On the right Y-axis, the scale of the positive value part for $\xi_{2.5}$ and μ_4 is different from the negative value part for $\log U_{\min}$. The filled diamonds indicate “ex-

plosion” models, while open circles indicate “collapse” models. These explosion and collapse models are predicted by the results of Figure 43.

We find that “explosion” and “collapse” can be separated by the critical values of $\mu_4 = 0.088 \pm 0$, $\xi_{2.5} = 0.293^{+0.059}_{-0.040}$, $\log V/U_{\max} = 1.205^{+0.070}_{-0.055}$, and $\log U_{\min} = -0.745^{+0.053}_{-0.032}$. In Figures 44 and 45, these critical values are shown by the dashed lines with the uncertainty bars.

For models outside the uncertainty bars, the numbers of correct predictions of “explosion” and “collapse”, and false predictions (“false”) for μ_4 , $\xi_{2.5}$, V/U_{\max} , and U_{\min} are given in Table 6 for $\sigma_{C12\alpha}$ from -3 to $+3$. The uncertainty bars are chosen to make the fraction of “false” prediction less than 5 %. (Remember that the total number of models is 99). Inside the uncertainty bars, the final fate of the model is regarded as “uncertain”, where the numbers of correct and false predictions are also given in Table 6. These uncertainties may be re-

⁴ V/U_{\max} denotes $(V/U)_{\max}$.

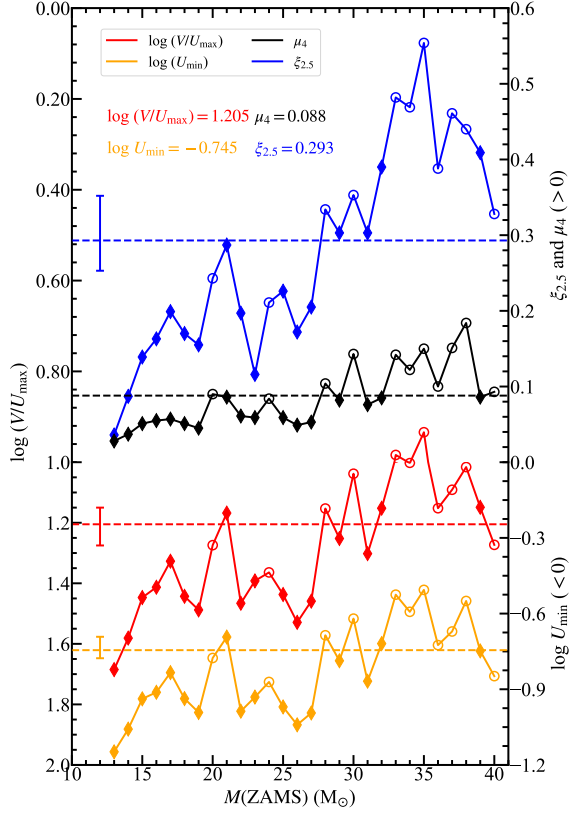


Figure 44. The $\log(V/U_{\max})$, $\log U_{\min}$, $\xi_{2.5}$ and μ_4 as a function of $M(\text{ZAMS})$ for $\sigma_{C12\alpha} = 0$. The left Y-axis is shown upside down. On the right Y-axis, $\xi_{2.5}$ and μ_4 are shown with the upper part (positive) while $\log U_{\min}$ is shown in the bottom part (negative). The filled diamonds represent explosion models, while open circles represent collapse models. The explosion and collapse are predicted by the results of Figure 43. The critical value of each parameter is shown as dashed lines and an uncertainty of $\pm 6\%$. We assume that the models beyond $\pm 6\%$ of critical value should collapse and explode, while those within this range are uncertain because of the uncertainties of progenitor evolution and explosion mechanism.

lated to the uncertainties of presupernova models and hydrodynamical simulations. To make the uncertainties smaller, we need core-collapse calculations using our own presupernova models calculated in this paper, which will be done in the forthcoming study.

We note from Figures 44 and 45 and Table 6 several properties of presupernova structures.

$\xi_{2.5}$, μ_4 , V/U_{\max} , and $1/U_{\min}$ show similar dependencies on $M(\text{ZAMS})$. As discussed in Section 4.2.4, V/U_{\max} and $1/U_{\min}$ are the steepest gradients of $\log P$ and $\log r$ with respect to M_r in the CO core. μ_4 is also the average gradient. Thus, the compactness parameter $\xi_{2.5}$ is closely related to the gradients of pressure and density

Table 6. The number of “explosion”, “collapse” and “uncertain” models for different criteria.

prediction	“explosion”	“collapse”	“false”	“uncertain”	
				correct	false
μ_4	54	42	3	0	0
$\xi_{2.5}$	41	31	5	11	11
V/U_{\max}	45	31	5	11	7
U_{\min}	50	32	5	7	5

in the presupernova core. This is the reason why larger μ_4 and $\xi_{2.5}$, smaller V/U_{\max} and $1/U_{\min}$ tend to collapse. As shown in Figure 22, the core-collapse models would more easily explode with the steeper gradients of pressure and density.

During the core-collapse and bounce, the mass accretion onto the collapse object produces lamb pressure against the bouncing shock and the accretion rate would be lower if the density structure is steeper. This would make the explosion easier to occur. Also, the shock wave generated at the bounce and propagates outward would be more strengthened at the steeper gradient, which would also make the explosion easier.

Although $\xi_{2.5}$ would be a good measure of “collapse” vs. “explosion”, we propose that V/U_{\max} and $1/U_{\min}$ are physically reasonable measures of the explodability.

5.3.2. Explodability and $^{12}\text{C}(\alpha, \gamma)^{16}\text{O}$ Rate

Figures 44 and 45 and Table 6 show the dependence of the explodability on $\sigma_{C12\alpha}$. For smaller $\sigma_{C12\alpha}$, generally, V/U_{\max} and $1/U_{\min}$ tend to be larger, while $\xi_{2.5}$ and μ_4 tend to smaller. Thus, a larger number of models tend to undergo explosions for smaller $\sigma_{C12\alpha}$,

The dependence of “collapse vs. explosion” on $M(\text{ZAMS})$ also depends on $\sigma_{C12\alpha}$ as seen in these figures. For $\sigma_{C12\alpha} > 0$, e.g., the $M(\text{ZAMS})$ dependence is different because the effect of O shell burning is dominant over C shell burning. How $\sigma_{C12\alpha}$ affects the presupernova structures and V/U_{\max} will be shown for $M(\text{ZAMS})$ in the next section.

5.4. Presupernova Structure and $^{12}\text{C}(\alpha, \gamma)^{16}\text{O}$ Rate

5.4.1. Oxygen Shell Burning, V/U_{\max} , and U_{\min}

Figures 46 show how $\sigma_{C12\alpha}$ affects the presupernova structures of the density and entropy and the locations of V/U_{\max} for $M(\text{ZAMS}) = 18 - 40 M_{\odot}$ with $\sigma_{C12\alpha} = 0$ (solid lines) and -1 (dashed lines). It is indicated whether these models are “collapse” or “explosion” (or

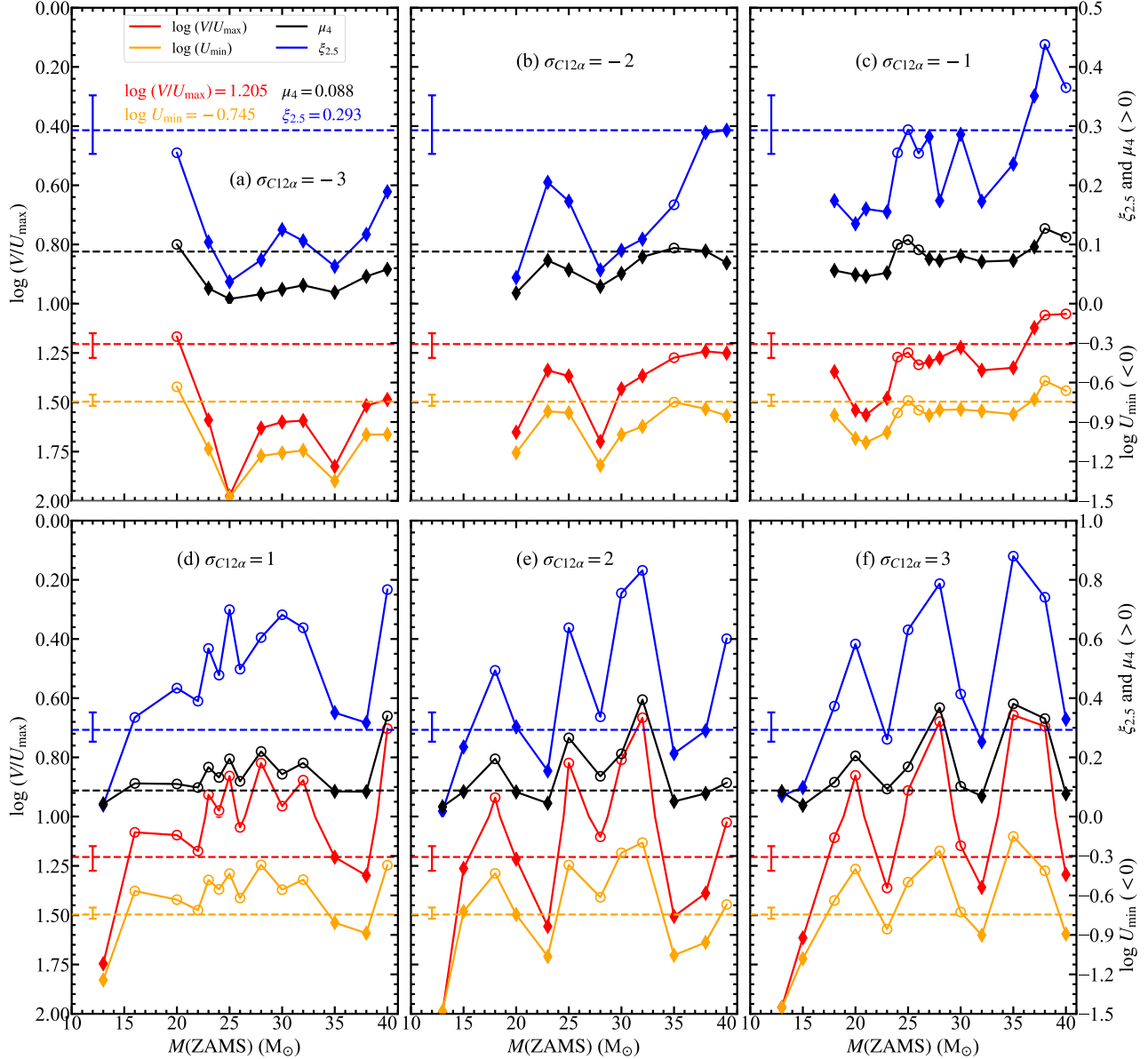


Figure 45. The $\log(V/U_{\max})$, $\log U_{\min}$, $\xi_{2.5}$ and μ_4 as a function of $M(\text{ZAMS})$ for $\sigma_{C12\alpha} = \pm 1, \pm 2$ and ± 3 .

“uncertain”). The lines and marks are the same as used in Figure 22 for $M(\text{ZAMS}) = 28 M_{\odot}$.

These figures show that V/U_{\max} is located in most cases at the sharp increase in s , which is produced by O shell burning (i.e., at the outer edge of the Si core $M_r = M(\text{Si})$). When shell burning is active, the released heat prevents the contraction of the outer layers and the density there remains almost constant and even decreases as seen in Figure 17. On the other hand, the inner core continues to increase the density of the inner core. This creates a very steep density gradient, almost a density jump, and a decrease in U , which is the ratio between ρ and the mean density of the inner core.

For example, two density jumps are produced by C shell burning and O shell burning at $M_r = 1.95 M_{\odot}$ and $1.44 M_{\odot}$, respectively, in the $28 M_{\odot}$ star for $\sigma_{C12\alpha} = -1$ (Figure 22). These two density jumps correspond to the sharp jumps of V , two valley points of U , and the highest peak and knee points of V/U in Figure 20.

Thus, the steepest gradient of density is created by the most active shell burning, mostly oxygen burning. This implies $M(V/U_{\max}) \simeq M(\text{Si})$. For $\sigma_{C12\alpha} = -1$, $M(\text{Si})$ tends to be smaller than those for $\sigma_{C12\alpha} = 0$, which would affect the explodability as has been discussed for $M(\text{ZAMS}) = 28 M_{\odot}$.

5.4.2. Core Masses and $\sigma_{C12\alpha}$

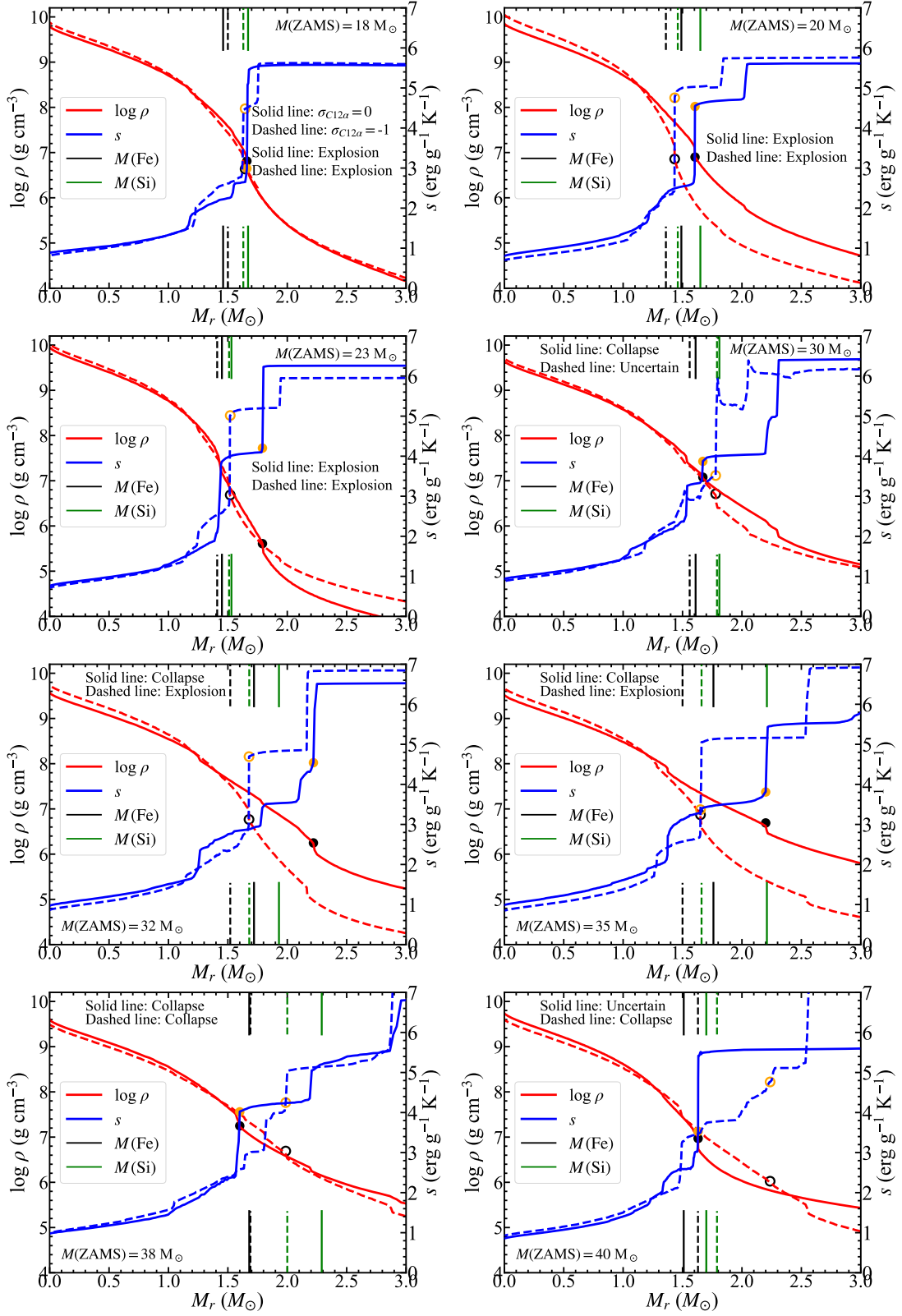


Figure 46. The presupernova density and entropy distributions of stars of several $M(\text{ZAMS})$ for $\sigma_{C12\alpha} = 0$ (solid line) and -1 (dashed line). It is indicated whether these models are “collapse” or “explosion” (or “uncertain”). The lines and marks are the same as used in Figure 22 for $M(\text{ZAMS}) = 28 M_\odot$.

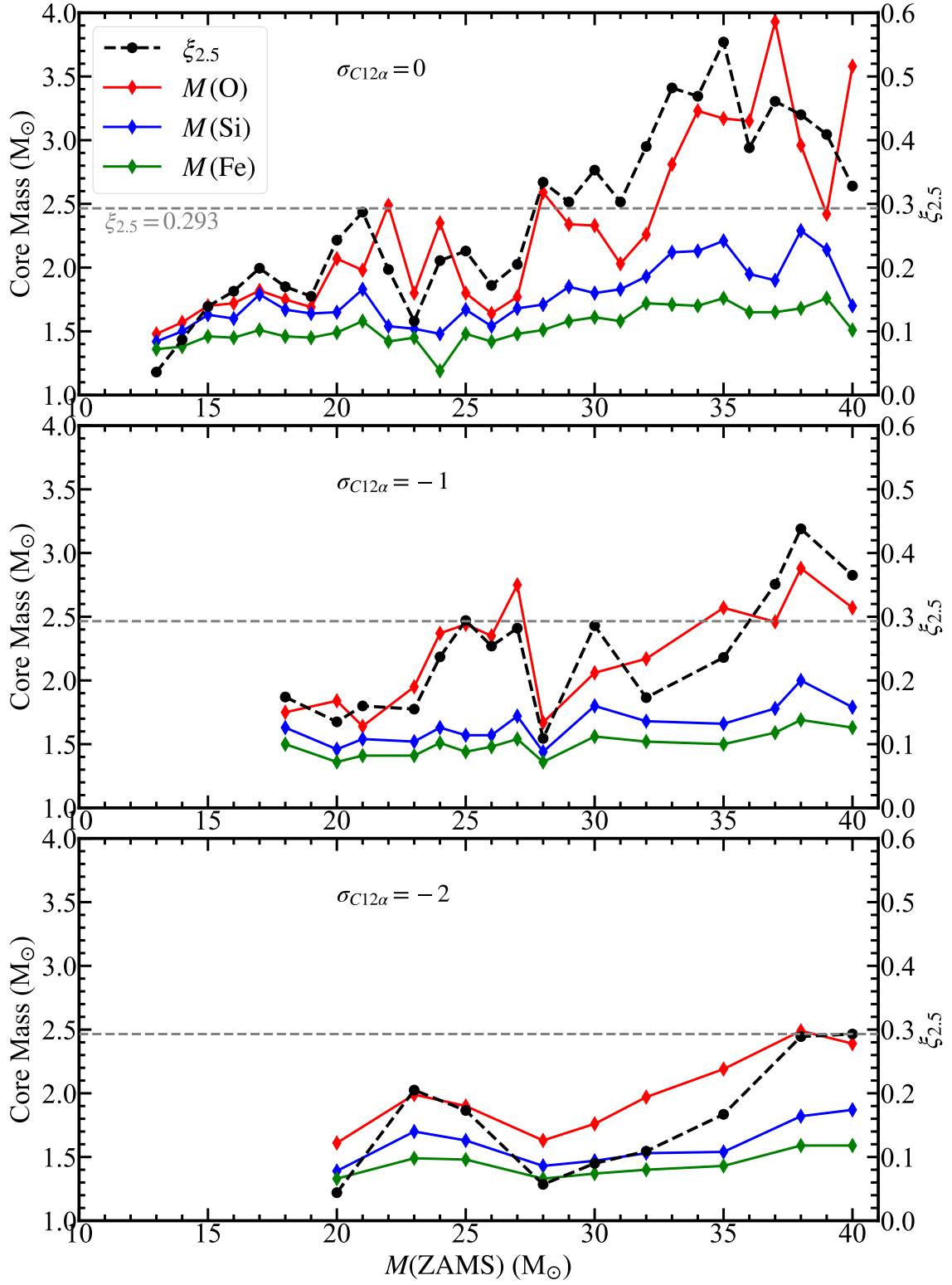


Figure 47. The core masses, $M(\text{O})$, $M(\text{Si})$, $M(\text{Fe})$ and $\xi_{2.5}$ as a function of $M(\text{ZAMS})$ for $\sigma_{C12\alpha} = 0$ (top), -1 (median) and -2 (bottom). The gray dashed line shows the critical value of $\xi_{2.5} = 0.293$.

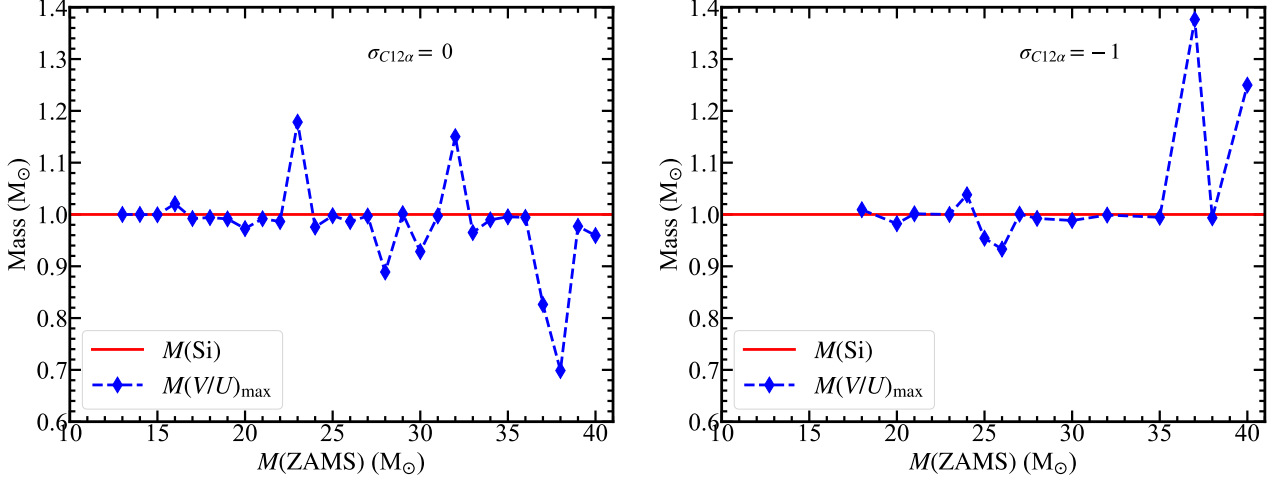


Figure 48. $M(V/U_{\max})$ normalized by $M(\text{Si})$ as a function of $M(\text{ZAMS})$ for $\sigma_{C12\alpha} = 0$ and -1 .

Given the importance of these core masses for the explosability, Figure 47 shows the masses of Fe core $M(\text{Fe})$, Si core $M(\text{Si})$, and O core $M(\text{O})$, as well as $\xi_{2.5}$ as a function of $M(\text{ZAMS})$ at the final stages ($\tau = t_f$) for $\sigma_{C12\alpha} = 0, -1$ and -2 . The data for all models are also listed in Table 7 and 8. As mentioned earlier, the boundaries of $M(\text{Fe})$, $M(\text{Si})$, and $M(\text{O})$ are defined at the location where the energy generation rates of the Si-burning shell, O-burning shell, and C-burning shell are the highest.

In these figures, $M(\text{O})$ and $\xi_{2.5}$ change with $M(\text{ZAMS})$ non-monotonously. Their changes are similar, which implies that $\xi_{2.5}$ is mainly affected by C shell burning, as discussed earlier. For smaller $\sigma_{C12\alpha}$, $M(\text{O})$ tends to be smaller because $X(\text{C})$ is larger in the deeper region, as has been shown in Figure 42 for $M(\text{ZAMS}) = 28 M_{\odot}$. Then the smaller $M(\text{O})$ leads to the formation of smaller $M(\text{Si})$ and $M(\text{Fe})$.

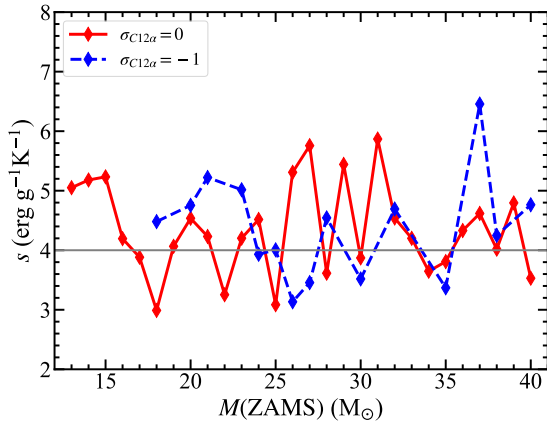


Figure 49. The entropy at $M(V/U_{\max})$ as a function of $M(\text{ZAMS})$ for $\sigma_{C12\alpha} = 0$ and -1 . The grey line shows where $s = 4 \text{ erg g}^{-1} \text{ K}^{-1}$.

Figure 48 shows $M(V/U_{\max})$ normalized by $M(\text{Si})$, which shows that $M(V/U_{\max})$ is almost identical to $M(\text{Si})$ except for a few $M(\text{ZAMS})$. This is because O-shell burning is the strongest shell burning at the onset of collapse and forms a very steep increase in entropy (Figure 22) and thus the steepest gradients of pressure and density as discussed above for Figure 46.

Figure 49 shows the entropy at (V/U_{\max}) , which ranges from $s(\text{erg g}^{-1} \text{ K}^{-1}) = 3$ to 6 including 4. Thus $M_4 = M(V/U_{\max})$ except for a few $M(\text{ZAMS})$ (see Table 7). This is also due to the entropy jump at the O burning shell.

As discussed in Section 4.2.4, $M(V/U_{\max}) = M_{\text{eff}}$. Therefore, smaller $M(V/U_{\max})$ for smaller $\sigma_{C12\alpha}$ leads to smaller s_c and thus higher ρ_c for the same T_c (Equation 9 and 11).

5.4.3. Density Profiles and $\sigma_{C12\alpha}$

Figures 50 show the density profiles at the final pre-collapse models (i.e., at $\log T_c(\text{K}) = 10.0$) for $\sigma_{C12\alpha} = 0, -1$ and 1 . On top figures, models for “explosion” (left) and “collapse” (right) are shown for $\sigma_{C12\alpha} = 0$. At the bottom, models for “explosion” (left) and “collapse” (right) are shown for $\sigma_{C12\alpha} = -1$ (solid lines) and 1 (dashed lines). The points on the lines show the location of V/U_{\max} .

By comparing the models with the same $M(\text{ZAMS})$, $M(V/U_{\max}) (= M_{\text{eff}})$ is smaller and thus ρ_c is lower for smaller $\sigma_{C12\alpha}$. This means that the density distribution concerning M_r tends to be steeper for smaller $\sigma_{C12\alpha}$. Also, the “explosion” models (left) tend to have a steeper density structure than the “collapse” models (right). This suggests that models with smaller $\sigma_{C12\alpha}$ explode more easily, although the exact explosability depends on the behavior of C shell burning.

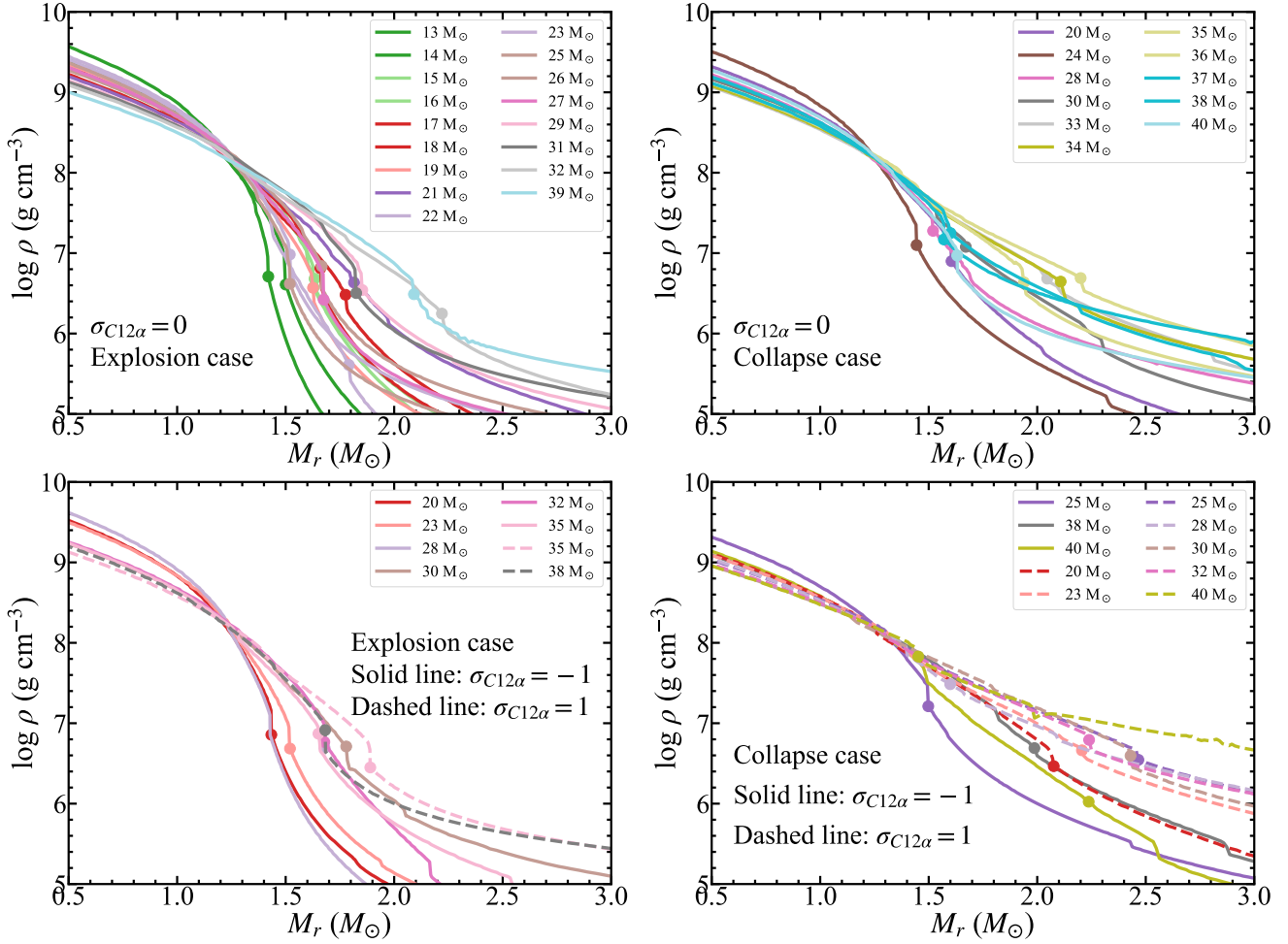


Figure 50. The density profile ranging from $0.7 < M_r < 2.75 M_\odot$ for different $M(\text{ZAMS})$ and $\sigma_{C12\alpha}$. (Top) The explosion (left) and collapse (right) models for $\sigma_{C12\alpha} = 0$ are shown. (Bottom) The explosion (left) and collapse (right) models for $\sigma_{C12\alpha} = -1$ and 1 are shown by the solid lines and dashed lines, respectively. The points on the lines show the location of $M(V/U_{\max})$ and its local density.

To judge whether the modes are “explosion” or “collapse”, Burrows & Vartanyan (2021), Wang et al. (2022), Boccioli et al. (2023) and Boccioli et al. (2025) have suggested that the models with stronger density jumps at the Si/O interface are more likely to explode and the location of this density jump may be the initial boundary of the proto-NS based on their 2D and 3D simulations of the core collapse. This is consistent with our findings of the importance of V/U_{\max} , but our results can provide the *quantitative* criterion, i.e., the critical steepness of the density for the “explosion vs. collapse”.

6. SUMMARY AND DISCUSSION

Among the uncertainties of stellar evolution theory, we investigate how the $^{12}\text{C}(\alpha, \gamma)^{16}\text{O}$ reaction rate affects the evolution of massive stars through the beginning of the Fe core collapse. We adopt stars with the initial masses of $M(\text{ZAMS}) = 13 - 40 M_\odot$ and the solar metallicity. For the reaction rate, we adopt $\sigma_{C12\alpha} =$

$-3, -2, -1, 0, 1, 2$, and 3 , i.e., by a factor of $0.37, 0.52, 0.78, 1, 1.28, 1.93$, and 2.69 of the standard rate.

Comparison between $\sigma_{C12\alpha} = -1$ and 0 is made particularly in detail for the evolution of the $M(\text{ZAMS}) = 28 M_\odot$ stars. For $M(\text{ZAMS}) = 25 M_\odot$, models with $\sigma_{C12\alpha} = -2, -1$, and 0 are compared, and for the $M(\text{ZAMS}) = 35 M_\odot$ models, $\sigma_{C12\alpha} = 0$ and $+1$ are examined. For the explodability, models with the whole range of $M(\text{ZAMS})$ and $\sigma_{C12\alpha}$ are calculated.

We find the following differences:

- (1) Smaller $\sigma_{C12\alpha}$ leads to the synthesis of a larger mass fraction of C, $X(\text{C})$, which makes C shell burning stronger. Then, the convection zone extends to mix C from the overlying layer, further strengthening C shell burning. The extra heating by C shell burning tends to prevent the contraction of outer layers and decrease the compactness parameter at $M_r = 2.5 M_\odot$.

- (2) This effect leads to the formation of smaller mass cores of Si and Fe and the steeper density and pressure gradients at the O burning shell in the presupernova models.
- (3) This difference affects the *explodability* of the models, i.e., whether a NS or a BH is formed, The steeper pressure gradient results in more likely the explosion forming a NS rather than a BH.
- (4) We describe the pressure gradient against M_r with V/U and the density drop with $1/U$, where U and V are non-dimensional variables to describe the stellar structure (Equation. 2 and 3).
- (5) By applying the Ertl-criterion for explodability, we estimate the critical values of V/U and $1/U$ at the O-burning shell above which the model is more likely to explode.
- (6) We conclude that the smaller $^{12}\text{C}(\alpha, \gamma)^{16}\text{O}$ reaction rate makes the mass range of $M(\text{ZAMS})$ that forms a NS larger.
- (7) The dependencies of the compactness parameter on $M(\text{ZAMS})$ and the reaction rate is consistent with the earlier results by Sukhbold & Woosley (2014) and Chieffi & Limongi (2020) but our study covers a much wider range of input parameters.
- (8) In view of the importance of the overshooting of C shell burning to enhance $X(\text{C})$ by mixing fresh C, multi-

D simulations of convective overshooting (Cristini et al. 2019; Rizzuti et al. 2022) are critically important.

In the forthcoming papers, we will present the explodability by hydrodynamical calculations of collapse for our progenitor models with different $\sigma_{C12\alpha}$ rather than using the Ertl-criterion. We will also present how the detailed nucleosynthesis yields depend on $\sigma_{C12\alpha}$.

7. ACKNOWLEDGEMENTS

This work was supported by the National Natural Science Foundation of China under Grant Nos. 11988101 and the National Key R&D Program of China No. 2024YFA1611900. W. Y. X. is supported by the Cultivation Project for LAMOST Scientific Payoff and Research Achievement. W. Y. X. thanks Xianfei Zhang and Shaolan Bi for their financial support (the grants 12073006, 12090040 and 12090042 from the National Natural Science Foundation of China) and also their help in using MESA. K. N. is supported by the World Premier International Research Center Initiative (WPI), MEXT, Japan, and the Japan Society for the Promotion of Science JSPS KAKENHI Grant Numbers JP20K04024, JP21H044pp, and JP23K03452. We would like to thank Marco Limongi and Raphael Hirschi for useful discussion.

APPENDIX

A. PROPERTY OF EXPLOSION

Table 7. Presupernova properties for varying $\sigma_{C12\alpha}$ and $M(\text{ZAMS})$ at the final stage ($T_c = 10^{10}$ K).

$\sigma_{C12\alpha}$	$M(\text{ZAMS})$ (M_\odot)	$\log(V/U_{\max})$	$\log V_{\max}$	$\log U_{\min}$	$M(V/U_{\max})$ (M_\odot)	M_4 (M_\odot)	μ_4	$M_4\mu_4$	$\xi_{2.5}$	fate
-3 σ	20	1.167	0.696	-0.632	1.531	1.597	0.100	0.160	0.255	uncertain
	23	1.590	0.723	-1.104	1.680	1.677	0.026	0.043	0.104	explosion
	25	1.975	0.803	-1.471	1.545	1.544	0.008	0.013	0.037	explosion
	28	1.631	0.779	-1.158	1.793	1.762	0.016	0.029	0.074	explosion
	30	1.600	0.745	-1.135	1.877	1.868	0.024	0.045	0.125	explosion
	32	1.593	0.764	-1.116	1.863	1.687	0.031	0.052	0.106	explosion
	35	1.825	0.809	-1.348	1.654	1.504	0.019	0.029	0.063	explosion
	38	1.517	0.795	-0.996	1.523	1.529	0.046	0.071	0.117	explosion
	40	1.486	0.799	-0.995	1.512	1.511	0.058	0.088	0.189	explosion
-2 σ	20	1.652	0.756	-1.134	1.395	1.394	0.018	0.025	0.044	explosion
	23	1.338	0.754	-0.819	1.667	1.662	0.073	0.121	0.205	explosion

Table 7 – continued

$\sigma_{C12\alpha}$	$M(\text{ZAMS})$ (M_{\odot})	$\log(V/U_{\max})$	$\log V_{\max}$	$\log U_{\min}$	$M(V/U_{\max})$ (M_{\odot})	M_4 (M_{\odot})	μ_4	$M_4\mu_4$	$\xi_{2.5}$	fate
-2σ	25	1.367	0.707	-0.830	1.631	1.631	0.057	0.093	0.173	explosion
	28	1.699	0.821	-1.230	1.633	1.386	0.029	0.040	0.057	explosion
	30	1.432	0.763	-0.996	1.429	1.429	0.051	0.072	0.090	explosion
	32	1.366	0.749	-0.934	1.956	1.463	0.079	0.115	0.109	explosion
	35	1.274	0.754	-0.749	1.354	1.489	0.094	0.140	0.167	explosion
	38	1.242	0.705	-0.800	1.830	1.826	0.089	0.163	0.289	uncertain
	40	1.251	0.683	-0.852	2.377	2.112	0.069	0.147	0.293	uncertain
-1σ	18	1.345	0.715	-0.848	1.645	1.631	0.056	0.092	0.174	explosion
	20	1.540	0.795	-1.025	1.434	1.434	0.049	0.070	0.135	explosion
	21	1.564	0.807	-1.056	1.542	1.541	0.046	0.070	0.160	explosion
	23	1.480	0.735	-0.979	1.520	1.515	0.052	0.079	0.155	explosion
	24	1.244	0.713	-0.770	1.692	1.692	0.073	0.124	0.237	uncertain
	25	1.248	0.741	-0.736	1.498	1.498	0.108	0.162	0.294	uncertain
	26	1.310	0.740	-0.809	1.465	1.471	0.091	0.134	0.254	uncertain
	27	1.294	0.693	-0.848	1.721	1.721	0.076	0.132	0.282	uncertain
	28	1.566	0.769	-1.035	1.429	1.428	0.044	0.063	0.109	explosion
	30	1.222	0.657	-0.804	1.779	1.779	0.081	0.145	0.286	uncertain
	32	1.338	0.724	-0.817	1.678	1.678	0.071	0.119	0.173	explosion
	35	1.325	0.729	-0.841	1.651	1.657	0.073	0.121	0.236	explosion
	37	1.122	0.688	-0.728	2.450	2.119	0.096	0.204	0.351	uncertain
	38	1.058	0.634	-0.586	1.987	1.958	0.127	0.249	0.438	collapse
	40	1.052	0.684	-0.662	2.237	1.988	0.112	0.223	0.365	collapse
0σ	13	1.685	0.814	-1.148	1.420	1.417	0.028	0.040	0.036	explosion
	14	1.581	0.820	-1.058	1.500	1.497	0.037	0.056	0.087	explosion
	15	1.447	0.751	-0.938	1.629	1.625	0.051	0.082	0.139	explosion
	16	1.413	0.748	-0.912	1.633	1.627	0.055	0.090	0.163	explosion
	17	1.327	0.672	-0.834	1.776	1.776	0.057	0.101	0.199	explosion
	18	1.443	0.779	-0.937	1.660	1.660	0.051	0.084	0.170	explosion
	19	1.488	0.749	-0.992	1.626	1.626	0.045	0.074	0.155	explosion
	20	1.274	0.708	-0.776	1.605	1.605	0.090	0.144	0.243	explosion
	21	1.168	0.644	-0.693	1.815	1.802	0.086	0.155	0.287	uncertain
	22	1.466	0.773	-0.987	1.519	1.519	0.061	0.092	0.197	explosion
	23	1.392	0.777	-0.931	1.791	1.514	0.059	0.089	0.116	explosion
	24	1.364	0.722	-0.871	1.444	1.444	0.084	0.121	0.211	explosion
	25	1.437	0.742	-0.970	1.666	1.666	0.059	0.098	0.226	explosion
	26	1.529	0.798	-1.041	1.519	1.519	0.049	0.074	0.172	explosion
	27	1.459	0.755	-0.994	1.675	1.673	0.053	0.089	0.205	explosion
	28	1.153	0.715	-0.686	1.520	1.656	0.104	0.172	0.334	uncertain
	29	1.252	0.711	-0.787	1.853	1.848	0.082	0.151	0.303	uncertain
	30	1.038	0.655	-0.620	1.671	1.786	0.143	0.255	0.353	collapse
	31	1.302	0.717	-0.868	1.825	1.819	0.076	0.139	0.303	uncertain
	32	1.152	0.637	-0.719	2.220	2.114	0.085	0.179	0.390	collapse
	33	0.984	0.610	-0.525	2.046	2.024	0.142	0.287	0.482	collapse
	34	1.002	0.618	-0.593	2.108	2.108	0.122	0.258	0.469	collapse
	35	0.934	0.628	-0.506	2.200	2.200	0.150	0.331	0.554	collapse
	36	1.152	0.686	-0.725	1.939	1.936	0.100	0.193	0.388	collapse

Table 7 – continued

$\sigma_{C12\alpha}$	$M(\text{ZAMS})$ (M_{\odot})	$\log(V/U_{\max})$	$\log V_{\max}$	$\log U_{\min}$	$M(V/U_{\max})$ (M_{\odot})	M_4 (M_{\odot})	μ_4	$M_4\mu_4$	$\xi_{2.5}$	fate
0σ	37	1.091	0.660	-0.671	1.570	1.570	0.151	0.237	0.461	collapse
	38	1.016	0.664	-0.550	1.600	1.600	0.184	0.294	0.440	collapse
	39	1.149	0.658	-0.748	2.091	2.082	0.086	0.179	0.409	collapse
	40	1.273	0.691	-0.848	1.631	1.631	0.093	0.151	0.328	uncertain
$+1\sigma$	13	1.746	0.775	-1.243	2.363	1.498	0.043	0.065	0.039	explosion
	16	1.080	0.678	-0.566	2.595	1.840	0.112	0.205	0.335	uncertain
	20	1.094	0.625	-0.632	2.076	2.058	0.110	0.226	0.434	collapse
	22	1.175	0.694	-0.712	1.947	1.947	0.098	0.192	0.390	collapse
	23	0.926	0.623	-0.482	2.206	2.146	0.167	0.358	0.568	collapse
	24	0.980	0.636	-0.554	2.075	2.093	0.132	0.276	0.478	collapse
	25	0.863	0.601	-0.434	2.466	2.391	0.195	0.467	0.699	collapse
	26	1.055	0.614	-0.620	2.109	2.109	0.119	0.251	0.498	collapse
	28	0.819	0.631	-0.367	1.599	2.057	0.220	0.453	0.605	collapse
	30	0.965	0.614	-0.556	2.430	2.397	0.143	0.343	0.682	collapse
	32	0.877	0.592	-0.480	2.239	2.239	0.181	0.404	0.638	collapse
	35	1.206	0.678	-0.807	1.890	1.888	0.085	0.160	0.351	uncertain
	38	1.299	0.719	-0.887	1.682	1.682	0.084	0.141	0.317	uncertain
	40	0.703	0.596	-0.370	1.452	1.885	0.340	0.642	0.767	collapse
$+2\sigma$	13	1.993	0.822	-1.480	2.428	1.404	0.033	0.046	0.018	explosion
	15	1.263	0.669	-0.722	2.597	1.738	0.084	0.146	0.235	explosion
	18	0.936	0.674	-0.432	1.405	1.796	0.195	0.350	0.494	collapse
	20	1.216	0.666	-0.745	1.831	1.831	0.083	0.151	0.303	uncertain
	23	1.557	0.813	-1.064	1.482	1.480	0.045	0.067	0.154	explosion
	25	0.819	0.629	-0.368	1.384	1.714	0.266	0.455	0.638	collapse
	28	1.103	0.702	-0.614	1.578	1.587	0.136	0.216	0.337	uncertain
	30	0.808	0.570	-0.276	2.593	2.506	0.212	0.530	0.755	collapse
	32	0.666	0.501	-0.198	2.603	2.172	0.395	0.859	0.832	collapse
	35	1.506	0.794	-1.055	1.630	1.630	0.051	0.083	0.213	explosion
	38	1.389	0.759	-0.957	1.567	1.570	0.078	0.122	0.290	uncertain
	40	1.030	0.645	-0.669	2.358	2.358	0.114	0.270	0.601	collapse
$+3\sigma$	13	1.967	0.730	-1.452	2.414	1.823	0.084	0.153	0.071	explosion
	15	1.615	0.819	-1.081	1.458	1.458	0.038	0.055	0.098	explosion
	18	1.107	0.646	-0.638	1.810	1.810	0.116	0.211	0.373	collapse
	20	0.861	0.621	-0.399	1.674	2.065	0.205	0.423	0.583	collapse
	23	1.362	0.765	-0.856	1.386	1.385	0.093	0.129	0.261	uncertain
	25	0.912	0.583	-0.499	2.260	2.251	0.168	0.377	0.631	collapse
	28	0.679	0.546	-0.261	1.789	1.867	0.368	0.686	0.787	collapse
	30	1.148	0.683	-0.726	1.973	1.973	0.102	0.202	0.414	collapse
	32	1.359	0.770	-0.902	1.487	1.553	0.069	0.107	0.253	explosion
	35	0.657	0.506	-0.151	2.596	2.696	0.381	1.028	0.880	collapse
	38	0.695	0.591	-0.412	1.529	1.888	0.331	0.626	0.741	collapse
	40	1.294	0.728	-0.893	1.859	1.859	0.077	0.143	0.329	uncertain

B. INFORMATION OF CORES

Table 8. The core masses for varying $\sigma_{C12\alpha}$ and $M(\text{ZAMS})$ at the final stage ($T_c = 10^{10}$).

$\sigma_{C12\alpha}$	$M(\text{ZAMS}) (M_\odot)$	$M(\text{Fe}) (M_\odot)$	$M(\text{Si}) (M_\odot)$	$M(\text{O}) (M_\odot)$	$M(\text{CO}) (M_\odot)$	$M(\text{He}) (M_\odot)$
-3σ	20	1.45	1.77	2.19	4.26	6.43
	23	1.69	1.52	1.44	5.19	5.54
	25	1.34	1.38	1.54	4.76	8.50
	28	1.38	1.51	1.79	3.46	6.36
	30	1.49	1.63	1.88	7.97	9.18
	32	1.45	1.58	1.75	8.23	9.55
	35	1.40	1.51	1.66	8.58	9.89
	38	1.41	1.54	1.64	10.06	10.08
	40	1.41	1.50	1.65	11.79	13.00
-2σ	20	1.33	1.39	1.61	2.41	6.57
	23	1.49	1.70	1.99	4.99	7.22
	25	1.48	1.63	1.90	5.88	8.37
	28	1.33	1.43	1.63	5.93	7.71
	30	1.37	1.47	1.76	5.55	8.22
	32	1.40	1.53	1.97	3.69	7.50
	35	1.43	1.54	2.19	7.46	9.51
	38	1.59	1.82	2.49	10.55	10.60
	40	1.59	1.87	2.39	11.33	11.73
-1σ	18	1.50	1.63	1.75	3.73	5.77
	20	1.36	1.46	1.84	4.30	6.42
	21	1.41	1.54	1.64	4.57	6.87
	23	1.41	1.52	1.95	5.33	6.07
	24	1.51	1.63	2.37	5.65	6.51
	25	1.44	1.57	2.44	5.85	7.58
	26	1.48	1.57	2.35	5.86	8.56
	27	1.54	1.72	2.75	6.61	8.21
	28	1.36	1.44	1.67	6.69	7.32
	30	1.56	1.80	2.06	7.78	8.42
	32	1.52	1.68	2.17	7.42	8.71
	35	1.50	1.66	2.57	7.42	11.06
	37	1.59	1.78	2.46	8.36	12.15
	38	1.69	2.00	2.88	10.99	13.07
	40	1.63	1.79	2.57	10.47	13.29
0σ	13	1.36	1.42	1.48	2.30	3.83
	14	1.38	1.50	1.57	2.63	4.22
	15	1.46	1.63	1.70	2.92	4.60
	16	1.45	1.60	1.72	3.19	4.93
	17	1.51	1.79	1.82	3.42	5.40
	18	1.46	1.67	1.75	3.54	5.63
	19	1.45	1.64	1.69	4.41	6.34
	20	1.49	1.65	2.07	4.30	6.52
	21	1.58	1.83	1.98	4.53	6.76
	22	1.42	1.54	2.49	4.86	6.04
	23	1.45	1.52	1.80	4.94	5.66
	24	1.19	1.48	2.35	5.74	7.01

Table 8 – continued

$\sigma_{C12\alpha}$	$M(\text{ZAMS}) (M_{\odot})$	$M(\text{Fe}) (M_{\odot})$	$M(\text{Si}) (M_{\odot})$	$M(\text{O}) (M_{\odot})$	$M(\text{CO}) (M_{\odot})$	$M(\text{He}) (M_{\odot})$
0σ	25	1.48	1.67	1.80	5.71	7.13
	26	1.42	1.54	1.64	5.99	7.53
	27	1.48	1.68	1.77	6.66	8.35
	28	1.51	1.71	2.59	6.74	8.79
	29	1.58	1.85	2.34	7.43	9.04
	30	1.61	1.80	2.33	7.97	9.92
	31	1.58	1.83	2.03	8.26	9.77
	32	1.72	1.93	2.26	9.18	10.17
	33	1.71	2.12	2.81	8.91	10.74
	34	1.70	2.13	3.23	9.31	12.20
	35	1.76	2.21	3.17	8.59	12.62
	36	1.65	1.95	3.15	9.88	12.40
	37	1.65	1.90	3.93	10.41	13.12
	38	1.68	2.29	2.96	15.51	13.69
	39	1.76	2.14	2.42	12.60	14.76
	40	1.51	1.70	3.58	11.56	14.08
$+1\sigma$	13	1.35	1.50	1.57	2.31	3.87
	16	1.56	1.72	2.00	3.28	5.17
	20	1.70	2.07	2.24	4.55	6.66
	22	1.67	1.95	2.67	5.30	7.47
	23	1.77	2.21	2.60	5.58	7.88
	24	1.71	2.10	2.39	5.76	7.20
	25	1.88	2.47	2.93	6.07	8.17
	26	1.79	2.12	2.45	6.36	8.34
	28	1.81	2.19	3.16	7.43	10.12
	30	1.90	2.44	2.84	7.98	9.99
	32	1.98	2.45	3.57	8.71	10.92
	35	1.61	1.89	5.07	9.72	12.02
	38	1.53	1.74	4.85	10.86	12.81
	40	2.11	3.33	4.72	11.88	14.76
$+2\sigma$	13	1.34	1.41	1.47	2.39	3.97
	15	1.54	1.74	1.87	2.82	4.57
	18	1.67	1.92	2.39	3.85	4.91
	20	1.57	1.84	2.00	4.48	5.50
	23	1.36	1.48	1.58	5.47	6.55
	25	1.86	2.36	3.75	6.20	7.58
	28	1.58	1.74	2.49	7.25	8.81
	30	2.09	2.66	4.58	8.12	10.07
	32	2.26	3.19	5.00	8.81	10.66
	35	1.46	1.63	1.76	9.48	11.52
	38	1.46	1.76	2.69	11.01	12.89
	40	1.85	2.37	3.37	11.96	14.25
$+3\sigma$	13	1.54	1.67	2.01	2.34	3.69
	15	1.36	1.46	1.53	2.79	3.33
	18	1.60	1.82	2.94	3.90	4.61
	20	1.76	2.07	3.43	4.56	5.54

Table 8 – continued

$\sigma_{C12\alpha}$	$M(\text{ZAMS}) (M_{\odot})$	$M(\text{Fe}) (M_{\odot})$	$M(\text{Si}) (M_{\odot})$	$M(\text{O}) (M_{\odot})$	$M(\text{CO}) (M_{\odot})$	$M(\text{He}) (M_{\odot})$
+3 σ	23	1.37	1.58	2.08	5.54	6.81
	25	1.85	2.25	4.16	6.30	7.88
	28	2.09	2.99	5.26	7.42	9.26
	30	1.66	1.99	5.50	8.03	9.83
	32	1.42	1.57	4.77	8.99	10.47
	35	2.52	3.10	6.54	10.00	12.25
	38	2.39	2.81	6.48	11.01	12.88
	40	1.59	1.86	6.91	11.73	13.76

REFERENCES

- Abbott, R., Abbott, T. D., Abraham, S., et al. 2020, The Astrophysical Journal, 900, L13, doi: [10.3847/2041-8213/aba493](https://doi.org/10.3847/2041-8213/aba493)
- An, Z.-D., Chen, Z.-P., Ma, Y.-G., et al. 2015, Phys. Rev. C, 92, 045802, doi: [10.1103/PhysRevC.92.045802](https://doi.org/10.1103/PhysRevC.92.045802)
- Anders, E., & Grevesse, N. 1989, Geochimica et Cosmochimica Acta, 53, 197, doi: [10.1016/0016-7037\(89\)90286-X](https://doi.org/10.1016/0016-7037(89)90286-X)
- Angulo, C., Arnould, M., Rayet, M., et al. 1999, Nuclear Physics A, 656, 3, doi: [https://doi.org/10.1016/S0375-9474\(99\)00030-5](https://doi.org/10.1016/S0375-9474(99)00030-5)
- Arnett, D. 1996, Supernovae and Nucleosynthesis: An Investigation of the History of Matter from the Big Bang to the Present
- Barkat, Z., Rakavy, G., & Sack, N. 1967, PhRvL, 18, 379, doi: [10.1103/PhysRevLett.18.379](https://doi.org/10.1103/PhysRevLett.18.379)
- Boccioli, L., Gogilashvili, M., Murphy, J., & O'Connor, E. P. 2025, MNRAS, 537, 1182, doi: [10.1093/mnras/staf066](https://doi.org/10.1093/mnras/staf066)
- Boccioli, L., Roberti, L., Limongi, M., Mathews, G. J., & Chieffi, A. 2023, ApJ, 949, 17, doi: [10.3847/1538-4357/acc06a](https://doi.org/10.3847/1538-4357/acc06a)
- Branch, D., & Wheeler, J. C. 2017, Supernova Explosions, doi: [10.1007/978-3-662-55054-0](https://doi.org/10.1007/978-3-662-55054-0)
- Burrows, A., & Vartanyan, D. 2021, Nature, 589, 29, doi: [10.1038/s41586-020-03059-w](https://doi.org/10.1038/s41586-020-03059-w)
- Chatzopoulos, E., Couch, S. M., Arnett, W. D., & Timmes, F. X. 2016, The Astrophysical Journal, 822, 61, doi: [10.3847/0004-637X/822/2/61](https://doi.org/10.3847/0004-637X/822/2/61)
- Chieffi, A., & Limongi, M. 2020, ApJ, 890, 43, doi: [10.3847/1538-4357/ab6739](https://doi.org/10.3847/1538-4357/ab6739)
- Chieffi, A., Roberti, L., Limongi, M., et al. 2021, ApJ, 916, 79, doi: [10.3847/1538-4357/ac06ca](https://doi.org/10.3847/1538-4357/ac06ca)
- Costa, G., Bressan, A., Mapelli, M., et al. 2021, MNRAS, 501, 4514, doi: [10.1093/mnras/staa3916](https://doi.org/10.1093/mnras/staa3916)
- Cristini, A., Hirschi, R., Meakin, C., et al. 2019, MNRAS, 484, 4645, doi: [10.1093/mnras/stz312](https://doi.org/10.1093/mnras/stz312)
- Cyburt, R. H., Amthor, A. M., Ferguson, R., et al. 2010, The Astrophysical Journal Supplement Series, 189, 240, doi: [10.1088/0067-0049/189/1/240](https://doi.org/10.1088/0067-0049/189/1/240)
- de Jager, C., Nieuwenhuijzen, H., & van der Hucht, K. A. 1988, A&AS, 72, 259
- Ertl, T., Janka, H. T., Woosley, S. E., Sukhbold, T., & Ugliano, M. 2016, ApJ, 818, 124, doi: [10.3847/0004-637X/818/2/124](https://doi.org/10.3847/0004-637X/818/2/124)
- Ertl, T., Woosley, S. E., Sukhbold, T., & Janka, H. T. 2020, ApJ, 890, 51, doi: [10.3847/1538-4357/ab6458](https://doi.org/10.3847/1538-4357/ab6458)
- Farmer, R., Fields, C. E., Petermann, I., et al. 2016, ApJS, 227, 22, doi: [10.3847/1538-4365/227/2/22](https://doi.org/10.3847/1538-4365/227/2/22)
- Farmer, R., Renzo, M., de Mink, S. E., Fishbach, M., & Justham, S. 2020, The Astrophysical Journal, 902, L36, doi: [10.3847/2041-8213/abbadd](https://doi.org/10.3847/2041-8213/abbadd)
- Farmer, R., Renzo, M., de Mink, S. E., Marchant, P., & Justham, S. 2019, The Astrophysical Journal, 887, 53, doi: [10.3847/1538-4357/ab518b](https://doi.org/10.3847/1538-4357/ab518b)
- Fields, C. E., Timmes, F. X., Farmer, R., et al. 2018, ApJS, 234, 19, doi: [10.3847/1538-4365/aaa29b](https://doi.org/10.3847/1538-4365/aaa29b)
- Fuller, G. M., Fowler, W. A., & Newman, M. J. 1985, ApJ, 293, 1, doi: [10.1086/163208](https://doi.org/10.1086/163208)
- Hammer, J., Fey, M., Kunz, R., et al. 2005, Nucl. Phys. A, A758, doi: [10.1016/j.nuclphysa.2005.05.066](https://doi.org/10.1016/j.nuclphysa.2005.05.066)
- Hayashi, C., Hōshi, R., & Sugimoto, D. 1962, Progress of Theoretical Physics Supplement, 22, 1, doi: [10.1143/PTPS.22.1](https://doi.org/10.1143/PTPS.22.1)
- Heger, A., Langer, N., & Woosley, S. E. 2008, Astrophysical Journal, 528, 368, doi: [10.1086/308158](https://doi.org/10.1086/308158)
- Jermyn, A. S., Bauer, E. B., Schwab, J., et al. 2023, ApJS, 265, 15, doi: [10.3847/1538-4365/aca8d](https://doi.org/10.3847/1538-4365/aca8d)
- Kaiser, E. A., Hirschi, R., Arnett, W. D., et al. 2020, MNRAS, 496, 1967, doi: [10.1093/mnras/staa1595](https://doi.org/10.1093/mnras/staa1595)

- Keszthelyi, Z., Meynet, G., Shultz, M. E., et al. 2020, *Monthly Notices of the Royal Astronomical Society*, 493, 518, doi: [10.1093/mnras/staa237](https://doi.org/10.1093/mnras/staa237)
- Kippenhahn, R., Weigert, A., & Weiss, A. 2013, *Stellar Structure and Evolution*, doi: [10.1007/978-3-642-30304-3](https://doi.org/10.1007/978-3-642-30304-3)
- Kunz, R., Fey, M., Jaeger, M., et al. 2002, *ApJ*, 567, 643, doi: [10.1086/338384](https://doi.org/10.1086/338384)
- Langanke, K., & Martínez-Pinedo, G. 2000, *NuPhA*, 673, 481, doi: [10.1016/S0375-9474\(00\)00131-7](https://doi.org/10.1016/S0375-9474(00)00131-7)
- Laplace, E., Justham, S., Renzo, M., et al. 2021, *A&A*, 656, A58, doi: [10.1051/0004-6361/202140506](https://doi.org/10.1051/0004-6361/202140506)
- Limongi, M., & Chieffi, A. 2015, in *Chemical and dynamical evolution of the Milky Way and the Local Group*, 15
- Maeder, A., & Stahler, S. 2009, *Physics Today*, 62, 52, doi: [10.1063/1.3226770](https://doi.org/10.1063/1.3226770)
- Mapelli, M., Spera, M., Montanari, E., et al. 2020, *The Astrophysical Journal*, 888, 76, doi: [10.3847/1538-4357/ab584d](https://doi.org/10.3847/1538-4357/ab584d)
- Marchant, P., & Moriya, T. J. 2020, *A&A*, 640, L18, doi: [10.1051/0004-6361/202038902](https://doi.org/10.1051/0004-6361/202038902)
- Müller, B., Heger, A., Liptai, D., & Cameron, J. B. 2016, *MNRAS*, 460, 742, doi: [10.1093/mnras/stw1083](https://doi.org/10.1093/mnras/stw1083)
- Nomoto, K. 1984, *ApJ*, 277, 791, doi: [10.1086/161749](https://doi.org/10.1086/161749)
- Nomoto, K., & Hashimoto, M. 1988, *PhR*, 163, 13, doi: [10.1016/0370-1573\(88\)90032-4](https://doi.org/10.1016/0370-1573(88)90032-4)
- Nomoto, K., Kobayashi, C., & Tominaga, N. 2013, *ARA&A*, 51, 457, doi: [10.1146/annurev-astro-082812-140956](https://doi.org/10.1146/annurev-astro-082812-140956)
- Nugis, T., & Lamers, H. J. G. L. M. 2000, *A&A*, 360, 227
- O'Connor, E., & Ott, C. D. 2011, in *APS Division of Nuclear Physics Meeting Abstracts*, APS Meeting Abstracts, CG.005
- Oda, T., Hino, M., Muto, K., Takahara, M., & Sato, K. 1994, *Atomic Data and Nuclear Data Tables*, 56, 231, doi: <https://doi.org/10.1006/adnd.1994.1007>
- Ohkubo, T., Nomoto, K., Umeda, H., Yoshida, N., & Tsuruta, S. 2009, *ApJ*, 706, 1184, doi: [10.1088/0004-637X/706/2/1184](https://doi.org/10.1088/0004-637X/706/2/1184)
- Osaki, Y. 1966, *PASJ*, 18, 384
- Paxton, B., Bildsten, L., Dotter, A., et al. 2011, *ApJS*, 192, 3, doi: [10.1088/0067-0049/192/1/3](https://doi.org/10.1088/0067-0049/192/1/3)
- Paxton, B., Cantiello, M., Arras, P., et al. 2013, *ApJS*, 208, 4, doi: [10.1088/0067-0049/208/1/4](https://doi.org/10.1088/0067-0049/208/1/4)
- Paxton, B., Marchant, P., Schwab, J., et al. 2015, *ApJS*, 220, 15, doi: [10.1088/0067-0049/220/1/15](https://doi.org/10.1088/0067-0049/220/1/15)
- Paxton, B., Schwab, J., Bauer, E. B., et al. 2018, *ApJS*, 234, 34, doi: [10.3847/1538-4365/aaa5a8](https://doi.org/10.3847/1538-4365/aaa5a8)
- Paxton, B., Smolec, R., Schwab, J., et al. 2019, *ApJS*, 243, 10, doi: [10.3847/1538-4365/ab2241](https://doi.org/10.3847/1538-4365/ab2241)
- Renzo, M., Cantiello, M., Metzger, B. D., & Jiang, Y. F. 2020, *ApJL*, 904, L13, doi: [10.3847/2041-8213/abc6a6](https://doi.org/10.3847/2041-8213/abc6a6)
- Renzo, M., Ott, C. D., & Shore, S. N. 2017, *A&A*, 603, A118, doi: [10.1051/0004-6361/201730698](https://doi.org/10.1051/0004-6361/201730698)
- Rizzuti, F., Hirschi, R., Georgy, C., et al. 2022, *MNRAS*, 515, 4013, doi: [10.1093/mnras/stac1981](https://doi.org/10.1093/mnras/stac1981)
- Sallaska, A. L., Iliadis, C., Champagne, A. E., et al. 2013, *ApJS*, 207, 18, doi: [10.1088/0067-0049/207/1/18](https://doi.org/10.1088/0067-0049/207/1/18)
- Schneider, F. R. N., Podsiadlowski, Ph., & Müller, B. 2021, *A&A*, 645, A5, doi: [10.1051/0004-6361/202039219](https://doi.org/10.1051/0004-6361/202039219)
- Schwarzschild, M. 1958, *Structure and evolution of the stars*.
- Sugimoto, D., & Fujimoto, M. Y. 2000, *ApJ*, 538, 837, doi: [10.1086/309150](https://doi.org/10.1086/309150)
- Sugimoto, D., & Nomoto, K. 1980, *SSRv*, 25, 155, doi: [10.1007/BF00212318](https://doi.org/10.1007/BF00212318)
- Sukhbold, T., & Adams, S. 2020, *MNRAS*, 492, 2578, doi: [10.1093/mnras/staa059](https://doi.org/10.1093/mnras/staa059)
- Sukhbold, T., Ertl, T., Woosley, S. E., Brown, J. M., & Janka, H. T. 2016, *ApJ*, 821, 38, doi: [10.3847/0004-637X/821/1/38](https://doi.org/10.3847/0004-637X/821/1/38)
- Sukhbold, T., & Woosley, S. E. 2014, *ApJ*, 783, 834, doi: [10.1088/0004-637X/783/1/10](https://doi.org/10.1088/0004-637X/783/1/10)
- Sukhbold, T., Woosley, S. E., & Heger, A. 2018, *ApJ*, 860, 93, doi: [10.3847/1538-4357/aac2da](https://doi.org/10.3847/1538-4357/aac2da)
- Timmes, F. X. 1999, *ApJS*, 124, 241, doi: [10.1086/313257](https://doi.org/10.1086/313257)
- Timmes, F. X., Hoffman, R. D., & Woosley, S. E. 2000, *ApJS*, 129, 377, doi: [10.1086/313407](https://doi.org/10.1086/313407)
- Timmes, F. X., Woosley, S. E., & Weaver, T. A. 1996, *ApJ*, 457, 834, doi: [10.1086/176778](https://doi.org/10.1086/176778)
- Tumino, A., Spitaleri, C., La Cognata, M., et al. 2018, *Nature*, 557, 687, doi: [10.1038/s41586-018-0149-4](https://doi.org/10.1038/s41586-018-0149-4)
- Tur, C., Heger, A., & Austin, S. M. 2007, *ApJ*, 671, 821, doi: [10.1086/523095](https://doi.org/10.1086/523095)
- Ugliano, M., Janka, H.-T., Marek, A., & Arcones, A. 2012, *ApJ*, 757, 69, doi: [10.1088/0004-637X/757/1/69](https://doi.org/10.1088/0004-637X/757/1/69)
- van Son, L. A. C., De Mink, S. E., Broekgaarden, F. S., et al. 2020, *ApJ*, 897, 100, doi: [10.3847/1538-4357/ab9809](https://doi.org/10.3847/1538-4357/ab9809)
- Vink, J. S., de Koter, A., & Lamers, H. J. G. L. M. 2001, *A&A*, 369, 574, doi: [10.1051/0004-6361:20010127](https://doi.org/10.1051/0004-6361:20010127)
- Wang, T., Vartanyan, D., Burrows, A., & Coleman, M. S. B. 2022, *MNRAS*, 517, 543, doi: [10.1093/mnras/stac2691](https://doi.org/10.1093/mnras/stac2691)
- Weaver, T. A., & Woosley, S. E. 1993, *PhR*, 227, 65, doi: [10.1016/0370-1573\(93\)90058-L](https://doi.org/10.1016/0370-1573(93)90058-L)
- West, C., Heger, A., & Austin, S. M. 2013, *ApJ*, 769, 2, doi: [10.1088/0004-637X/769/1/2](https://doi.org/10.1088/0004-637X/769/1/2)
- Woosley, S. E. 2017, *The Astrophysical Journal*, 836, 244, doi: [10.3847/1538-4357/836/2/244](https://doi.org/10.3847/1538-4357/836/2/244)

Woosley, S. E., & Heger, A. 2021, ApJL, 912, L31,
doi: [10.3847/2041-8213/abf2c4](https://doi.org/10.3847/2041-8213/abf2c4)

Woosley, S. E., Heger, A., & Weaver, T. A. 2002, Reviews
of Modern Physics, 74, 1015,
doi: [10.1103/RevModPhys.74.1015](https://doi.org/10.1103/RevModPhys.74.1015)